A Rhodium Centered Supramolecular Complex as a Photoinitiated Electron Collector

by

Mark Christopher Elvington

Dissertation submitted to the faculty of the

Virgnia Polytechnic Institute and State University

in partial fulfillment of the requirements for the degree of

Doctor of Philosophy

in

Chemistry

Karen J. Brewer, Chair

Mark R. Anderson

Paul A. Deck

Brian E. Hanson

Gordon T. Yee

July 24, 2007
Blacksburg, Virginia

Keywords: Supramolecular, photochemistry, photocatalysis, electron transfer

A Rhodium Centered Supramolecular Complex as a Photoinitiated Electron Collector

Mark Christopher Elvington

Abstract

The research presented here is focused on photochemical studies of a supramolecular structural motif for photoinitiated electron collection. The complex studied, $[\{(bpy)_2Ru(dpp)\}_2RhCl_2](PF_6)_5$, is of the form LA-BL-EC-BL-LA comprising a Ru(II) polyazine light absorber (LA) bearing two bpy (bpy = 2,2'-bipyridine) ligands, two dpp (dpp = 2,3'-bis(2-pyridyl)pyrazine) bridging ligands (BL), and a central rhodium(III) electron collector (EC). Ruthenium-polyazine light absorbers are commonly used in light to energy conversion systems due to the intense metal to ligand charge transfer (MLCT) absorptions observed in the visible spectrum. Electrochemical methods establish rhodium as the site of localization of the lowest lying unoccupied molecular orbital, while phosphorescence measurements are used to study electron transfer within the supramolecular assembly. Electrochemical and photochemical experiments show that the absorption of light in the rhodium centered supramolecular complex, $[\{(bpy)_2Ru(dpp)\}_2RhCl_2](PF_6)_5$, can initiate the sequential transfer of multiple electrons to the rhodium metal center, i.e. photoinitiated electron collection. A mechanistic study of photoinitiated electron collection, involving a Stern-Volmer analysis of emission quenching and product formation, is also presented, to determine the rate constants of the possible excited state and ground state reactions. One application of a molecular device for photoinitiated electron collection is fuel production. It has been

shown that the complex studied, $[\{(bpy)_2Ru(dpp)\}_2RhCl_2](PF_6)_5$, can collect reducing equivalents and use them to catalyze the reduction of water to hydrogen. Photocatalytic hydrogen generation experiments will also be presented including initial quantum yield optimization experiments.

Thesis Statement

The goal of this research is to develop an understanding of the functioning of a photochemical molecular device using supramolecular architecture designed to undergo photoinitiated electron collection.

Acknowledgments

First and foremost I would like to thank two of the most important people in my life, my parents, Tony and Ulrike Elvington for their support throughout my life and my sister Maria Elvington for her support in my endeavors. I also acknowledge members of the Brewer group past and present for their support and for our discussions that has furthered my knowledge of chemistry. I would like to specifically thank Shamindri Arachchige for her collaborative work in photocatalytic hydrogen generation experiments. I thank the members of my committee, Mark Anderson, Paul Deck, Brian Hanson, and Gordon Yee for their help in developing my knowledge of chemistry. Lastly, I want to thank Karen Brewer for her guidance and support. Her contribution toward my development as a chemist is immeasurable.

Funding of this work has been provided by VTabc, The National Science Foundation (CHE–0408445), and The American Chemical Society Petroleum Research Fund. Acknowledgment is also made to the Chemical Sciences, Geosciences and Biosciences Division, Office or Basic Energy Sciences, Office of Sciences, U. S. Department of Energy for their generous support of this research. I also would like to acknowledge Phoenix Canada Oil Company for their financial collaboration in this research project, which holds long term license rights to commercialize the technology.

Table of Contents

List of Figures

List of Tables

Table of Abbreviations

Abbreviations	
BL	bridging ligand
bpbimH2	2,2'-bis(2-pyridyl)bibenzimidazole
bpm	2,2'-bipyrimidine
bpy	2,2'-bipyridine
CV	cyclic voltammetry
dmbpbim	1,1'-dimethyl-2,2'-bis(2-pyridyl)-6,6'-bibenzimidazole
dpb	2,3-bis(2-pyridyl)benzoquinoxaline
dpbime	bis[2-(2-pyridyl)benzimidazoyl]ethane
dpimbH2	2,6-bis(2-pyridyl)benzdiimidazole
dpp	2,3-bis(2-pyridyl)pyrazine
dpq	2,3-bis(2-pyridyl)quinoxaline
EC	electron collector
EA	electron acceptor
ED	electron donor
HOMO	highest occupied molecular orbital
IL	intraligand
LA	light absorber
LF	ligand field
LUMO	lowest unoccupied molecular orbital
MLCT	metal to ligand charge transfer
MMCT	metal to metal charge transfer
PEC	photoinitiated eletron collection
phen	1,10-phenanthroline
SWV	squarewave voltammetry
tatpp	phenanthroline-pyrazine-benzene-pyrazine-phenanthroline
tatpq	phenanthroline-pyrazine-quinone-pyrazine-phenanthroline
TL	terminal ligand
tpp	2,3,5,6-tetrakis(2-pyridyl)pyrazine
tpy	2,2',2"-terpyridine
ttpy	4'-p-toyl-2,2':6,2"-terpyridine

I. Introduction

A. Supramolecular Chemistry

1. Supramolecular Chemistry Defined

Within the context of coordination chemistry a supramolecular assembly can be defined as a complex that is made up of individual components connected together with bridging ligands to form a supramolecular architecture. Supramolecular assemblies are composed of metals and ligands that form subunits with well defined individual properties. Each component essentially retains its own properties and provides a specific function, which can be combined in certain architectures to exploit the component's function. The design of these multicomponent systems can consist of a large variety of ligands, of which bidentate polypyridyl/polyazine ligands are the most common. Tridentate polyazine ligands have also found use in this arena but their chemistry has not been as thoroughly developed. Research in supramolecular chemistry has recently made sufficient progress to enable rapid growth in the design and realization of photochemical molecular devices, which consist of systems capable of performing complex light induced functions, i.e. photoinitiated electron collection.

Supramolecular complexes are composed of multiple components, the selection of which dictates the functioning of the molecular device. Supramolecular complexes that undergo light induced processes contain chromophores and are often referred to as photochemical molecular devices. Chromophores, molecules or parts of molecules that are capable of absorbing light, often comprise polyazine ligands bound to transition metals such as ruthenium or osmium. The absorption of light initiates the functioning of a photochemical molecular device and thus chromophores are integral in the design of

such complexes. There are several reviews relevant to this topic, including reviews on emissive polynuclear transition metal complexes,[1] transition metal complexes bridged by tridentate polyazine ligands,[2] electron transfer in Ru/Os complexes,[3] and a review on photoinduced processes in multicomponent arrays of transition metal complexes.[4]

2. Supramolecular Complex Components

Ruthenium-polyazine complexes are generally good light absorbers (LAs). These chromophores have $\pi \rightarrow \pi^*$ ligand based transitions with absorption maxima typically in the UV region of the electromagnetic spectrum. Ru-polyazine chromophores also possess a lower energy transition involving a charge transfer from a ruthenium based highest occupied molecular orbital (HOMO) to the ligand based lowest unoccupied molecular orbital (LUMO), Figure 1. This transition corresponds to the strong absorption maximum located in the visible region of the spectrum. Following metal to ligand charge

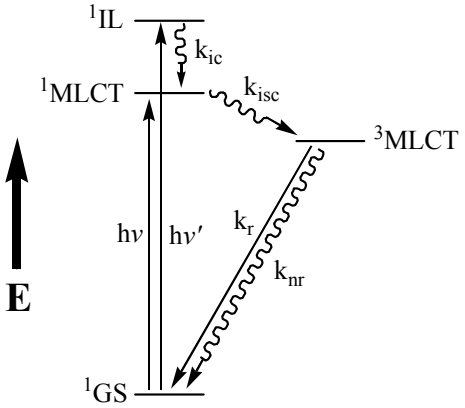

Figure 1. Energy state diagram for the general complex $[Ru(ligand)_3]^{2+}$ where the ligand is a polypyridyl bridging or terminal ligand. MLCT is Ru $\rightarrow$ ligand charge transfer, IL is intraligand centered $\pi \rightarrow \pi^*$ transition, k_{ic} is the rate of internal conversion, k_{isc} is the rate of intersystem crossing, k_r is the rate of radiative decay (phosphorescence), and k_{nr} is the rate of nonradiative decay.

transfer (MLCT) excitation, the excited electron rapidly undergoes a spin flip, known as intersystem crossing (isc) resulting in population of the ^{3}MLCT state. The ^{3}MLCT state is a relatively long lived state in most polyazine systems, typically on the order of several hundred nanoseconds or longer, which undergoes nonradiative and radiative deactivation to regenerate the ground state molecule. Nonradiative decay is an excited state deactivation pathway (primarily vibrational relaxation) represented by a wavy line in an energy state diagram. Radiative decay from a triplet excited state to a singlet ground state, also known as phosphorescence, is a deactivation pathway where a photon of light is emitted, and is represented by a straight line in an energy state diagram.

Multicomponent photochemical molecular devices can be designed to take advantage of the long lived ^{3}MLCT state by incorporating an electron acceptor (EA) into the supramolecular framework. Electron transfer can occur from the ^{3}MLCT state to a lower lying acceptor orbital resulting in quenching of the ^{3}MLCT state emission and the formation of a charge separated state. If the electron acceptor is a metal like rhodium, this charge separated state is designated a metal to metal charge transfer (MMCT) state. If multiple electron transfers are possible, the site of electron transfer can be considered an electron collector (EC). Electron transfer, and ^{3}MMCT states will be discussed below in detail.

3. Polyazine Ligands of Interest

Several useful polyazine terminal and bridging ligands are shown below are utilized in the supramolecular coordination complexes that will be discussed. These terminal and bridging ligands are shown below in Figures 2 and 3 respectively.

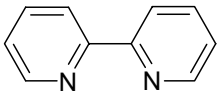

2,2'-bipyridine (bpy)

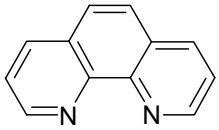

1,10-phenanthroline (phen)

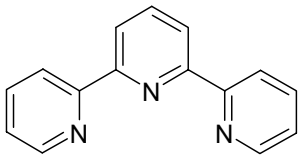

2,2',2"-terpyridine (tpy)

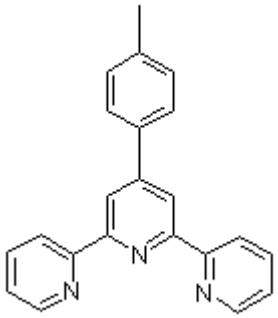

4'-p-tolyl-2,2':6,2"-terpyridine (ttpy)

Figure 2. Polyazine bidentate and tridentate terminal ligands.

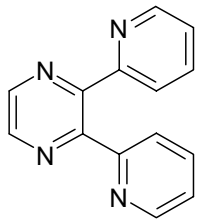

2,3-bis(2-pyridyl)pyrazine (dpp)

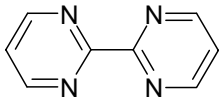

2,2'-bipyrimidine (bpm)

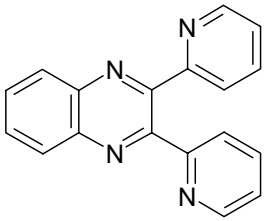

2,3-bis(2-pyridyl)quinoxaline (dpq)

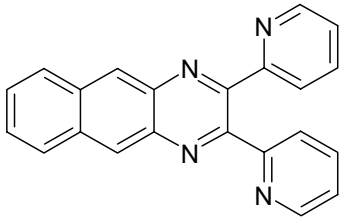

2,3-bis(2-pyridyl)benzoquinoxaline (dpb)

Figure 3. Polyazine bidentate and tridentate bridging ligands.

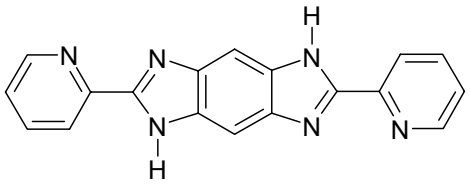

2,6-bis(2'-pyridyl)benzdiimidazole
($dpimbH_2$)

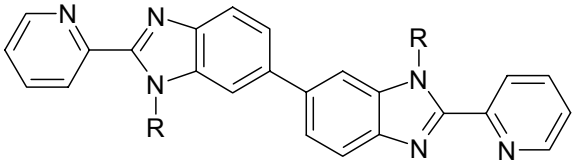

R=H 2,2'-bis(2-pyridyl)bibenzimidazole
($bpbimH_2$)
$R=CH_3$ 1,1'-dimethyl-2,2'-bis
(2-pyridyl)-6,6'-bibenzimidazole
(dmbpbim)

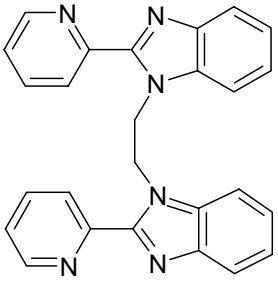

bis[2-(2'-pyridyl)benzimidazoyl]ethane
(dpbime)

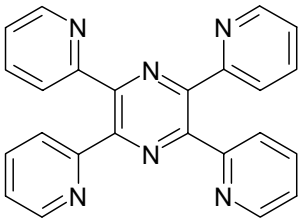

2,3,5,6-tetrakis(2-pyridyl)pyrazine
(tpp)

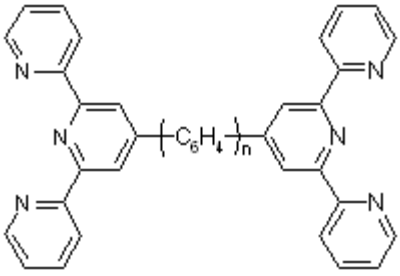

two 2,2':6,2"-terpyridines
tpy-$(C_6H_4)_n$-tpy

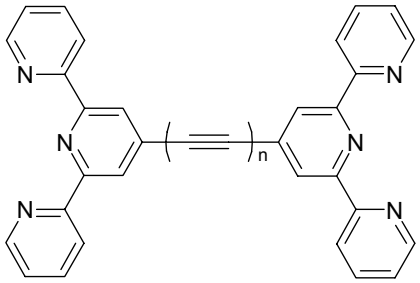

two 2,2':6,2"-terpyridines
tpy-$(C_2)_n$-tpy

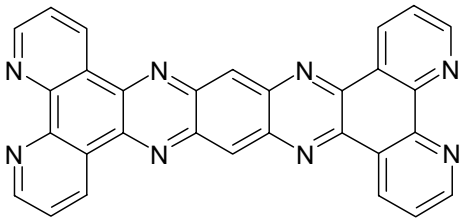

tatpp

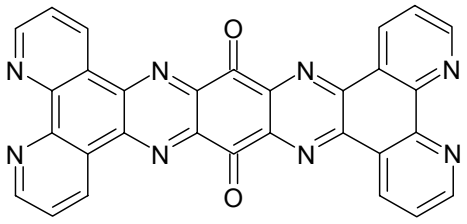

tatpq

Figure 3 (cont.). Polyazine bidentate and tridentate bridging ligands of interest.

4. $[Ru(bpy)_3](PF_6)_2$, a Prototypical Light Absorber

The coordination complex $[Ru(bpy)_3]^{2+}$ is a well known chromophore that was first synthesized in 1936 by Burstall.[5] $[Ru(bpy)_3]^{2+}$ is a d^6 pseudooctahedral ruthenium complex. It is bright orange in color due to its intense $Ru(d\pi) \rightarrow bpy(\pi^*)$ MLCT transition and has an absorption wavelength maximum, λ_{max}^{abs}, at 450 nm.[6] This chromophore also has a long-lived ^{3}MLCT excited state, approximately 860 ns, from which phosphorescence can be observed in the visible region of the electromagnetic spectrum at 605 nm.[6] $[Ru(bpy)_3]^{2+}$ is the most well known transition metal-polyazine light absorber and is considered the prototypical chromophore. This light absorber and its derivatives have been the subject of much study.

Studies in the late 1970s and early 1980s initially by Sauvage[7,8] and subsequently by Creutz[9-13] showed the potential for ruthenium-rhodium electron transfer systems in photochemical energy conversion schemes. The system studied involves the MLCT excitation of the chromophore, $[Ru(bpy)_3]^{2+}$, followed by excited state electron transfer to $[Rh(bpy)_3]^{3+}$. The resulting $[Rh(bpy)_3]^{2+}$ can then disproportionate to form $[Rh(bpy)_2]^{+}$ and $[Rh(bpy)_3]^{3+}$ or in the presence of a heterogeneous platinum catalyst can generate hydrogen.[9-13] Hydrogen catalysis for this system is discussed in more detail in section IV. D. There are, however, kinetic limitations associated with bimolecular systems. In contrast, a unimolecular system is not limited by diffusion and thus it is possible to enhance the efficiency of electron transfer. A supramolecular framework can be utilized to connect the electron donor and acceptor. Bipyridine is a bidentate ligand that readily binds to transition metals forming complexes like the above mentioned $[Ru(bpy)_3]^{2+}$ chromophore. Other polyazine ligands can be substituted for bipyridine resulting in a

great variety of possible complexes. Usually, only minor modifications of the synthetic procedure are necessary to achieve the desired product in high yield. Substitution of a bipyridine for a bridging polyazine ligand allows for the design of multimetallic supramolecular complexes.

5. *$[Ru(bpy)_2(dpp)](PF_6)_2$, a Light Absorber with a Bridge*

The coordination complex $[Ru(bpy)_2(dpp)]^{2+}$ (dpp = 2,3-bis(2-pyridyl)pyrazine), is probably the most well known chromophore containing a bridging ligand. This complex was first synthesized by Gafney in 1987,[14] and has also been studied in detail along with many similar monometallic complexes by Balzani. $[Ru(bpy)_2(dpp)]^{2+}$ is also a d^6 octahedral ruthenium complex and is bright orange in color, due to its intense $Ru(d\pi) \rightarrow bpy(\pi^*)$ and $Ru(d\pi) \rightarrow dpp(\pi^*)$ CT transitions in the visible region. These MLCT transitions have absorption wavelength maxima at 450 and 480 nm, respectively. This chromophore also has a single long-lived ^{3}MLCT excited state that emits in the visible region of the solar spectrum at 640 nm with a lifetime of approximately 500 ns.[14] The presence of the bis bidentate bridging ligand dpp, Figure 3, within the chromophore enables its use in the construction of complex supramolecular systems, the first step in designing a photochemical molecular device.[14]

6. *Metal and Ligand Impact on Orbital Energetics*

The successful functioning of a photochemical molecular device is dependent on the relative orbital energetics for each component. Varying the ligands on transition metal complexes can modulate the energetics of component within a supramolecular

assembly. A study of a series of rhodium-polyazine complexes demonstrates the potential to tune the energetics of supramolecular components through ligand substitution as shown in Table 1.

The electronic absorption spectra for a series of polyazine-rhodium complexes of the form $[Rh(BL)_2Br_2]^+$ (BL = bpy, bpm, dpp, dpq, dpb) are dominated by intense ligand-based transitions in the ultraviolet region, typical of rhodium centered transition metal complexes.[15] The electronic absorption spectra for the series of complexes shows that substituting bpy with dpp and other highly conjugated bridging ligands results in a red-shift, a shift to lower energy, of the IL absorbance maxima, Table 1. If the ligand π orbital energy remains unchanged, lowering the ligand π^* orbital energy relative to bpy would result in lower energy $\pi \rightarrow \pi^*$ transitions, which is observed in this series of complexes.

$[Rh(BL)_2Cl_2](PF_6)$ complexes emit from their lowest lying excited state, a LF state. Emission was observed only at low temperature, typical of LF emitters. The emission spectra showed a pronounced red shift as bpy was substituted by bpm, dpp, dpq, and dpb, which is indicative of a decreased σ donating ability for the pyrazine based ligands which results in smaller ligand field splitting and thus lower energy LF emissions, Table 1.

An analysis of the electrochemical data also shows an electronic trend as a function of BL in the series of $[Rh(BL)_2Cl_2](PF_6)$ complexes. Cyclic voltammetry shows an irreversible rhodium reduction followed by successive ligand-based reductions. The cyclic voltammetry data shows that the substitution of bpy for BL results in complexes that are easier to reduce. Both rhodium based reductions and BL reductions have

decreasing $E_{1/2}$s in the order of bpy > bpm > dpp > dpq > dpb, Table 1. These ligand substitutions demonstrate the ability to tune the energetics of both the BLs and the metals. This study suggests that multicomponent systems based on transition metal complexes can be designed to impact orbital energetics in a specific manner. The energetics of the HOMO and LUMO has a direct impact on energy/electron transfer within the supramolecular assembly.[15]

Table 1. Electrochemical, electronic spectroscopy, and 298 K emission data for monometallic and multimetallic complexes of ruthenium and rhodium.

Complex	$E_{1/2}^{ox}$ [a] (V)	$E_{1/2}^{red}$ [a] (V)	λ_{max}^{abs} (nm)	λ_{max}^{em} 298 K	λ_{max}^{em} 77 K [b]	τ (ns) 298 K	τ (μs) 77 K	*ref*
Mononuclear Rh and Ru complexes								
$[Rh(bpy)_2Br_2](PF_6)$	-	-0.50	302	-	660	-	-	*15*
		-1.01	311					
		-1.21						
$[Rh(bpm)_2Br_2](PF_6)$	-	-0.33	224	-	691	-	-	*15*
		-1.05	328					
		-1.41						
$[Rh(dpp)_2Br_2](PF_6)$	-	-0.31	280	-	707	-	-	*15*
		-0.76	328					
		-0.90						
$[Rh(dpq)_2Br_2](PF_6)$	-	-0.15	256	-	737	-	-	*15*
		-0.56	282					
		-1.20	376					
$[Rh(dpb)_2Br_2](PF_6)$	-	-0.10	334	-	-	-	-	*15*
		-0.43	408					
		-0.95						
$[Rh(bpy)_2(dpp)](PF_6)_3$	-	-	308	450	-	390	-	*23*
			321					
$[Rh(bpy)_2Cl_2](PF_6)$	-	-	300	308	704	-	19.6	*23*
			311					
$[Rh(dpp)_2Cl_2](PF_6)$	-	-	286	-	-	90	-	*23*
			326					
$[Ru(bpy)_2(CN)_2]$	0.96	-1.43	428[c]	634[d]	573[d]	430[d]	4.3[d]	*25*
		-1.66						
$[Ru(ttpy)_2](PF_6)_2$	1.49	-1.00	-	-	-	3200[e]	13.5	*28*
		-1.22						
Homonuclear Ru-Ru complexes								
$[(bpy)_2Ru(dpp)Ru(bpy)_2](PF_6)_4$	-	-	284	790	702	140	2.38	*23*
$[(ttpy)Ru(tpy\text{-}tpy)Ru(ttpy)](PF_6)_4$	1.55	-0.69	-	-	770	3500[e]	12.9	*28*
		-1.00						
$[(phen)_2Ru(tatpp)Ru(phen)_2](PF_6)_4$	1.56	-0.02	-	-	-	-	-	*42*
		-0.51						
		-1.08						

[a] Cyclic voltammetry potentials referenced vs. NHE. [b] 77 K emission data recorded in EtOH/MeOH unless otherwise noted. [c] in H_2O. [d] in DMSO-H_2O (1:1). [e] lifetime measured at 150 K.

Table 1 (cont.). Electrochemical, electronic spectroscopy, and 298 K emission data for monometallic and multimetallic complexes of ruthenium and rhodium.

Complex	$E_{1/2}^{ox}$ [a] (V)	$E_{1/2}^{red}$ [a] (V)	λ_{max}^{abs} (nm)	λ_{max}^{em} 298 K	λ_{max}^{em} 77 K[b]	τ (ns) 298 K	τ (μs) 77 K	*ref*
Heteronuclear Ru-Rh complexes								
$[(bpy)_2Ru(dpp)Rh(bpy)_2](PF_6)_5$	-	-	284 425 519	778	632 687	37	1.71	*23*
$[(bpy)_2Ru(CN)(\mu\text{-}CN)Rh(NH_3)_5](PF_6)_3$	1.24	-1.46 -1.69	415[c]	604[d]	556[d]	310[d]	5.7[d]	*25*
$[(bpy)_2Ru\{(\mu\text{-}CN)Rh(NH_3)_5\}_2](PF_6)_6$	1.19	-1.45 -1.69	408[c]	576[d]	543[d]	40[d]	8.4[d]	*25*
$[(bpy)_2Ru(dpimbH_2)Rh(bpy)_2](ClO_4)_5$	1.47	-0.52	-	-	632	-	-	*27*
$[(bpy)_2Ru(bpbimH_2)Rh(bpy)_2](ClO_4)_5$	1.44	-0.48	-	-	603	-	-	*27*
$[(bpy)_2Ru(dmbpbim)Rh(bpy)_2](ClO_4)_5$	1.43	-0.53	-	-	609	-	-	*27*
$[(bpy)_2Ru(dpbime)Rh(bpy)_2](ClO_4)_5$	1.50	-0.51	-	-	609	-	-	*27*
$[(ttpy)Ru(tpy\text{-}tpy)Rh(ttpy)](PF_6)_5$	1.55	-0.30 -0.98 -1.20	-	-	-	<100[e]	12.5	*28*
$[(ttpy)Ru(tpy\text{-}ph\text{-}tpy)Rh(ttpy)](PF_6)_5$	1.53	-0.32 -0.94 -1.12	-	-	-	3000[e]	13.0	*28*
$[(ttpy)Ru(tpy\text{-}ph_2\text{-}tpy)Rh(ttpy)](PF_6)_5$	1.51	-0.32 -0.96 -1.13	-	-	-	3500[e]	13.2	*28*
$[(tpy)Ru(tpp)RhCl_3](PF_6)_2$	1.89	+0.06 -0.31	516	830	-	22	-	*30*
Trimetallic complexes								
$[\{(bpy)_2Ru(dpb)\}_2IrCl_2](PF_6)_5$	-	+0.31 +0.16	-	-	-	-	-	*39*

[a] Cyclic voltammetry potentials referenced vs. NHE. [b] 77 K emission data recorded in EtOH/MeOH unless otherwise noted. [c] in H_20. [d] in DMSO-H_2O (1:1). [e] lifetime measured at 150K.

B. Electron Transfer in Supramolecular Complexes

1. Charge Transfer Excitations in Transition Metal Coordination Complexes

Charge transfer transitions are fundamental to coordination complexes and require consideration due to their importance in supramolecular chemistry. Photoinduced electron transfer has been the subject of many detailed theoretical studies.[16-19] This section will review charge transfer transitions in a fundamental way.

Consider the following system, consisting of two components, a light absorber (LA) and an electron acceptor (EA) or electron donor (ED). The first step is the absorption of light resulting in population of a MLCT excited state (eq1). The excited molecule *LA, can then undergo oxidation or reduction with EA or ED respectively, resulting in photoinduced electron transfer (eq2, eq3).

$$LA + h\nu \rightarrow {}^*LA \qquad \text{(eq1)}$$

$${}^*LA + EA \rightarrow LA^+ + EA^- \qquad \text{(eq2)}$$

$${}^*LA + ED \rightarrow LA^- + ED^+ \qquad \text{(eq3)}$$

Examination of the system from an electrochemical standpoint allows for an analysis of the thermodynamic driving force for excited state electron transfer. Upon absorption of visible light resulting in *LA (eq1), the excited state oxidation and reduction potentials are less positive and less negative respectively, relative to the ground state redox potentials. *LA becomes both a stronger reducing agent and a stronger oxidizing agent generating the thermodynamic driving force required for electron transfer. The excited state redox potentials, $E°\ (LA^+ / LA^*)$ (eq4) and $E°\ (LA^* / LA^-)$ (eq5), can be calculated from the ground state redox potential, $E°\ (LA^+ / LA)$, by the following equations

$$E^\circ (LA^+ / LA^*) = E^\circ (LA^+ / LA) - E_{0\text{-}0} \quad \text{(eq4)}$$

$$E^\circ (LA^* / LA^-) = E^\circ (LA / LA^-) + E_{0\text{-}0} \quad \text{(eq5)}$$

where $E_{0\text{-}0}$ is the energy difference between the ground vibrational state of the first electronic excited state and the ground vibrational, ground electronic state. In a system with an ED and EA separated by a bridge, the bridging ligand can affect the strength of the electronic interaction. The strength of the electronic interaction is related to the length and geometry of the ligand and its electronic nature as discussed in detail later. The free energy change for an electronic interaction, ΔG°, can be calculated by the Weller equation[20]

$$\Delta G^\circ = E^\circ (LA^+ / LA) - E^\circ (LA / LA^-) - E_{00} \quad \text{(eq6)}$$

with the assumption that the Coulombic stabilization energy of the products is negligible. When the electronic interaction is small and the electron transfer process approaches the nonadiabatic limit, the rate of electron transfer, k_{et}, can be calculated by the Marcus model.[21]

$$k_{et} = \nu \exp[(\lambda / 4)(1 + \Delta G^\circ / \lambda)^2 / (RT)] \quad \text{(eq7)}$$

where ν is the frequency factor related to the nuclear motion, λ is the reorganizational energy factor which will be discussed in more detail below, R is the gas constant (8.314 $J \cdot K^{-1} \cdot mol^{-1}$),[22] and T is temperature in K. In the nonadiabatic case the rate limiting step is the electron transfer at the transition state geometry. If, however, the electronic interaction is large, the rate of electron transfer is given by equation 7 under the adiabatic limit where the rate determining step is the slow nuclear motion from the initial geometry to the transition state geometry.[1,3] Investigating the photophysical and redox properties

of polypyridyl transition metal complexes can lead to a better understanding of electron transfer processes. A specific example is provided to illustrate electron transfer.

Kalyanasundaram studied the heterobimetallic complex $[(bpy)_2Ru^{II}(dpp)Rh^{III}(bpy)_2]^{5+}$ (**1**), Figure 4A, and their corresponding mononuclear parent compounds.[23] Upon photo-excitation into the ^{1}MLCT excited state of the complex $[(bpy)_2Ru^{II}(dpp)Rh^{III}(bpy)_2]^{5+}$, intersystem crossing results in quantitative formation of the ^{3}MLCT state followed by quenching of the ^{3}MLCT emission resulting in a very short excited state lifetime. This rapid deactivation of the ^{3}MLCT state can theoretically be a result of enhanced nonradiative decay (k_{nr}), intramolecular electron transfer (k_{et}), or intramolecular energy transfer, Figure 4B. The degree of quenching can be determined by comparing the quantum yield of emission in complex (**1**) with the parent complex $[Rh^{III}(bpy)_2(dpp)]^{3+}$ (**2**). Quantum yields are typically defined as a ratio between two processes, for example, the formation of a species versus the number of photons to generate the species. In this system, the quantum yield of emission, Φ^{em}, is determined

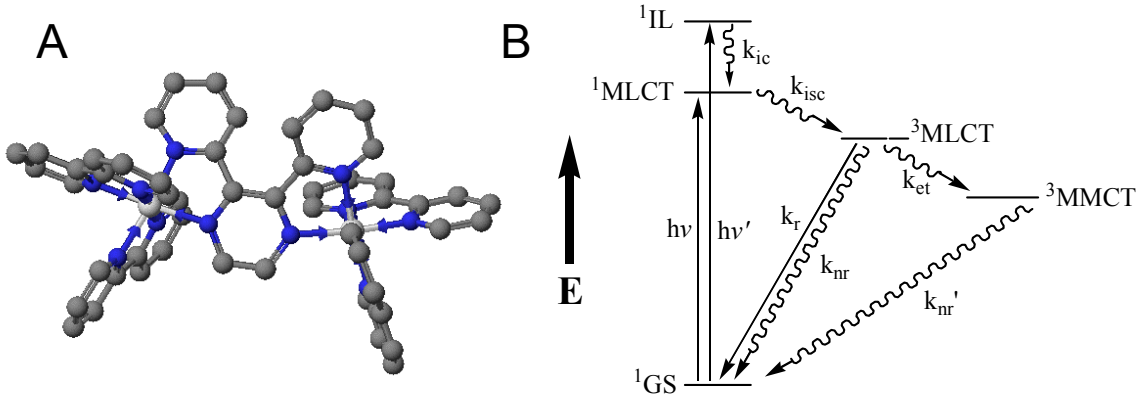

Figure 4. A) CAChe generated structure for the heterobimetallic complex $[(bpy)_2Ru(dpp)Rh(bpy)_2]^{5+}$ (bpy = 2,2'-bipyridine; dpp = 2,3-bis(2-pyridyl)pyrazine) B) Energy state diagram for the complex $[(bpy)_2Ru(dpp)Rh(bpy)_2]^{5+}$ where MLCT is Ru → dpp charge transfer, IL is intraligand π → π* transition, MMCT is Ru → Rh charge transfer, k_{ic} is the rate of internal conversion k_{isc} is intersystem crossing, k_r is the rate of radiative decay (phosphorescence), k_{nr} is the rate of nonradiative decay, k_{et} is the rate of electron transfer.

by the ratio of the rate of radiative decay versus the sum of all the decay pathways (eq8).

$$\Phi^{em} = \frac{k_r}{\sum k_{decay\ pathways}} \qquad \text{(eq8)}$$

In order to determine the prevalent quenching pathway**,** complex **2** and the complexes $[Rh^{III}(bpy)_2Cl_2]^+$ (**3**) and $[Rh^{III}(dpp)_2Cl_2]^+$ (**4**) were also examined. Upon irradiation of the bimetallic complex (**1**) a charge transfer excited state appears to form that is Ru → dpp MLCT in character. Other than the broad absorption band that appears around 510 nm (MLCT) the absorption spectra of the bimetallic (**1**) and the monometallic parent (**2**) are nearly identical. Comparing the absorption spectra one can see that the $\pi \rightarrow \pi^*$ transition at 284 nm of the Rh(III)-polypyridyl unit appears at nearly the same wavelength as in the rhodium monomers (**2**,**3**,**4**). Nonradiative decay, a possible decay pathway of the ^{3}MLCT excited state, is accelerated with a decrease in the energy gap between the lowest lying excited state and the ground state, this effect is known as the energy gap law.[24] Since the Ru-based emission for the heterobimetallic complex (**1**) is of lower energy (778 nm) than in the parent monomer (**2**) (450 nm), the energy gap between the excited state and the ground state is decreased resulting in an increase in nonradiative decay. This nonradiative decay pathway should result in a significant increase in deactivation of the excited state. The emission energies of the complexes $[(bpy)_2Ru(dpp)Ru(bpy)_2]^{4+}$ (**5**) and (**1**), however, are very close, 790 nm, and 778 nm respectively. In this case the increase in nonradiative decay should be minimal because of the small change in energy gap. There is still a significant amount of quenching when comparing the two bimetallic compounds (**1**, **5**) as is evident from the decreased Φ^{em} in complex (**1**). Another possible source of quenching is intramolecular energy transfer. In some rhodium(III) molecules or components within larger molecules the lowest lying

excited state is populated through a ligand field (LF) d → d transition instead of the polyazine intraligand (IL) π → π* transition, as has been shown in Rh-terpyridine complexes.[21] In some Rh-terpyridine complexes the LF d → d state may be low enough in energy to act as an intramolecular energy acceptor of the excited Ru(II) fragment. However, from the energy state diagram, Figure 5, it is clear that the mononuclear Rh(III) complexes have higher lowest lying LF and IL states than the charge transfer (CT) state present in (**1**) and (**5**) by 0.5 eV. The large energy gap should impede thermal population of the LF state. Therefore energy transfer is expected to be an inefficient source of quenching, and intramolecular electron transfer is expected to be the main source of quenching in this system. This result is not surprising, as rhodium(III)-polyazine complexes have been shown to be efficient oxidative quenchers of the ruthenium(II)-polyazine excited states.[9-13] Complex **1'**s excited states were examined by transient absorption spectroscopy to confirm the identity of the electron-transfer products following optical excitation. However, the lifetime of the MMCT state was too short for any rhodium(II) based transient to be measured. This finding was ascribed to efficient

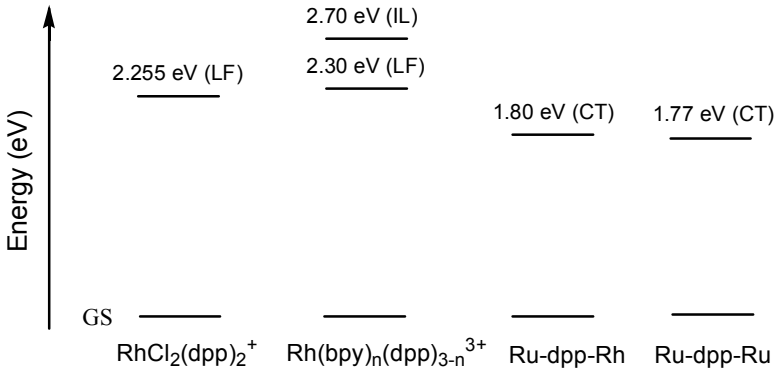

Figure 5. Energy state diagram of mononuclear Rh complexes and Ru-Ru and Ru-Rh binuclear complexes. LF is a ligand field state, IL is an intraligand state, and CT is a charge transfer state.[22]

back electron transfer. This study is an example depicting many of the excited state processes possible in a mixed metal complex consisting of ruthenium and rhodium including electron transfer to generate a MMCT state.[22]

2. *Electron Transfer in Rhodium Centered Supramolecular Complexes*

Much progress has been made over the past decade into the investigation of electron transfer in rhodium complexes. The various factors that play an important role in electron transfer will be discussed, such as the distance between metal centers in polymetallic complexes and the effect that bridging ligands have on the electronics of the system. There is great interest in this class of complexes due to their potential use in energy conversion schemes. The topic of electron transfer will be explored by considering various excited states in detail. MLCT states of ruthenium-polypyridyl units have been studied in detail and are the subject of discussion below. The less well studied MMCT state, which has been observed in polymetallic complexes of ruthenium and rhodium, is also examined below, which in some cases has been shown to form a long lived charge separated state. These charge separated states are important in designing multicomponent systems that are capable of multielectron transfer.

3. *Factors Impacting Electron Transfer Efficiency*

i. *Electronic Coupling*

The strength of electronic coupling between the donor and the acceptor is an important factor in determining the efficiency of energy and/or electron transfer. The

extent of electronic delocalization can be classified as follows. A system can either be valence-localized, i.e. M^{II}-M^{III}, M^{III}-M^{II} with no electronic coupling, or there can be orbital delocalization resulting in orbital mixing. The degree of orbital mixing can range from very weak, such that any mixing is essentially negligible (class 1), where the electronic behavior is essentially that of a valence localized system, Figure 6A, or there can be a strong degree of electronic coupling resulting in essentially one potential energy well (class 3), Figure 6C. Many real systems, however, lie between these two extremes. Electronic coupling is weak enough that the electron donor and acceptor essentially retain their individual molecular orbitals, but large enough that energy or electron transfer does occur (class 2), Figure 6B.[1]

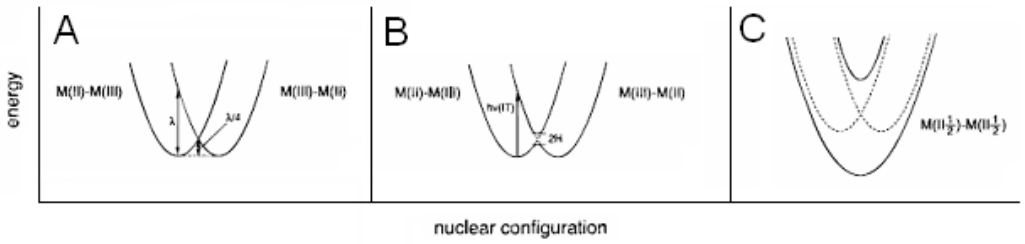

Figure 6. Potential energy curves for mixed-valence compounds with A) negligible, B) weak, and C) strong electronic coupling.[1] Reproduced with permission from Balzani, V; Juris, A; Venturi, M; Campagna, S; Serroni, S. *Chem. Rev*. **1996**, *96*, 759. Copyright 2007 American Chemical Society.

Coupling strength has been varied while the effects were monitored by measuring trends in excited state relaxation rates. In a series of experiments $[(bpy)_2Ru(CN)_2]$ was the donor, $[(CN\text{-}\mu\text{-})Rh(NH_3)_5](PF_6)_3$ was the acceptor, and the rhodium-ammine acceptor was covalently linked through the cyano group.[25] Coupling strength was first varied by changing the number of rhodium-amine acceptors attached to the ruthenium donor between zero and two. Rh(III) amine complexes are known to be good quenchers of

(^{3}MLCT) $[Ru(bpy)_2(CN)_2]$.[25] Increasing the number of $\{Rh(NH_3)_5\}^{3+}$ units is expected to increase quenching of the ^{3}MLCT state. The ^{3}MLCT state emission is shifted to higher energy (A, B, C) with each additional $\{Rh(NH_3)_5\}^{3+}$ acceptor, Figure 7, and at 77 K, the excited state lifetimes increase from 4.3 μs, 5.7 μs, and 8.4 μs, respectively.[25] This observation is the opposite of what was expected. One possibility is that the rhodium based LUMO is too high in energy to quench the ^{3}MLCT emission. Fast equilibration between the ruthenium and rhodium units' excited states are likely a contributing factor in this system. Further complicating matters, it was also found that the complex, $[(bpy)_2(CN)Ru(-\mu\text{-}CN\text{-}\mu\text{-})Rh(NH_3)_5](PF_6)_6$, photodecomposes in the spectrometer making definitive assignments difficult.[25]

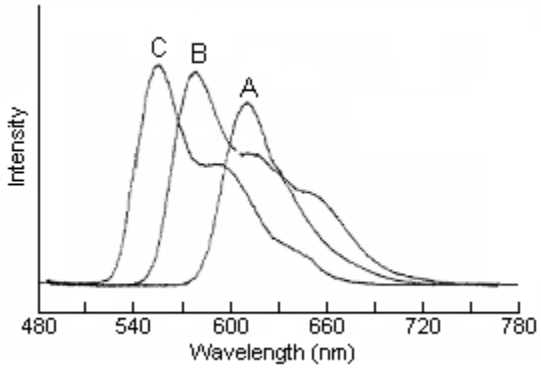

Figure 7. 77 K emission spectroscopy for a series of ruthenium-rhodium heterobimetallic complexes bridged by cyanide. A) $[(bpy)_2Ru(CN)_2](PF_6)$ λ_{abs}^{max} = 573 nm (bpy = 2,2'-bipyridine) B) $[(bpy)_2Ru(CN)(\mu\text{-}CN)Rh(NH_3)_5](PF_6)_3$ λ_{abs}^{max} = 556 nm C) $[(bpy)_2Ru\{(\mu\text{-}CN)Rh(NH_3)_5\}_2](PF_6)_6$ λ_{abs}^{max} = 543 nm.).[25] Reproduced with permission from Lei, Y; Buranda, T; Endicott, J. *J. Am. Chem. Soc.* **1990**, *112*, 8824. Copyright 2007 American Chemical Society.

ii. Reorganization energy

In designing photochemical molecular devices, efficient electron transfer is a desirable property. The electron transfer rate constant, k_{et}, is a function of the strength of electronic coupling, as stated previously, and also the reorganization energy of the

complex. The reorganization energy can be divided into two categories, outer sphere and inner sphere. The inner-sphere reorganization energy cannot be calculated due to the unknown nuclear configurations of the reactant and product states. Experiments, however, have shown that collisional ET rates for $Rh(L)_3^{3+}$-$Rh(L)_3^{2+}$ and $Ru(L)_3^{3+}$-$(^3CT)Ru(L)_3^{2+}$ (where L is a polypyridyl ligand such as bpy) self exchange is fast (2×10^9 M^{-1} s^{-1}) indicating that inner-sphere barriers are small (<0.1 eV). Thus, it can be assumed that the total reorganization energy is approximately equal to the outer-sphere reorganization energy.[26,27]

Electronic coupling and reorganization energy can be determined from the metal-to-metal charge transfer (MMCT) between the donor, i.e. a ruthenium chromophore, and an acceptor, i.e. rhodium. A series of complexes were synthesized of the type $[(bpy)_2Ru^{II}(L\text{-}L)Rh^{III}(bpy)_2](ClO_4)_5$ where (L-L) is $dpimbH_2$, $bpbimH_2$, dmbpbim, or dpbime, Figure 3.[27] Upon photo excitation of these compounds, it was determined that the ruthenium based ^{3}MLCT was rapidly quenched by electron transfer generating the species $*[(bpy)_2Ru^{III}(L\text{-}L)Rh^{II}(bpy)_2](ClO_4)_5$. This state then undergoes rapid decay by back electron transfer to regenerate the ground state complex $[(bpy)_2Ru^{II}(L\text{-}L)Rh^{III}(bpy)_2](ClO_4)_5$. The ^{3}MLCT lifetime was determined by measuring its rate of deactivation via phosphorescence and by transient absorbance spectroscopy. In this study it was found that the specific bridging ligand had little effect on the frequency factors indicating that electron transfer is an adiabatic process even though the electronic coupling is small. This can be rationalized by the fact that electron transfer couples to slow nuclear motions such as solvent reorientation.[27]

iii. Distance Dependence of Electronic Coupling and Reorganizational Energy

Both the extent of electronic coupling and the outer-sphere reorganization energy are a function of the distance between the electron donor and acceptor. Ohno prepared a series of complexes of the general form [(ttpy)Ru-tpy-$(ph)_n$-tpy-Rh(ttpy)]$(PF_6)_5$ (n=0,1,2; Ru-Rh binuclear complexes (**6**, **7**, **8**)) in order to explore the effects of distance on coupling, Figure 8.[27] Some advantages exist with this system over previously studied systems. Terpyridine, a tridentate ligand, allows for the formation of stereochemically defined complexes as opposed to bidentate ligands where complications can arise from the formation of many more stereoisomers, especially in trimetallic and larger

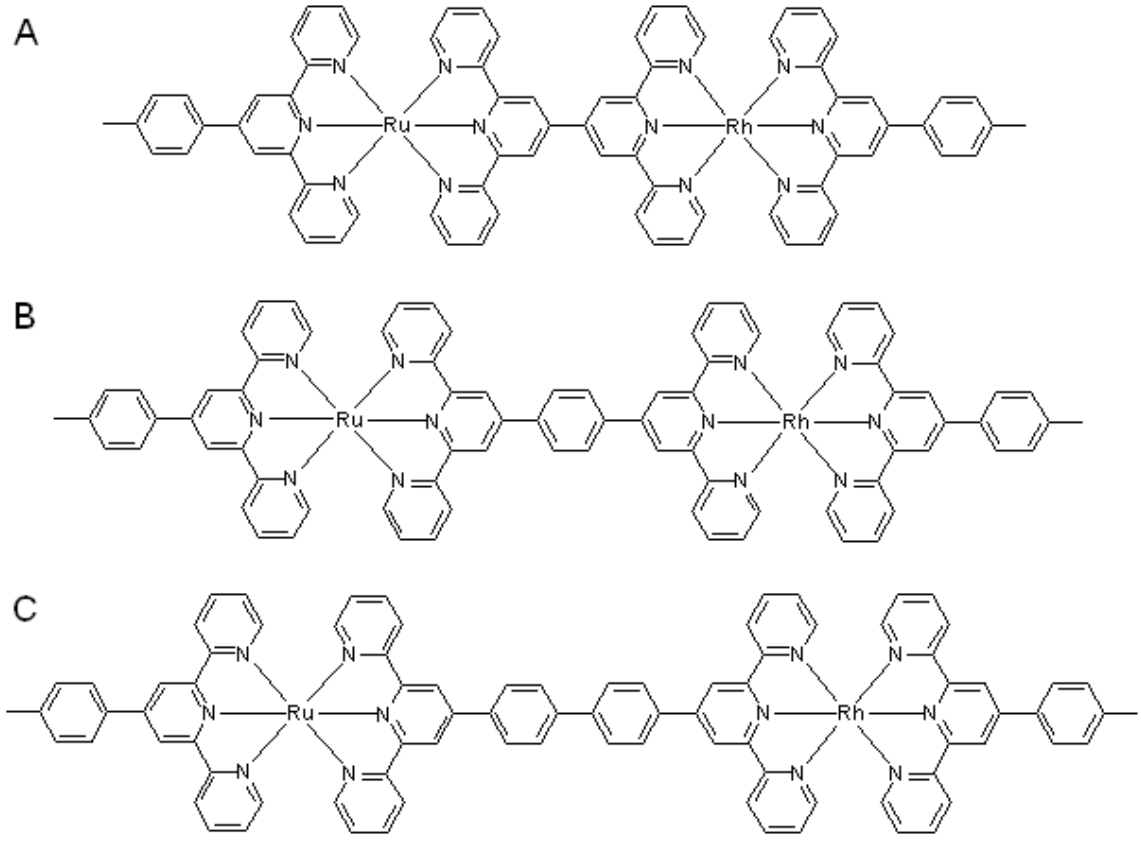

Figure 8. A series of Ru-Ru bimetallic complexes of the form [(ttpy)Ru(tpy-$(C_6H_4)_n$-tpy)Ru(ttpy)]$(PF_6)_5$ (tpy = 4'-p-tolyl-2,2':6,2"-terpyridine) with n phenylene spacers, where A) n = 0, complex **6**, B) n = 1, complex **7**, and C) n = 2, complex **8**.[27] Reproduced with permission from Nozaki, K; Ohno, T; Haga, M. *J. Phys. Chem*. **1992**, *96*, 10880. Copyright 2007 American Chemical Society.

polymetallic complexes. Also, by varying the number of phenylene spacers, the metal-metal distance can be controlled. In this system, metal-metal distances range from 1.1 to 2.0 nm. $Ru(ttpy)_2^{2+}$ (**9**) (1.49 V) indicating a decrease in electronic coupling. There is also a very small cathodic shift in the reduction potentials corresponding to the $Rh^{III/I}$ reduction, -0.30 V (**6**), -0.32 V (**7**), and -0.32 V (**8**) with increasing metal-metal distance (Table 1). Emission experiments were carried out to examine the excited state properties of **6**, **7**, and **8**. All of the complexes are weak emitters at 300 K, so fluid solution measurements were all measured at 150 K. Emission spectra were also recorded in a rigid matrix at 77 K. At both temperatures all of the Ru-Rh complexes (**6**, **7**, **8**) exhibit Ru-based emissions. At 150 K the emission of complex **6** (n=0) is greatly red-shifted (λ = 720 nm) with respect to **9** (λ = 645 nm) and close to the Ru-Ru bimetallic model $[(ttpy)Ru(tpy\text{-}tpy)Ru(ttpy)]^{4+}$ (complex **10**). This data, along with the comparison of the emission quantum yield of $[(ttpy)Ru(tpy\text{-}tpy)Rh(ttpy)]^{5+}$ (**6**) with the Ru-Ru model $[(ttpy)Ru(tpy\text{-}tpy)Ru(ttpy)]^{4+}$ (**10**) indicates that there is efficient quenching in complex **6** at 150 K.

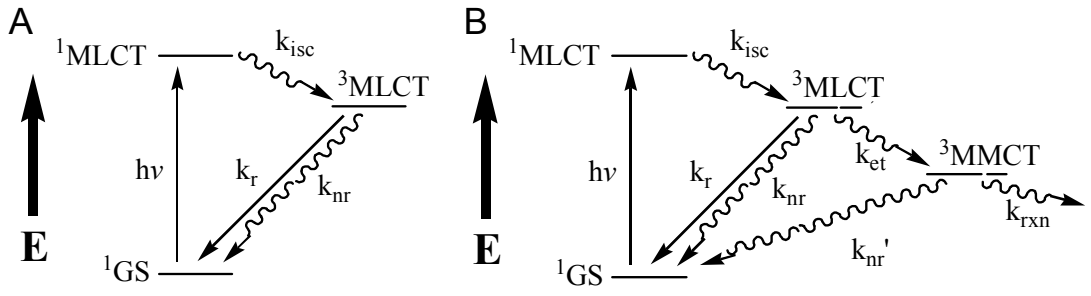

Figure 9. Energy state diagram for the model complex A) $[(ttpy)Ru(tpy\text{-}tpy)Ru(ttpy)]^{4+}$ (tpy = 4'-p-toyl-2,2':6,2"-terpyridine) and the complexes B) $[(ttpy)Ru(tpy\text{-}(ph)_n\text{-}tpy)Rh(ttpy)]^{5+}$ (n= 0,1,2).

The emissions of complexes **7** and **8** had the same intensity as the Ru model indicating that there is no quenching of the Ru-based excited state at this temperature, Table 1. At 77 K all three of the Ru-Rh complexes' (**6**, **7**, **8**) emission intensities match the Ru model (**9**) indicating that all three complexes have no quenching of the ^{3}MLCT Ru-based excited state. Complexes **7** and **8** (n = 1, 2) have almost identical absorption and emission spectra as the mononuclear Ru model (**9**) and has been shown to not undergo electron transfer quenching at any temperature. Electron transfer quenching could only be observed for the Ru-Rh complex **6** (n=0) at 150 K, making it impossible to probe the distance dependence in this series of complexes.[28] Since the lifetime of the Ru(II) → terpyridine ^{3}MLCT excited state is less than a nanosecond, due to thermal population of the ligand field state in complexes **7** and **8** (n=1,2), electron transfer occurs too slowly to compete with other excited state relaxation processes, i.e. radiative and nonradiative decay.[29] Ligands with longer lived MLCTs are needed to study the effects of bridge lengths or greater coupling between electron donor and acceptor are needed. Pyrazine based bridging ligand complexes like dpp and tpp, Figure 3, have been found to exhibit long lived ^{3}MLCT which make them attractive for further study.

The bridging ligand tpp, Figure 3, has been used in the hetero-bimetallic complex $[(tpy)Ru(tpp)RhCl_3]^{2+}$ (complex **11**) where tpp is a bis-tridentate bridging ligand similar in structure to tpy but having different electronic properties.[30] Pyrazine based bridging ligands have lower energy ^{3}MLCT excited states, increasing the separation between the ^{3}MLCT and the ^{3}LF state, which limits thermal population into the ^{3}LF state. This change results in longer lived Ru-bridging ligand charge transfer states. Complex **11** undergoes electron transfer quenching at room temperature shortening the lifetime by

about 80%. Unlike the previous system (complexes **7**, **8**) the lifetime of **11** is still long enough to be measured. At 77 K quenching is no longer observed and the lifetime becomes approximately equal to that of the bimetallic complex $[(tpy)Ru(tpp)Ru(tpy)]^{4+}$. This study shows that the (tpy)Ru(μ-tpp) chromophore is a promising component in designing photochemical molecular devices.[30]

All of the Ru-Rh heterobimetallic systems examined thus far contain a chromophore that functions as an excited state electron donor and a Rh quencher that acts as an electron acceptor. Another study of a two component "dyad" and its accompanying intramolecular electron and energy transfer processes utilized the complex $[(Me_2phen)_2Ru(Mebpy\text{-}CH_2\text{-}CH_2\text{-}Mebpy)Rh(Me_2bpy)]^{5+}$ (**12**), Figure 10. This complex has unusual behavior in that both the electron donor and acceptor are chromophoric, that is they are both photoexcitable. This affords the investigation of a number of intermolecular electron and energy transfer pathways, some of which do not occur in the usual systems, Figure 11. The processes that are investigated are

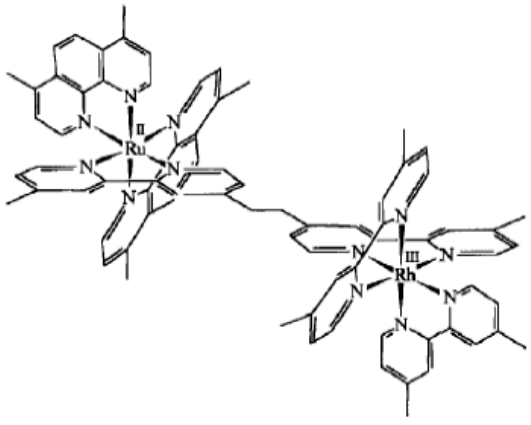

Figure 10. A Ru-Rh bimetallic complex of the form $[(Me_2phen)_2Ru^{II}(Mebpy\text{-}CH_2\text{-}CH_2\text{-}Mebpy)Rh^{III}(Me_2phen)_2]$ (Me_2phen = 4,7-dimethyl-l,l0-phenanthroline; Mebpy-CH_2-CH_2-Mebpy = 1,2-bis[4-(4'-methyl-2,2'-bipyridinyl)]ethane).[31] Reprinted from Scandola, F; Argazzi, R; Bignozzi, C; Indelli, M. *J. Photochem. Photobiol*. **1994**, *82*, 191 with permission from Elsevier.

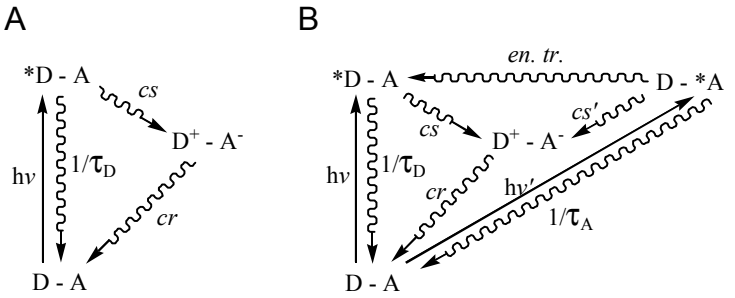

Figure 11. Intercomponent processes in A) a typical electron donor-acceptor framework, and B) in a system capable of exiting both the donor and the acceptor. *cs* is charge separated state, *cr* is charge recombination (back electron transfer), *en. tr.* is energy transfer.

1. electron transfer from the excited Ru donor to the Rh acceptor
2. electron transfer from the Ru donor to the excited Rh acceptor
3. back electron transfer from the reduced Rh acceptor to the oxidized Ru donor
4. energy transfer directly from the excited Rh acceptor to the Ru donor

Flash photolysis was employed and excited state lifetimes were measured in order to determine the rates of various excited state processes. The rate of energy transfer from the excited acceptor to the donor was determined from the lifetime at 77 K. At this temperature the very fast electron transfer process ($k_{et} = 3.3 \times 10^{10}$ s^{-1}; electron transfer rate constant) is completely suppressed making it possible to measure the rate of the much slower energy transfer process ($k_{en.\,tr.} < 1.9 \times 10^{6}$ s^{-1}; energy transfer rate constant).[31] Knowing the relative rates of these intermolecular processes may make it possible to take the next step, adding a third transition metal fragment. A trimetallic complex could be designed to have two chromophoric electron donors and a central rhodium polypyridyl fragment. Complexes containing multiple light absorbers with the correct electronics could potentially undergo multi-electron processes. In such a system

where multiple electron transfers do occur, the central rhodium unit could be considered an electron collector. The importance of these multimetallic systems lies in their potential to function as multielectron catalysts. For multielectron processes to be possible though, the second reduction of the rhodium unit generating the doubly reduced rhodium(I) unit must take place faster than back electron transfer. For a complex of similar design to complex **12**, this would require the second electron transfer to occur within 140 ps.[31] An alternative method to make photoinitiated multielectron collection feasible could involve the use of an electron donor to reductively quench the excited state to limit back electron transfer. In addition, the supramolecular architecture may require modification such that back electron transfer could be slowed to allow for reductive quenching of the excited complex.

C. Photoinitiated Electron Collection

The conversion of light energy into chemical energy is of great interest, with particular focus on the development of efficient solar energy conversion schemes. The MLCT excited states of ruthenium-polyazine complexes have found widespread use in this area.[32-35] Multielectron photocatalysis is a key component of schemes that convert light energy into fuels. Both solar water splitting and light-driven carbon dioxide reduction involve multielectron reactions. Much work has focused on the development of complex supramolecular assemblies for light harvesting and directional charge separation.[36-39] Very few homogeneous systems have been studied that use light to perform multielectron reactions or collect multiple reducing equivalents.[39-50]

Photoinitiated electron collection is a process where light energy is used to collect reducing equivalents. This multielectron photochemistry has been of interest in harvesting light energy as a means to produce multielectron-reduced substrates including fuels. A system for photoinitiated electron collection must efficiently absorb light, undergo efficient successive and/or multiple electron transfer(s), and be stable in the multielectron-reduced form. Meeting all of these requirements makes the realization of a functional photoinitiated electron collector (PEC) difficult. Building block units commonly employed in the construction of photochemical molecular devices include LAs, BLs, EAs, EDs and ECs.

The first functioning photoinitiated electron collector was reported by Brewer and coworkers, employing π systems of polyazine bridging ligands to collect electrons, of the form $[\{(bpy)_2Ru(dpb)\}_2IrCl_2]^{5+}$.[39] This trimetallic complex incorporates two light-absorbing units covalently attached to a central iridium center. The supramolecular architecture, LA-EC-LA, is designed to allow two separate photoinitiated electron-

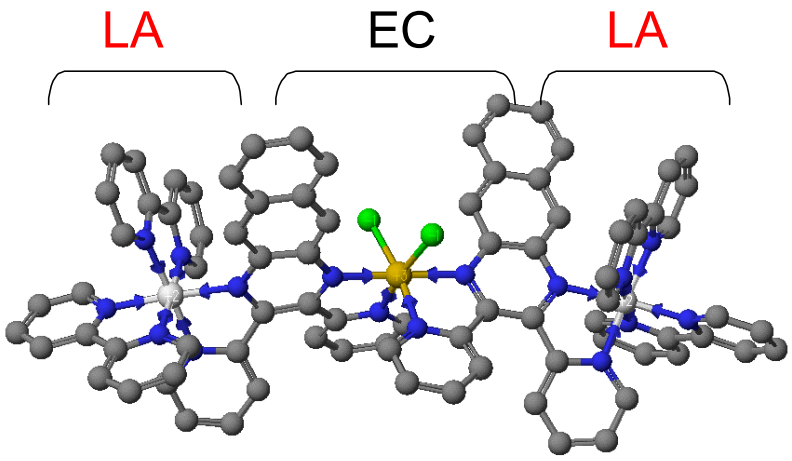

Figure 12. CAChe generated structure for the photoinitiated electron collector $[\{(bpy)_2Ru(dpb)\}_2IrCl_2]^{5+}$ (bpy = 2,2'bipyridine; dpb = 2,3-bis(2-pyridyl)benzoquinoxaline) depicting the light absorbing units and the electron collecting bridging ligands. Each dpb bridging ligand can collect one electron.[39]

transfer steps to occur which can lead to electron collection. Photolysis of this complex in the presence of an electron donor leads to the generation of the doubly reduced species, $[\{(bpy)_2Ru(dpb^-)\}_2IrC1_2]^{3+}$. Following photolysis, the central iridium core has two reduced dpb bridging ligands coordinated to it. It has also been previously shown that the central core, $[Ir(dpb)_2C1_2]^+$, can interact with a substrate by transferring electrons "stored" on the bridging ligands.[40] This is the first reported example of a complex that can photochemically collect multiple electrons.

Another system that incorporates two ruthenium polyazine light absorbers and a highly conjugated bridging π system as an electron collector was reported by MacDonnell and Campagna.[41-43] This study involved a pair of bimetallic Ru complexes of the form $[(phen)_2Ru(BL)Ru(phen)_2]^{4+}$, where BL is tatpp (phenanthroline-pyrazine-benzene-pyrazine-phenanthroline) or tatpq (phenanthrolinepyrazine-quinone-pyrazine-phenanthroline), Figure 13, that photochemically collect two or four electrons respectively. Upon absorption of light an electronic transition from a ruthenium dπ

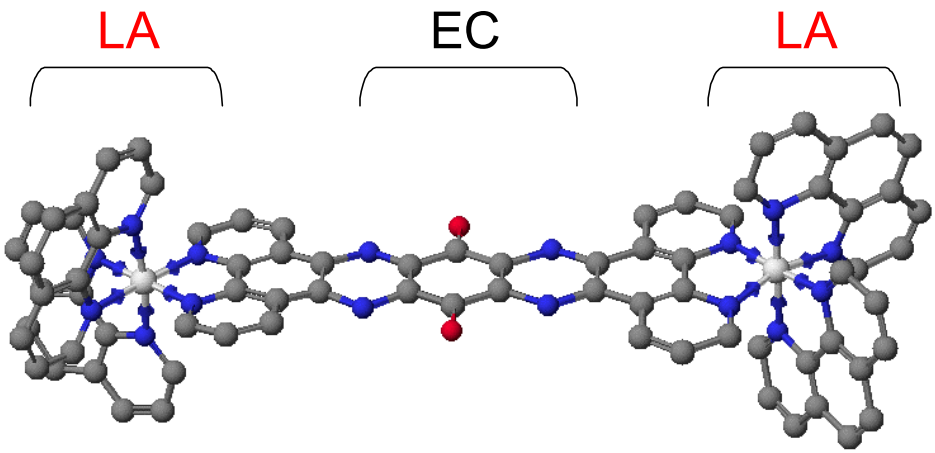

Figure 13. CAChe generated structure for the photoinitiated electron collector $[(phen)_2Ru(tatpq)Ru(phen)_2]^{4+}$ depicting the light absorbing units and the electron collecting bridging ligand. The tatpq bridging ligand (tatpq = phenanthrolinepyrazine-quinone-pyrazine-phenanthroline) can collect up to four electrons.[43]

orbital to a phen type π* orbital takes place followed by an electron transfer to a lower lying delocalized π* orbital located on the bridge. Photolysis of $[(phen)_2Ru(tatpp)Ru(phen)_2]^{4+}$ or $[(phen)_2Ru(tatpq)Ru(phen)_2]^{4+}$ in the presence of an electron donor leads to the formation of the two and four electron-reduced species, respectively. This example makes use of the LA-EC-LA supramolecular architecture where optical excitation takes place into a higher energy phen type π* orbital followed by electron transfer to a lower lying delocalized orbital located on the EC. The tatpq bridged complex has been shown to undergo photoinitiated electron collection and store up to four electrons on the bridge in the presence of an electron donor.[41-43]

Bocarsly and co-workers have also studied a system of the LA-EC-LA design consisting of two group eight transition metal light absorbers bridged by two cyanides to a platinum(IV) metal center.[48-50] The supramolecular architecture is of the form $[\{(NC)_5M^{II}(CN)\}_2Pt^{IV}(NH_3)_4]^{4-}$ where M is Fe, Ru, or Os. These promising systems have been shown to undergo photoinitiated electron transfer. When the light absorber contained an iron metal center the absorption of a single photon resulted in a two electron transfer to the platinum(IV) metal center. Once the platinum is reduced by two electrons it is no longer stable in an octahedral coordination environment. This instability results in fragmentation of the complex into two oxidized iron(III) LAs and a reduced platinum(II) complex which dissociates, limiting its use as a catalyst. This is the first reported example of using a LA-EC-LA supramolecular architecture to collect multiple reducing equivalents on a central metal.[48-50]

In a deviation from the LA-EC-LA structural motif for photoinitiated electron collection, Nocera designed an interesting system consisting of a rhodium-rhodium intervalence charge transfer species capable of undergoing interesting multielectron photochemistry.[44-47] Nocera's design is capable of photocatalytic hydrogen production from hydrohalic acid. One of the complexes studied was of the form $[(PPh)_3Rh^0$-$Rh^0(dfpma)_3(CO)]$, where dfpma is $MeN(PF_2)_2$, Figure 14. The dfpma ligand is key in the functioning of this system in that it helps stabilize the intervalence charge transfer state that is generated upon the absorption of light. This ligand stabilizes the intervalence charge transfer state by donating electron density via one of the difluorophosphines bound to the rhodium in the higher oxidation state. The central nitrogen in turn donates electron density to the difluorophosphine that acts as a sigma donor. Finally, the other difluorophosphine donates electron density to the central nitrogen, which then can act as a π backbonder to the rhodium in the lower oxidation state, Figure 15. These ligands help create the electronic environment for the mixed valence state to remain stable which is the key for this system to undergo multielectron chemistry.[44-47] Also see section IV. D. 4 for information on this system as it relates to hydrogen photocatalysis.

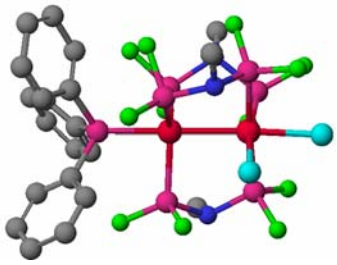

Figure 14. CAChe generated structure for the rhodium-rhodium intervalence charge transfer complex $(Ph_3P)Rh^0(dfpma)_3Rh^{II}Br_2$ (dfpma = $MeN(PF_2)_2$), a catalyst for hydrogen production from hydrohalic acid.[47]

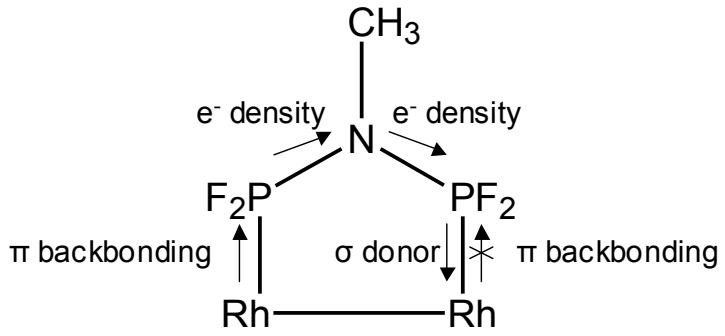

Figure 15. The ligand dfpma (dfpma = $MeN(PF_2)_2$) bound to two rhodium metals depicting the electronic effects through σ donation, π backbonding and the shifting of electron density around the central nitrogen.

D. Methods for Hydrogen Generation

1. Alternative Energy Sources

The need for renewable energy sources has driven an exploration for alternative energy. One major source of energy utilized by civilization is the light energy that reaches the earth from the sun. This solar energy is currently harvested through photosynthesis by plants. Solar energy is harnessed by plants, which is then utilized by animals as biomass or degrades to produce hydrocarbon reserves. The rate of our use of fossil fuels makes it necessary to explore alternative means to harness this solar energy or other alternative energy sources. One appealing alternative energy source is solar energy, harnessed without the use of plants. The energy demands of humanity have fostered an interest in the design of artificial systems to harvest solar energy. The harvesting of solar energy can occur through the conversion of light energy into heat energy in thermal conversion schemes, or electrical potentials in solar cells, or fuels through light to chemical energy conversion schemes. The conversion of light energy into a fuel focuses on the conversion of a widely available chemical feedstock into a transportable fuel. The

chemical feed stocks commonly suggested are carbon dioxide (via artificial photosynthesis) and water (via solar water splitting). Water is an attractive chemical feedstock for solar energy conversion as the fuel produced is hydrogen. Hydrogen is an attractive fuel with a standard heat of combustion, $\Delta H_c°$, of 285.8 kJ/mol.[51] Combustion of hydrogen is the highest energy content per mass, 285.2 kJ/g,[51] of a non nuclear, chemical reaction. Methods for generating hydrogen have been intensely studied for several decades for a number of reasons, the combustion by-product is water so the environmental impact is negligible, the high energy content, and many methods for generating hydrogen are renewable in nature. Since the volume of work in this field is vast, this discussion will be limited to hydrogen generation methods using rhodium based systems.

2. *Photocatalytic H_2 production using Rh-centered Supramolecular Complexes*

Solar hydrogen production[52-54] has received much attention in contemporary photochemical research. Solar energy is of sufficient energy to drive the splitting of water to hydrogen and oxygen.[55,56] Since water does not absorb in the visible region of the spectrum, a suitable photochemical agent must be used to absorb and utilize light to drive reactions.

In the late 1970s and early 1980s studies initially by Sauvage[7,8] and subsequently by Creutz[9-13] showed that a bimolecular heterogeneous system of $[Ru(bpy)_3]^{2+}$ (bpy- 2,2'-bipyridine), $[Rh(bpy)_3]^{3+}$ and platinum can produce dihydrogen photochemically. In this photocatalytic system the light absorber, $[Ru(bpy)_3]^{2+}$, absorbs visible light resulting in the formation of a Ru → bpy ^{3}CT excited state (rxn1). Following excitation, the excited

*$[Ru(bpy)_3]^{2+}$ complex can then be oxidized by $[Rh(bpy)_3]^{3+}$, an electron acceptor (EA), resulting in the oxidation of $[Ru(bpy)_3]^{2+}$ and the reduction of $[Rh(bpy)_3]^{3+}$ (rxn2).

$$[Ru(bpy)_3]^{2+} \rightarrow *[Ru(bpy)_3]^{2+} \quad \text{(rxn1)}$$

$$*[Ru(bpy)_3]^{2+} + [Rh(bpy)_3]^{3+} \rightarrow [Ru(bpy)_3]^{3+} + [Rh(bpy)_3]^{2+} \quad \text{(rxn2)}$$

$$[Ru(bpy)_3]^{3+} + TEOA \rightarrow TEOA^{+} + [Ru(bpy)_3]^{2+} \quad \text{(rxn3)}$$

$$[Rh(bpy)_3]^{2+} + [Rh(bpy)_3]^{2+} \rightarrow [Rh(bpy)_3]^{+} + [Rh(bpy)_3]^{3+} \quad \text{(rxn4)}$$

$$[Rh(bpy)_3]^{2+} + H_2O \xrightarrow{Pt} [Rh(bpy)_3]^{3+} + {}^1/_2H_2 + OH^- \quad \text{(rxn5)}$$

Triethanolamine (TEOA), a sacrificial donor, then reduces $[Ru(bpy)_3]^{3+}$ to limit electron transfer with $[Rh(bpy)_3]^{2+}$ (rxn3). $[Rh(bpy)_3]^{2+}$ can then disproportionate to generate the rhodium(I) and rhodium(III) complexes, $[Rh(bpy)_3]^{+}$ and $[Rh(bpy)_3]^{3+}$ (rxn4) or through a radical process, $[Rh(bpy)_3]^{2+}$ can produce H_2 in the presence of heterogeneous platinum (rxn5).[9-13] This system demonstrated the ability of rhodium to act as an electron acceptor and in the presence of a heterogeneous platinum catalyst can act as an electron relay in a system for photocatalytic hydrogen production. These early results showed the potential for ruthenium-rhodium electron transfer systems in photochemical energy conversion schemes and have provided inspiration for continued work in supramolecular chemistry for hydrogen photocatalysis.

3. *Hydrogen Catalysisc using Wilkinson's Catalyst, $[RhCl(dpm)_3]^{3-}$*

A homogeneous system consisting of the light absorbing moiety, $[Ru(bpy)_3]^{2+}$, and a water-soluble Wilkinson's complex, $[Rh^{I}Cl(dpm)_3]^{3-}$ (dpm = diphenylphosphinobenzene-m-sulphonate), was examined by Oishi as a catalyst for the reduction of water using ascorbic acid (represented here as AH_2) as the sacrificial

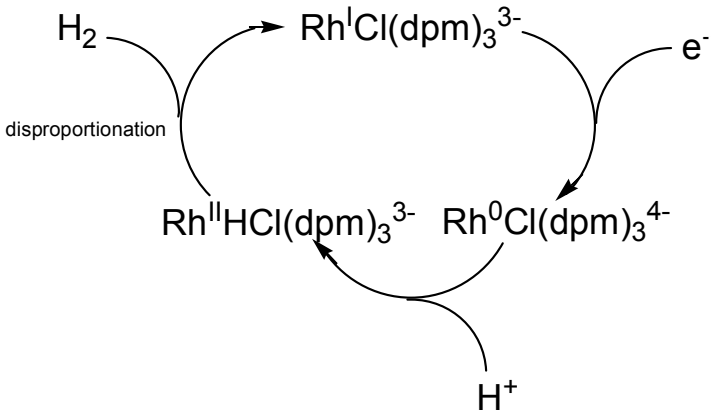

Figure 16. Catalytic cycle for the homogenous generation of hydrogen using a water soluble Wilkinson's catalyst and the light absorbing species $[Ru(bpy)_3]^{3+}$ (bpy = 2,2'-bipyridine).

electron donor, Figure 16.[57] At pH 5 with 440 nm irradiation, the system was reported to have a high quantum yield, $\Phi = 0.30$, for H_2 production. A kinetic analysis determined that the rate limiting step was either the reduction of $[Ru(bpy)_3]^{2+}$ by ascorbate (rxn7) or electron transfer from the reduced ruthenium light absorber to the rhodium(I) complex (rxn8). This analysis also indicated that the part of the catalytic cycle involving the rhodium complex is almost quantitative, i.e. the quantum yield for reactions 9 and 10 is

$$[Ru(bpy)_3]^{2+} \rightarrow *[Ru(bpy)_3]^{2+} \quad \text{(rxn6)}$$

$$*[Ru(bpy)_3]^{2+} + AH^- \rightarrow [Ru(bpy)_3]^{+} + AH^{\bullet} \quad \text{(rxn7)}$$

$$[Ru(bpy)_3]^{+} + [Rh^{I}Cl(dpm)_3]^{3-} \rightarrow Ru(bpy)_3]^{2+} + [Rh^{0}Cl(dpm)_3]^{4-} \quad \text{(rxn8)}$$

$$[Rh^{0}Cl(dpm)_3]^{4-} + H^{+} \rightarrow [Rh^{II}HCl(dpm)_3]^{3-} \quad \text{(rxn9)}$$

$$2\,[Rh^{II}HCl(dpm)_3]^{3-} \rightarrow 2\,[Rh^{I}Cl(dpm)_3]^{3-} + H_2 \quad \text{(rxn10)}$$

near unity, while the overall quantum yield is 0.30. Cyclic voltammetry, laser flash photolysis and pulse radiolysis were used to study the catalysis mechanism. These studies indicate the presence of a Rh(II)-hydride species as an intermediate in the catalytic cycle for the generation of hydrogen.[57]

This homogeneous system for the photochemical production of hydrogen consisting of the light absorbing moiety, $[Ru(bpy)_3]^{2+}$, and a water-soluble Wilkinson's complex, $[Rh^{I}Cl(dpm)_3]^{3-}$ was subsequently studied by Werner.[58] In the presence of the electron donor ascorbic acid and oxygen this system has a turn-over of more than 2000. Mass spectroscopy experiments also showed that the hydrogen produced originated from water as opposed to ascorbic acid.[58] Despite the relatively high quantum yield and turnover this is not a cost effective method for producing hydrogen and the rate limiting step is diffusion controlled due to the bimolecular nature of the system.

4. Photocatalytic H_2 production Using Rh-Rh Mixed Valence Complexes

Nocera has studied a series of intervalence charge transfer complexes, also see section IV. C.[44-47] One of the complexes studied was of the form $[(PPh)_3Rh^0Rh^0(dfpma)_3(CO)]$, where dfpma is $MeN(PF_2)_2$. This system enters the catalytic cycle upon absorption of light resulting in the photodissociation of CO. This is followed by coordination of hydrohalic acid and a disproportionation reaction to yield hydrogen. In the presence of a halogen-atom trap, the catalytically inactive species $[(PPh)_3Rh^0\text{-}Rh^0(dfpma)_3X_2]$ (X = halogen), that is a result of the disproportionation reaction can be activated to reenter the catalytic cycle as the species $[(PPh)_3Rh^0\text{-}Rh^0(dfpma)_3]$. The catalytic cycle is shown in Figure 17.

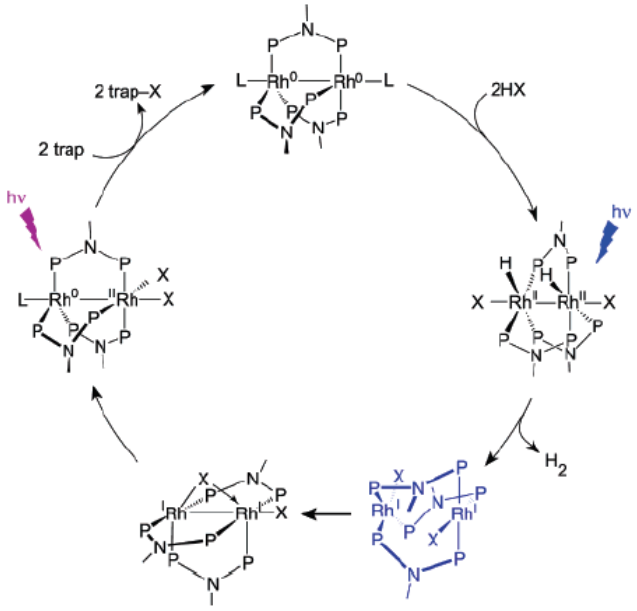

Figure 17. Catalytic cycle for the homogeneous production of hydrogen using the intervalence charge transfer complex $[(PPh)_3Rh^0\text{-}Rh^0(dfpma)_3(CO)]$ from hydrohalic acid (HX). The intervalence charge transfer is photoinitiated resulting in the coordination of hydrohalic acid. The active catalyst is regenerated with a halogen trap.[46] Reproduced with permission from Dempsey, J.; Esswein, A.; Manke, D.; Rosenthal, J.; Soper, J; Nocera, D. *Inorg. Chem*. **2005**, *44*, 6879. Copyright 2007 American Chemical Society.

II. Problem Addressed

The visible region of the solar spectrum is of sufficient energy to drive only the multielectron splitting of water necessitating the use of a photocatalyst capable of multielectron photochemistry. This problem can be addressed using a supramolecular architecture designed to function as a photoinitiated electron collector.

III. Experimental – Materials and Synthesis

A. Materials

Materials used for synthesis and chromatography included the following solvents which were used without further purification. HPLC grade acetonitrile and toluene were purchased from Fisher Scientific. High purity N,N-dimethylformamide (>99.99%) was purchased from Omnisolve. Industrial grade ethyl alcohol, 200 proof, was purchased from Aaper and deionized water was prepared in house.

The following materials were used for synthesis without additional purification. ReagentPlus 2,2'-bipyridine (>99%), and 2,3-bis(2-pyridyl)pyrazine (98%) were purchased from Aldrich. $RhCl_3 \cdot xH_2O$ (39-41% assay) and $RuCl_3 \cdot xH_2O$ (99%) were purchased from Alfa Aesar. KPF_6 (98%), NH_4PF_6 (99.99%), and LiCl (>98%) were purchased from Aldrich.

B. Synthesis

Synthesis of the supramolecular complex, $[\{(bpy)_2Ru(dpp)\}_2RhCl_2](PF_6)_5$, takes place via a building block approach, first prepared by Brewer.[39] The monometallic complex, $[(bpy)_2RuCl_2]$, was prepared using a procedure established by Meyer,[59] followed by the preparation of the monometallic complex $[(bpy)_2Ru(dpp)](PF_6)_2$, using a modified procedure of one originally developed by Gafney.[14] Many of the experimental methods discussed here employ electronic absorption spectroscopy and/or emission spectroscopy. Some of the building blocks used in the synthesis of the trimetallic complex have high quantum yields of emission that can become highly emissive impurities in subsequent synthetic steps. Additional purification procedures were

employed to ensure the purity of the title complex $[\{(bpy)_2Ru(dpp)\}_2RhCl_2](PF_6)_5$ was sufficient for emission spectroscopy.

1. Synthesis of $[(bpy)_2RuCl_2]$

The precursor $[(bpy)_2RuCl_2]$ was prepared via the method established by Meyer[58] with modifications to purification. A mixture of $RuCl_3 \bullet 3H_2O$ (7.80 g, 29.8 mmol), bpy (9.36 g, 60.0 mmol), and LiCl (8.4 g, 2.0 mmol) were heated at reflux in 50 mL DMF for 8 hours. The reaction mixture was allowed to cool to room temperature followed by the addition of 250 mL acetone and cooled overnight at 0˚ C. Red crystals were collected by vacuum filtration followed by washing with water. The crude product, $[(bpy)_2RuCl_2]$, was monitored by emission spectroscopy as it was purified by washing with H_2O. The primary impurity, $[Ru(bpy)_3]^{2+}$, is a chromophore with high quantum yield of emission, $\Phi^{em} = 0.068$.[6] It is necessary to remove this impurity until it is no longer detectable by emission spectroscopy. Additional washing with H_2O is necessary until there is no longer an observable emission at 605 nm[6] resulting in a product with >99.95% purity with respect to the emissive impurity $[Ru(bpy)_3]^{2+}$.

2. Synthesis of $[(bpy)_2Ru(dpp)](PF_6)_2$

Synthesis of the monometallic complex $[(bpy)_2Ru(dpp)](PF_6)_2$, takes place via a modified version of one developed by Gafney.[14] The purified precursor, $[(bpy)_2RuCl_2]$, (2.07 g, 4.28 mmol) and dpp (1.46 g, 6.24 mmol) are heated at reflux in a solution of 2:1 $EtOH/H_2O$ for 3 hours followed by precipitation in an approximately 50% saturated aqueous KPF_6 solution. Column chromatography is used for purification of the crude

product. A solution of 3:2 toluene/CH_3CN is used as the mobile phase and adsorption alumina is used as the solid phase. An orange band elutes first which is identified as the product. A purple band, identified as the bimetallic complex $[(bpy)_2Ru(dpp)Ru(bpy)_2](PF_6)_4$, adsorbs to the stationary phase. Column chromatography was repeated twice to obtain a product of higher purity. Upon addition of the sample to the third column the purple bimetallic band that adsorbs to the stationary phase was not observed. Purity with respect to the primary byproduct $[(bpy)_2Ru(dpp)Ru(bpy)_2](PF_6)_4$ was determined by cyclic and square wave voltammetry which can typically detect as little as 5% of electroactive impurities.

3. Synthesis of $[\{(bpy)_2Ru(dpp)\}_2RhCl_2](PF_6)_5$

Synthesis of the trimetallic complex $[\{(bpy)_2Ru(dpp)\}_2RhCl_2](PF_6)_5$ proceeds via a building block approach first reported by Brewer with subsequent modifications, figure 18.[39] Stoichiometry is a critical factor in synthesizing the complex in high purity. Theoretically, two parts of ruthenium monometallic $[(bpy)_2Ru(dpp)](PF_6)_2$, are needed for every one part of rhodium. Using excess ruthenium monometallic is undesirable as it will remain unreacted and provide an intense emission as an impurity. Generation of the tetrametallic complex appears unlikely as determined by electrochemical analysis of the product of a 3:1 reaction of the monometallic complex with rhodium. To minimize the emissive impurity attributed to unreacted monometallic complex, the stoichiometric ratio of monometallic complex to rhodium can be decreased to less than 2:1. This could possibly, however unlikely, lead to the generation of another impurity suspected to be the ruthenium-rhodium bimetallic complex, $[(bpy)_2Ru(dpp)RhCl_{2-n}X_{2+n}]^{3+n}$ (n = 0, 1, or 2)

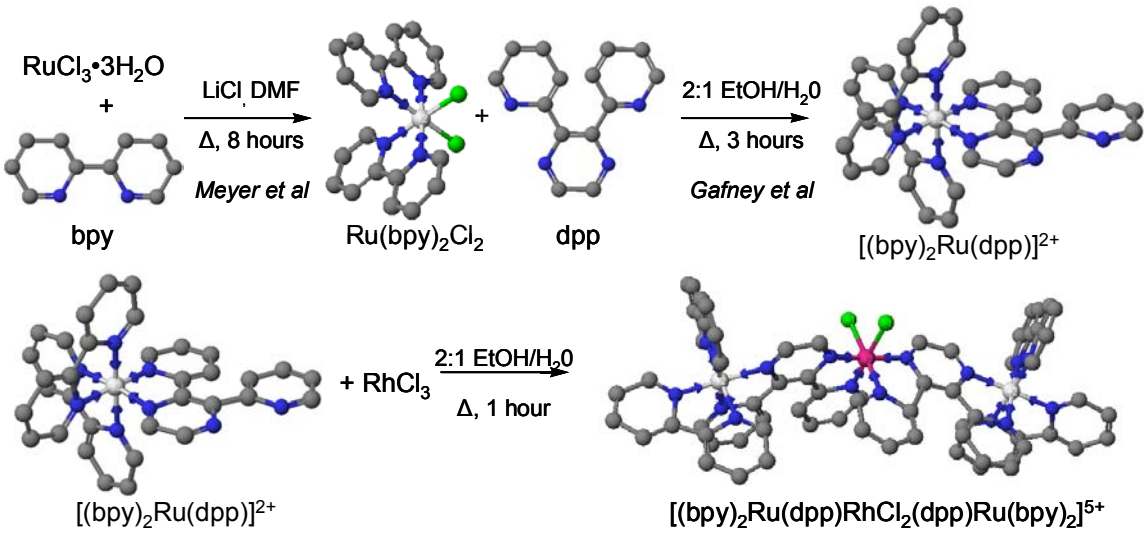

Figure 18. Synthetic scheme for the building block synthesis of $[\{(bpy)_2Ru(dpp)\}_2RhCl_2](PF_6)_5$ (bpy = 2,2'-bipyridine; dpp = 2,3-bis(2-pyridyl)pyrazine)[39] including the synthesis of the monometallic precursors $Ru(bpy)_2Cl_2$,[58] and $[(bpy)_2Ru(dpp)](PF_6)_2$.[14]

where X can be any combination of CH_3CN and H_2O. Rhodium monochelated complexes are difficult to isolate, however, the ruthenium-rhodium bimetallic complex is an intermediate along the path to formation of the trimetallic complex, so it is likely at least a minimal amount of the intermediate species is present. There is some electrochemical data that indicates the bimetallic species could be a larger contributing impurity, but it is inconclusive. Purification is discussed in more detail below. The stoichiometry with the best results for minimizing both the unreacted monometallic impurity and the impurity suspected to be the ruthenium-rhodium bimetallic complex, was found to be 1.8:1.

Synthesis of the trimetallic complex $[\{(bpy)_2Ru(dpp)\}_2RhCl_2](PF_6)_5$ takes place by the addition of purified $[(bpy)_2Ru(dpp)](PF_6)_2$ (0.30 g, 0.32 mmol), and $RhCl_3•xH_2O$ (0.045 g, 0.18 mmol) to a solution of 60 mL of 3:2 ethanol:water. A metals analysis is needed for an accurate determination of the Rh content for each sample of $RhCl_3•xH_2O$

as the degree of hydration can vary. Theoretically for a sample with exactly three waters bound to rhodium the percent mass attributed to rhodium is 39.09%. Metals analysis for the above example was determined to be 38.87%. Following addition of the reactants, the solution was heated at reflux temperature for one hour and then allowed to cool to room temperature. The crude product was precipitated in 150 mL of an approximately 50% saturated aqueous KPF_6 solution with stirring, and then isolated by vacuum filtration. The product was dried by washing with diethylether followed by air drying.

4. Purification of $[\{(bpy)_2Ru(dpp)\}_2RhCl_2](PF_6)_5$

Multiple purification methods have been applied to the trimetallic complex $[\{(bpy)_2Ru(dpp)\}_2RhCl_2](PF_6)_5$. Initial chromatographic methods, both adsorption and size exclusion chromatography, were ineffective as a result of product decomposition. Metathesis of $[\{(bpy)_2Ru(dpp)\}_2RhCl_2](PF_6)_5$ (rxn11) to the chloride salt

$$[\{(bpy)_2Ru(dpp)\}_2RhCl_2](PF_6)_5 + Bu_4NCl\ (excess) \rightarrow [\{(bpy)_2Ru(dpp)\}_2RhCl_2]Cl_5 \qquad (rxn11)$$

using an excess of Bu_4NCl in a minimum volume of acetone and the subsequent metathesis back to the PF_6^- salt (rxn12) using an aqueous KPF_6 or NH_4PF_6 solution was

$$[\{(bpy)_2Ru(dpp)\}_2RhCl_2]Cl_5 + KPF_6(excess) \rightarrow [\{(bpy)_2Ru(dpp)\}_2RhCl_2](PF_6)_5 \qquad (rxn12)$$

somewhat effective for removing the monometallic, $[(bpy)_2Ru(dpp)]^{2+}$, and other impurities, however, yields were, often as low as 50%. Recrystallization of the product from hot ethanol, 100 mg of product in 400 mL ethanol, was found to be effective for purification of the trimetallic complex, however, yields were also poor, ranging from

30% to 80%, with the lowest yields resulting in the highest purity product. Crude and purified products were analyzed by electronic absorption spectroscopy, emission spectroscopy and electrochemical methods, for determination of product purity.

5. *Purity Analysis of $[\{(bpy)_2Ru(dpp)\}_2RhCl_2](PF_6)_5$*

The trimetallic complex $[\{(bpy)_2Ru(dpp)\}_2RhCl_2](PF_6)_5$ was analyzed by electronic absorption spectroscopy, emission spectroscopy, cyclic voltammetry, and squarewave voltammetry before and after purification methods to ascertain their effectiveness. The large number of stereoisomers makes the accurate identification of the product difficult and essentially eliminates the use of NMR. The trimetallic complex has been previously synthesized, purified and isolated,[39] however, many of the studies presented here require greater purity.

Figure 19 displays the electronic absorption spectrum for an unpurified sample (blue) and a sample that has been recrystallized (black). Prior to purification, λ_{max}^{abs} for

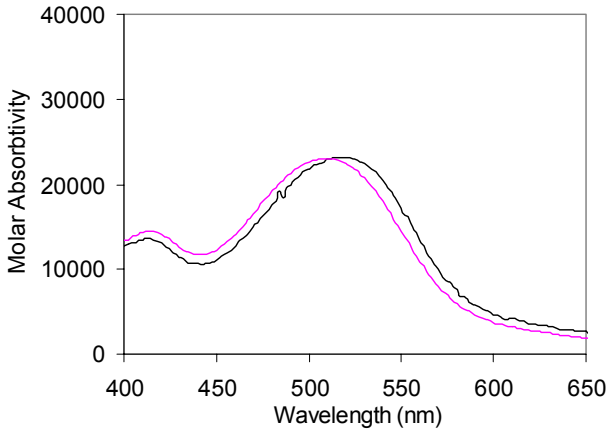

Figure 19. Electronic absorption spectrum for the complex $[\{(bpy)_2Ru(dpp)\}_2RhCl_2](PF_6)_5$ (bpy = 2,2'-bipyridine; dpp = 2,3-bis(2-pyridyl)pyrazine) both crude (blue) and after purification by recrystallization (black). A Ru → dpp CT λ_{max} shift from 510 to 518 nm is observed.

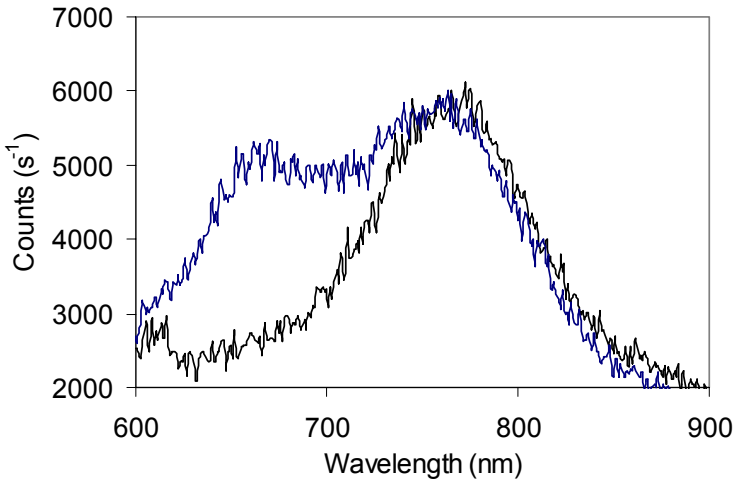

Figure 20. Emission spectroscopy for the complex $[\{(bpy)_2Ru(dpp)\}_2RhCl_2](PF_6)_5$ (bpy = 2,2'-bipyridine; dpp = 2,3-bis(2-pyridyl)pyrazine) excited at 520 nm both before (blue) and after (black) purification by recrystallization.

Ru → dpp CT band, typically appears in the range of 510 nm to 516 nm. After recrystallization there is a small red shift in the λ_{max} for the Ru → dpp CT band to 518 nm. Data from electrochemical and spectroscopic techniques coupled together indicates the impurity has a blue shifted λ_{max} for the Ru → dpp CT relative to the trimetallic product. It has been observed that with increasing amounts of impurity blue shifts are increased.

Figure 20 displays the emission spectra for the complex $[\{(bpy)_2Ru(dpp)\}_2RhCl_2](PF_6)_5$ before and after recrystallization. The peak with λ_{max} = 650 nm is attributed to the monometallic precursor $[(bpy)_2Ru(dpp)](PF_6)_2$. After recrystallization the monometallic precursor is removed to a high degree such that this impurity, with a quantum yield of emission, Φ^{em}, of 0.05,[14] which is more than two orders of magnitude greater than the trimetallic complex, $[\{(bpy)_2Ru(dpp)\}_2RhCl_2](PF_6)_5$ ($\Phi^{em} = 7.3 \times 10^{-5}$), is not observed when exciting at 520 nm. This results in a trimetallic

complexes of >99.9% purity with respect to the emissive impurity $[(bpy)_2Ru(dpp)](PF_6)_2$. This degree of purity is necessary for an in depth analysis of photophysical properties.

Figure 21 displays both cyclic and squarewave voltammetry for the complex $[\{(bpy)_2Ru(dpp)\}_2RhCl_2](PF_6)_5$ before (A) and after (B) recrystallization. These electrochemical techniques can be used to determine the degree of purity of the trimetallic complex with respect to electroactive impurities. Squarewave and cyclic voltammetry for a number of samples of trimetallic complex showed variations in the integrated peak areas for the first and second $dpp^{0/-}$ reductions which are expected to exhibit a 1 : 1 ratio. The integrated peak areas for the first and second $dpp^{0/-}$ reductions were found to be 1.0 : 0.8, which could be explained by the presence of an electroactive impurity with many of the same electrochemical characteristics, however, lacking a second $dpp^{0/-}$ reduction. The bimetallic complex, $[(bpy)_2Ru(dpp)RhCl_{2-n}X_{2+n}]^{3+n}$, although an unlikely impurity, fits some but not all of the electrochemical characteristics of the electroactive impurity. The trimetallic and bimetallic complexes should have a similar electronic environment around the ruthenium metal center so it is reasonable to assume the $Ru^{II/III}$ oxidation could overlap. The trimetallic complex has two $dpp^{0/-}$ reductions, at -0.76 and -1.00 V, whereas the bimetallic complex would have only one $dpp^{0/-}$ couple, which would also fit the electrochemical data. The monochelated rhodium, however, would be expected to have a different electronic environment than the trimetallic, which should result in a shifted $Rh^{III/II/I}$ couple, which is not observed. Following recrystallization, the peak area ratio for the first and second $dpp^{0/-}$ reductions is approximately 1.0 : 1.0, Figure 20B, indicating the trimetallic complex is pure, >95%, with respect to electroactive impurities and the electrochemical detection limit.

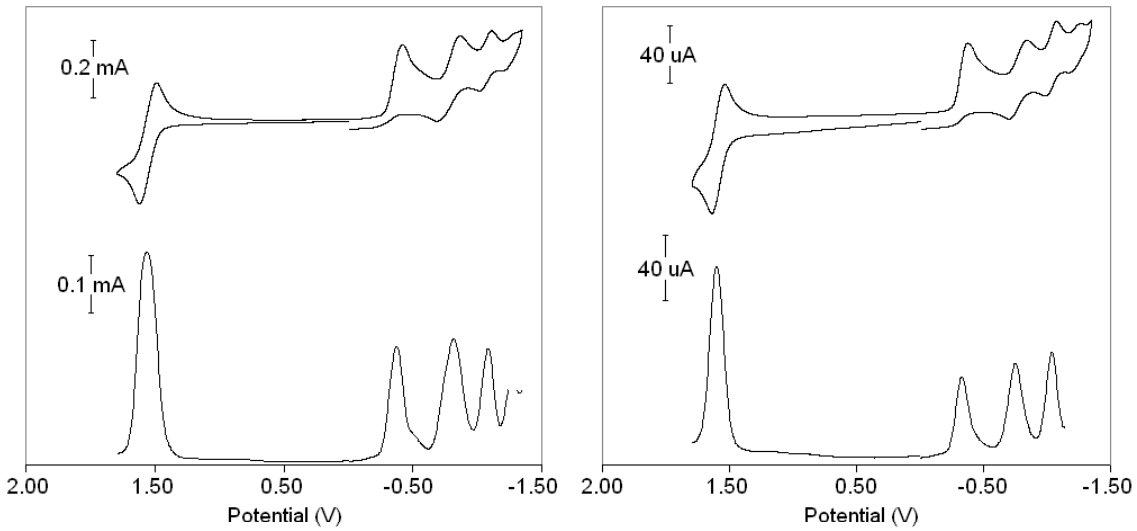

Figure 21. Cyclic and squarewave voltammetry of the complex $[\{(bpy)_2Ru(dpp)\}_2RhCl_2](PF_6)_5$ (bpy = 2,2'-bipyridine; dpp = 2,3-bis(2-pyridyl)pyrazine) both A) before and B) after purification by recrystallization plotting potential, V, versus current, A.

Electronic absorption spectroscopy, emission spectroscopy, and cyclic and squarewave voltammetry in conjunction are necessary for evaluation of product purity. Electronic absorption spectroscopy and the electrochemical methods employed are not sensitive enough to detect the very low levels of monometallic precursor $[(bpy)_2Ru(dpp)](PF_6)_2$ that are necessary for photophysical studies. Emission spectroscopy, however, can detect this level of impurity. With the similarities between the bimetallic and trimetallic complexes, many of the electrochemical and spectroscopic properties are similar or the same, however, electronic absorption spectroscopy and cyclic and squarewave voltammetry can be used as a handle for determination of purity with respect to the bimetallic complex. For a detailed discussion on spectroscopic and electrochemical properties for the trimetallic complex $[\{(bpy)_2Ru(dpp)\}_2RhCl_2](PF_6)_5$ see section V. Results and Discussion.

IV. Experimental Methods

A. Electrochemistry

Cyclic and squarewave voltammograms were recorded using a one-compartment, three electrode cell, with a Bioanalytical Systems (BAS) potentiostat, using a platinum wire auxiliary electrode, and a 1.9 mm diameter glassy carbon disk working electrode also purchased from BAS. Bulk electrolysis experiments were conducted in an H-cell, a two compartment cell separated by a porous glass frit designed to allow current flow but inhibit the flow of analyte. Mixing of the auxiliary and working electrode compartments can result in incomplete electrolysis. For bulk electrolysis, large surface area working and auxiliary electrodes are necessary for complete bulk conversion of the analyte. Platinum mesh working and auxiliary electrodes were utilized as shown in Figure 22 for bulk electrolysis. All potentials were measured versus a Ag/AgCl electrode (0.29 V vs NHE), calibrated using the ferrocene couple, $FeCp_2/FeCp_2^+$ (0.67 V vs NHE).[60] All measurements were carried out in solutions of Burdick and Jackson UV-grade

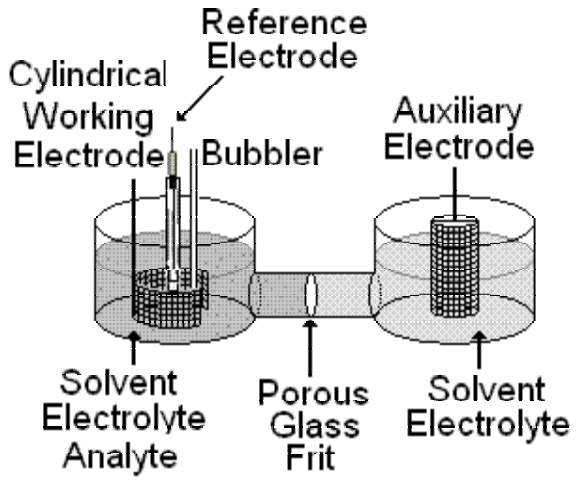

Figure 22. H-cell for bulk electrolysis showing the working and auxiliary electrodes, reference electrode, bubbler, porous glass frit, solvent, electrolyte, and analyte.

acetonitrile, deoxygenated and blanketed with argon. Bu_4NPF_6 (0.1 M) was used as the supporting electrolyte, which was purified by recrystallized from hot ethanol. Purity was determined by cyclic voltammetry.

B. Electronic Absorption Spectroscopy

Electronic absorption spectra were recorded using a Hewlett-Packard 8452A diode array spectrophotometer with 2 nm resolution. All solutions were prepared using Burdick and Jackson UV grade acetonitrile and all measurements were made at room temperature. The concentration of analyte was determined spectroscopically using Beer's Law. Optical quality glass or Spectrosil quartz cuvettes with a 1 cm path length purchased from Starna were used to measure the electronic absorption spectra.

C. Spectroelectrochemistry

Spectroelectrochemical measurements were made using a Hewlett-Packard 8452A diode array spectrophotometer with a 2 nm resolution to record the electronic absorption spectra and a BAS CV-27 potentiostat purchased from BAS to electrolyze the bulk solution at the desired potential. An H-cell of local design was used, Figure 23, with the working compartment consisting of a 1 cm rectangular cell constructed with two polished optical quality glass walls to allow for spectroscopic measurements. A platinum mesh working electrode and a carbon cloth auxiliary electrode were used in separate compartments to allow for complete electrolysis. The electrolysis potential was set using a Ag/AgCl reference electrode (0.29 V vs NHE), calibrated using $FeCp_2/FeCp_2^+$ (0.67 V vs NHE).[60] Solutions were prepared gravimetrically in Burdick and Jackson UV grade

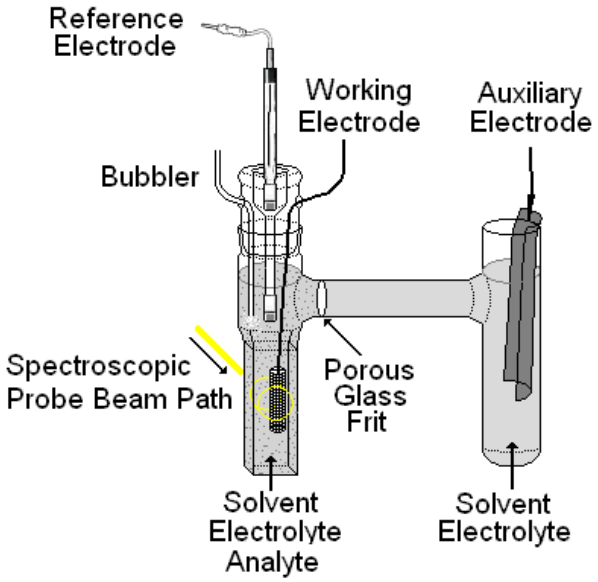

Figure 23. H-cell for spectroelectrochemistry showing the working compartment with an optical quality 1 cm path length cell containing the working electrode which is lifted during spectroscopic measurements, the reference electrode, a bubbler, solvent, electrolyte and the analyte. The auxiliary compartment, separated from the working compartment by a porous glass frit, contains the auxiliary electrode, solvent, and electrolyte.

acetonitrile with 0.1 M Bu_4NPF_6 as the supporting electrolyte. Solution were deoxygenated by bubbling argon for the duration of the electrolysis and blanketed with argon while recording the electronic absorption spectrum.

D. Emission Spectroscopy

Emission spectra were recorded using a modified Quanta-Master Model QM-200-45E fluorimeter from Photon Technology, Inc. The system was designed to use a water cooled 150 W xenon lamp as the excitation source. Uncorrected emission data was collected at a right angle by a thermoelectrically cooled Hamamatsu 1527 photomultiplier tube operating in photon counting mode. The monochrometers used resulted in a maximum resolution of 0.25 nm. A correction file for the PMT is shown in Figure 24

displaying the response versus wavelength. Spectrosil quartz cuvettes with four polished sides, a screw top fitted with a septum cap and with a 1 cm path length, which were purchased from Starna, were used for all emission experiments. All solutions were prepared in Burdick and Jackson UV grade acetonitrile and deoxygenated by bubbling argon for 10 minutes. For quantum yield measurements, solutions were absorbance matched to the reference complex $[Os(bpy)_3](PF_6)_2$ (Φ^{em} = 0.000462; λ_{max}^{em} = 746 nm; in CH_3CN)[61] prepared by the method reported by Meyer.[62]

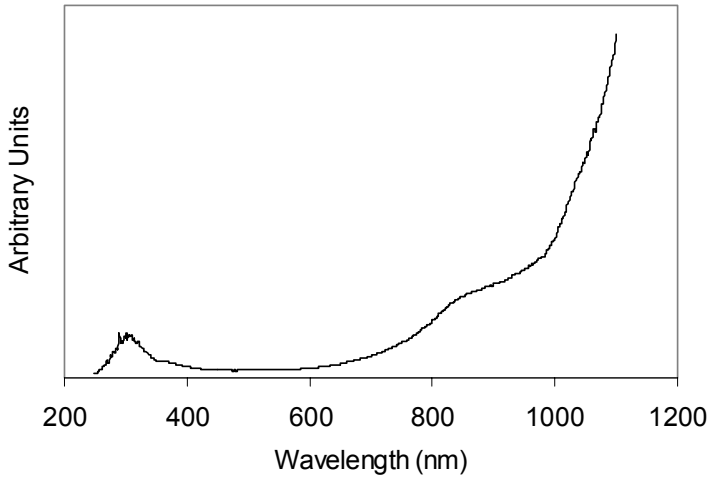

Figure 24. Correction file for the Hamamatsu 1527 photomultiplier tube plotting the inverse of the PMT response versus wavelength.

E. Excited State Emission Lifetime Measurements

Excited state emission lifetime measurements were made using Photon Technologies Inc. (PTI) PL 2300 Nitrogen Laser pumping a PTI PL 201 continuously tunable dye laser as an excitation source (360 - 900 nm). This excitation source has an energy output of 240 μJ per pulse and a pulse width of 500 ps. A Coumarin 500 laser dye ($1x10^{-3}$ M in ethanol), purchased from PTI, was used for excitation wavelengths between 470 and 550 nm or a Stillbene 420 laser dye ($1x10^{-3}$ M in ethanol), purchased

from Exciton, Inc., for excitation wavelengths between 420 and 469 nm. The laser dye system used for excited state emission lifetime measurements, shown in Figure 25, operates with a nanosecond time scale resolution. Signals for all measurements were recorded and digitized using a LeCroy 9361 dual 300 MHz Oscilloscope (operating at 2.5 Gs/s) and averaged over 200 laser pulses. The decay profile is displayed on the digital oscilloscope which was saved and converted to a text file. Data was processed in Microsoft Excel. The natural log of the decay profile is plotted from which the reciprocal of the slope is the excited state lifetime, τ (eq9).

$$\ln(|\text{decay}|) = 1/\tau \qquad \text{(eq9)}$$

Spectrosil quartz cuvettes with a septum screw top purchased from Starna were used for all excited state lifetime experiments. Solutions were prepared in Burdick and Jackson UV grade acetonitrile and deoxygenated by bubbling argon for 10 min.

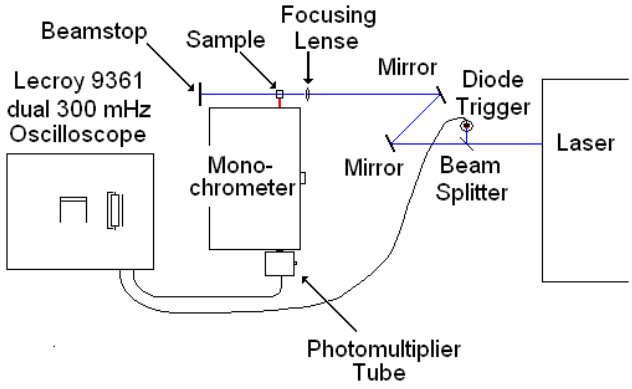

Figure 25. Schematic for emission lifetime measurements using a PTI PL 2300 nitrogen laser with a PL 201 dye chamber showing the excitation source, the beam path, beam stop, trigger, sample, emission monochrometer, photomultiplier tube and oscilloscope.

F. Photolysis with 1000 W Xenon Arc Lamp

A 1000 W xenon arc lamp purchased from Oriel was used for continuous photolysis experiments. The system includes a water filter to remove radiation from the

UV and IR regions of the spectrum. Additional components used in the photolysis setup include a 10 nm band pass filter centered at 520 nm (+/- 5 nm at half peak height) also purchased from Oriel and a focusing lens to focus the 2 inch collimated light down to the photolysis cell. The photolysis cell used was cylindrical with a 1 cm path length and a volume of approximately 3.1 mL and a cylindrical top compatible with a rubber septum. The 1 cm cylindrical cell was purchased from Starna. The photolysis setup using the 1000 W Xenon arc lamp is shown in Figure 26. The sample cell was cooled using a water cooled cell holder of local design connected to a Brinkman RM6 thermostated water supply. All solutions were prepared using Burdick and Jackson UV grade acetonitrile and deoxygenated by bubbling argon. Metal complex concentration was determined spectroscopically using Beer's Law. Other preparatory conditions were

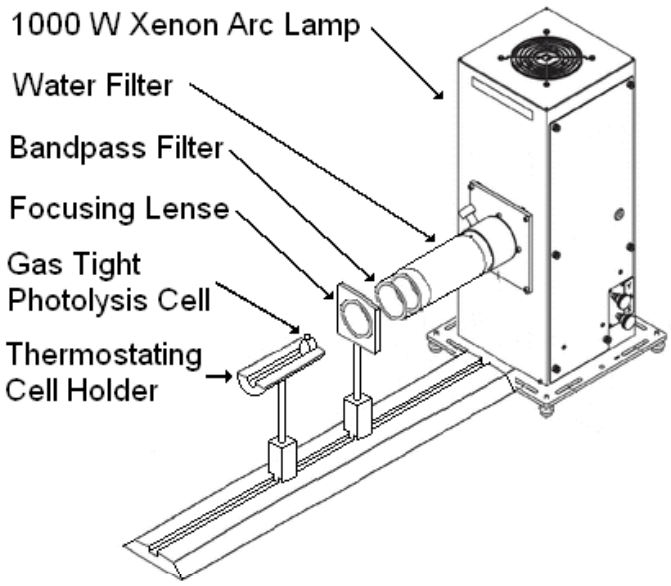

Figure 26. 1000 W xenon arc lamp and photolysis experimental design including H_2O UV and IR filter, a band pass narrow band pass filter to select the photolysis wavelength, a focusing lens to focus the collimated light onto the cell and the gas tight photolysis cell placed on a thermostated cell holder.

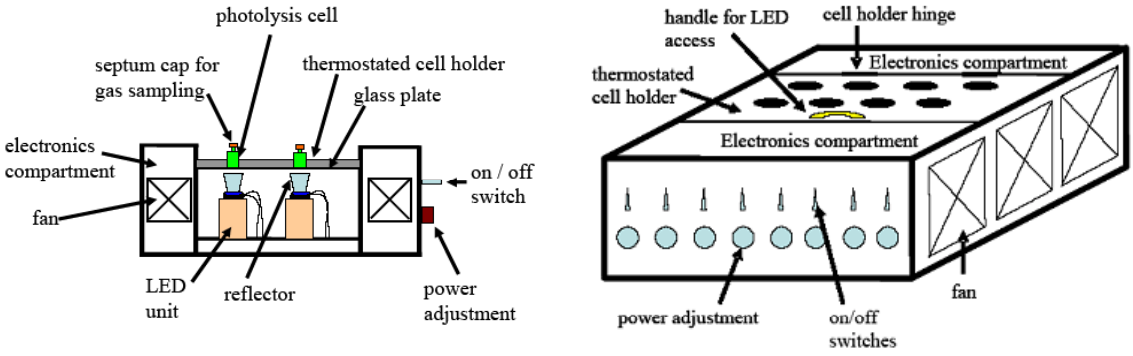

Figure 27. A) Cross section of the LED array used for photolysis showing the modular LED units. B) LED array illustration showing the overall design and layout.[63]

predicated by the experimental design such as the concentration of sacrificial donor, i.e. dimethylaniline (DMA).

G. Photolysis with LED Array

A photolysis array was designed and constructed locally using LEDs as light sources, Figure 27B. The LED array, designed by Brown and Brewer, has several features that help make it a consistent and reproducible light source.[63] The array is also modular, allowing for the use of LEDs with varying wavelengths, shown in Figure 26A. One of the primary design features to enable each LED to deliver the same light flux to each sample is the tunability of the power supplied to each LED. An abbreviated circuit diagram is shown in Figure 28. The circled area shows an adjustable rheostat. This part of the circuit acts as a dimmer allowing the operator to control the power supplied to each LED and thus the light flux from each LED. For additional details on the LED array used for hydrogen photocatalysis experiments including materials and construction, a detailed description is provided in The Proceedings of the SPIE.[63]

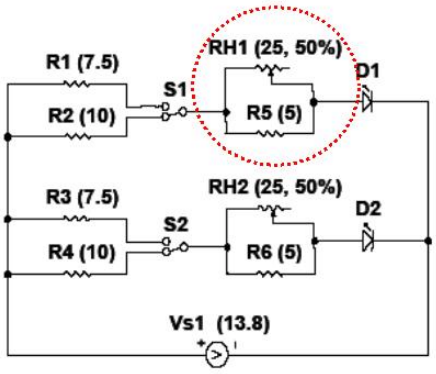

Figure 28. An abbreviated circuit diagram for the LED array showing the circuitry for two LEDs. The circled portion is an adjustable rheostat in parallel with a 5 ohm resister. This part of the circuit acts as a dimmer and allows for fine tuning of the power supplied to each LED thus making the light flux for each LED adjustable.[63]

H. Actinometry

Light output from the 1000 W xenon arc lamp and the LED array was quantified by chemical actinometry. The chemical actinometers ferrioxalate (rxn13, rxn14) and Reinecke's Salt (rxn15, rxn16) were used to determine the light flux. Calorimetry, which measures radiant energy, was used to determine the relative light flux for each LED within the array once the absolute light flux had been determined.

Ferrioxalate is the most commonly employed solution actinometer typically used in the wavelength range of 250 to 500 nm. This actinometer has a quantum yield that varies little between 240 and 500 nm (0.0125 to 0.009), is stable, and behaves well.[64] The ferrioxalate actinometer involves the photodissociation of oxalate anions (rxn13) followed by the complexation of phenanthroline ligands (rxn14) to form $[Fe^{II}(phen)_3]^{2+}$ which is measured spectroscopically to determine the quanta per unit time.

$$[Fe^{III}(C_2O_4)_3]^{-3} \rightarrow [Fe^{II}(C_2O_4)_2]^{-2} + 2\ CO_2 \qquad \text{(rxn13)}$$

$$phen + [Fe^{II}(C_2O_4)_2]^{-2} \rightarrow [Fe^{II}(phen)_3]^{2+} \qquad \text{(rxn14)}$$

Typically a solution of 0.15 M $K_3[Fe(C_2O_4)_3]$ is used for wavelengths greater than 405 nm, with 10 % of the solution composed of 1 N H_2SO_4. The path length can be adjusted to provide ~100 % absorption. For wavelengths longer than 500 nm there is a significant drop in quantum yield making ferrioxalate a poor actinometer for longer wavelengths.

Reinecke's Salt solution, $[Cr^{III}(NH_3)_2(NCS)_4]^-$, was used as an actinometer for wavelengths longer than 500 nm. Reinecke's Salt requires more attention to detail as thiocyanate, which complexes with Fe to form the spectroscopically measurable product, can also be generated thermally. In addition, multiple equivalents of thiocyanate can be generated photochemically under basic conditions making the accurate determination of light flux more difficult. It is essential to use this chemical actinometer under acidic conditions so only one thiocyanate will photodissociate. A blank should also be measured for the same time period as the light flux measurement in order to account for any thermally generated thiocyanate. Reinecke's Salt involves the photodissociation of thiocyanate and the aquation of the chromium(III) complex (rxn15). Iron(II) then complexes with thiocyanate to form the spectroscopically measurable iron complex (rxn16).

$$[Cr^{III}(NH_3)_2(NCS)_4]^- + H_2O \rightarrow [Cr^{II}(NH_3)_2(NCS)_3(H_2O)]^- + NCS^- \quad \text{(rxn15)}$$

$$Fe^{II} + NCS^- \rightarrow [Fe^{II}(H_2O)_5(NCS)]^+ \quad \text{(rxn16)}$$

Light flux determination for the xenon arc lamp with a 520 nm narrowband pass filter involved the use of Reinecke's Salt. An aqueous solution of 0.0040 M $[Cr^{III}(NH_3)_2(NCS)_4]^-$ was prepared spectroscopically and a developing solution consisting of 0.5 M perchloric acid and 0.1 M $[Fe(NO_3)_3(H_2O)]$ was prepared volumetrically (acid) and gravimetrically (iron complex). The Reinecke's Salt solution was determined to

have an absorbance of 2.020 in a 5 cm cylindrical cell, Figure 29. The actinometer was photolyzed at 520 nm for a period of 5 minutes. 2 mL of the photolyzed solution was then added to 8 mL of the developing solution and measured spectroscopically. A control solution was also prepared consisting of an unphotolyzed Reinecke's Salt solution (2 mL) of which were added to 8 mL of developing solution and measured spectroscopically. All solutions were developed for 5 min. In total three photolysis trials were measured with corresponding controls to account for any thermally liberated thiocyanate, Figure 30. All trials were conducted in a dark room to limit any photodissociation not a result of the light source to be quantified. The average incident radiation, I_o, can be calculated using equation 10.[64]

$$I_o = (6.023 \times 10^{20} V_1 V_3 \Delta A) / (\Phi t(1-10^{-\varepsilon_1 [a] l_1}) V_2 l_2 \varepsilon_2) \qquad \text{(eq10)}$$

V_1 is the volume of the actinometer solution irradiated (typically 13 to 14 mL), V_2 is the volume of the irradiated solution that is developed (2 mL), V_3 is the final volume after dilution with the developing solution (10 mL). ΔA is the difference in absorbance between the photolyzed solution and the control solution. Φ is the quantum yield for

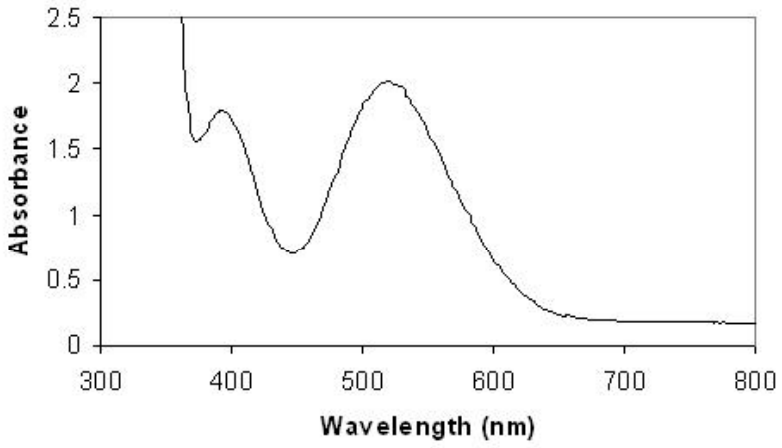

Figure 29. Electronic absorption spectrum for a sample of 0.004 M Reinecke's Salt in a 5 cm cylindrical cell before photolysis.

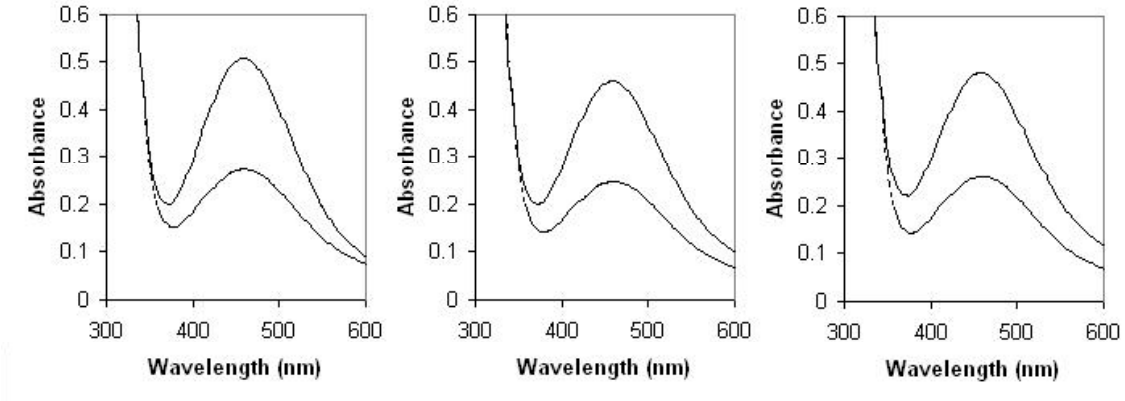

Figure 30. Electronic absorption spectroscopy for three actinometry trials with Reinecke's Salt. The spectrum displays the photolyzed and unphotolyzed Reinecke's Salt solutions after being developed in 0.5 M perchloric acid and 0.1 M $[Fe(NO_3)_3(aq)]$. In each spectrum the stronger absorbing species is the photolyzed sample while the lower absorbing species is the unphotolyzed control.

formation of the photoproduct at the measured wavelength, in this case 520 nm, which is 0.286 at 23°C. For a complete list of Φ see the Chemists Companion.[64] The fraction of the light absorbed, $1\text{-}10^{-\varepsilon_1[a]l_1}$, which is also 1 - % transmittance, where l_1 is the path length of the cell used for irradiation (5 cm), l_2 is the path length of the cell used for measuring the absorbance of the developed solution (1 cm), ε_1 is the molar extinction coefficient of the Reinecke's Salt solution at the wavelength measured (106.5 $M^{-1}cm^{-1}$) and ε_2 is the molar extinction coefficient of the developed solution consisting of $[Fe^{II}(H_2O)_5(NCS)]^+$ (4.30 x 10^3 $M^{-1}cm^{-1}$). The three trials yielded an average I_o of 6.34 x 10^{18} photons min^{-1}.

I. Catalytic Hydrogen Generation

Hydrogen catalysis experiments were carried out initially using an Oriel 1000W xenon arc lamp using the same setup as described in section VII. F. Subsequently a

photolysis array was designed and constructed using LEDs as light sources as detailed in section VII. G. Samples were prepared using Burdick and Jackson UV grade acetonitrile, deionized water adjusted to a pH of 2.0 using triflic acid, and the sacrificial electron donor, DMA. Conditions were varied based on the individual experiment and are detailed in section VIII. Hydrogen was detected and quantified by gas chromatography, described in the section VII. J.

J. Gas Chromatography

A GOW-MAC series 580 gas chromatograph equipped with 5A molecular sieves columns (1/8 in. x 6 ft.), purchased from Alltech, and a thermal conductivity detector was used for detection and quantization of gasses. The detector consisted of rhenium-tungsten filaments purchased from GOW-MAC Instrument Company. Argon was used as the carrier gas as opposed to nitrogen, which is most commonly employed, because there is a larger difference in thermal conductivity between an argon carrier gas and the analyte (hydrogen). The thermal conductivities of argon, nitrogen, and hydrogen at 300 K are 17.9, 26.0, and 186.9, respectively.[64] Ultra high purity Argon (>99.999%), purchased from Airgas, was used to limit oxidation and extend the lifetime of the rhenium-tungsten detector filaments. Gaseous samples of the headspace for hydrogen catalysis experiments were injected into the GC using 1700 series gas tight syringes with samplelock purchased from Hamilton Company. 5A molecular sieves columns have been shown to be capable of separating hydrogen, nitrogen and oxygen, Figure 31, the three primary gasses present in the hydrogen photocatalysis experiments discussed in section VIII. I.

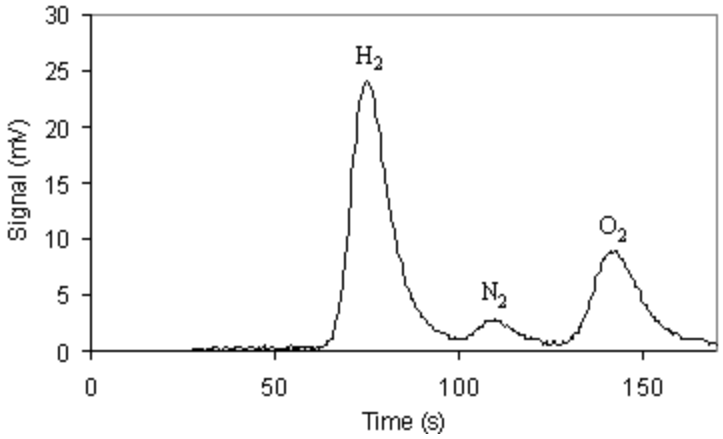

Figure 31. Gas chromatogram showing the separatory performance of the 5A molecular sieves column using Ar carrier gas for the separation of hydrogen, nitrogen and oxygen. Hydrogen elutes first followed by nitrogen and then oxygen.

Calibration curves were employed to quantitatively determine analyte concentrations. A sample calibration curve for hydrogen quantization is shown below in Figure 31. This calibration curve was produced using 4 trials. Each trial consisted of degassing with argon a 25 mL flask equipped with a septum for 10 min followed by hydrogen injections using a 1700 series 5 mL gas tight syringe with sample lock purchased from Hamilton Co. to make a 20% by volume hydrogen mixture (80% Argon). From this flask 5 injections were made into the GC using a 100 uL syringe (also a 1700 series gas tight syringe with sample lock purchased from Hamilton Co) consisting of 20 uL, 40 uL, 60 uL, 80 uL and 100 uL of the gaseous mixture. These injections correspond to 4, 8, 12, 16, and 20 uL of hydrogen. All signal responses from the GC were recorded using Logger Pro version 3.4.5 and plotted on a 0.5 second time resolution. Data was exported as text files and analyzed with Microsoft Excel. All pseudo integrations were made with the same time resolution as the calibration curve. Figure 32 shows the results of a H_2 calibration plot. Subsequent H_2 measurements using the same GC parameters (attenuation, temperature, detector current, etc.), same filament, and same recorder setting

were quantitated using the appropriate calibration. The peak area for a hydrogen analyte injection is pseudo integrated using the same method as the calibration and then divided by the slope (peak area / uL H_2) of the calibration curve to determine the amount of H_2 in the injection.

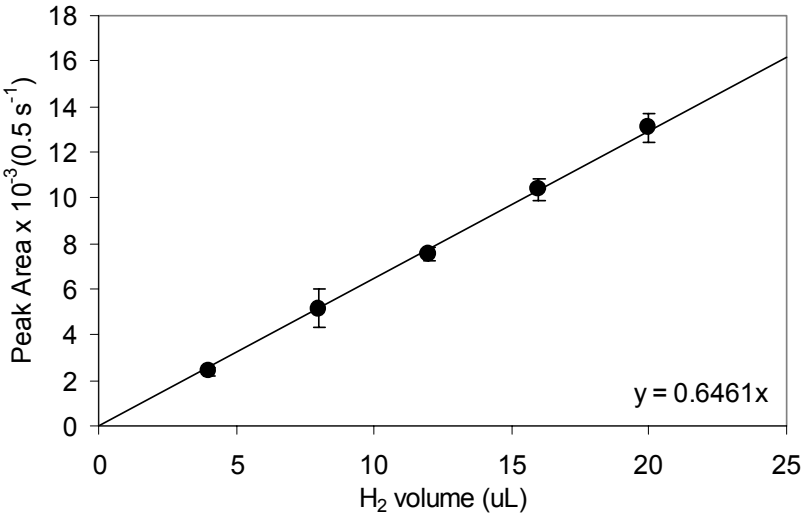

Figure 32. GC calibration for hydrogen quantization using 20, 40, 60, 80, and 100 uL injections of a 20% hydrogen mixture with argon by volume corresponding to 4, 8, 12, 16, and 20 uL hydrogen.

V. Results and Discussion

A. Photochemical Molecular Device for Light to Energy Conversion

The visible region of the solar spectrum contains most of the incident radiation that reaches the earth's surface. Any light energy to chemical energy conversion scheme devised must be capable of efficiently harnessing the available light, i.e. the visible region of the solar spectrum. Photons from the visible region of the solar spectrum are of sufficient energy to drive water splitting, however, water is transparent in the visible, necessitating the use of a catalyst to harness this energy. The single electron water splitting reaction requires a 5 eV driving force (rxn 19). A single electron light to

$$H^+ + e^- \rightleftharpoons H^\bullet \qquad \text{(rxn17)}$$

$$H_2O \rightleftharpoons e^- + H^+ + OH^\bullet \qquad \text{(rxn18)}$$

$$H_2O \rightleftharpoons H^\bullet + OH^\bullet \qquad \text{(rxn19)}$$

energy conversion scheme would therefore be limited to the high energy region of the spectrum whereas a multielectron water splitting scheme can proceed with a lower driving force, 1.23 eV, (rxn 22) enabling the possibility of a visible light driven process, Figure 33.

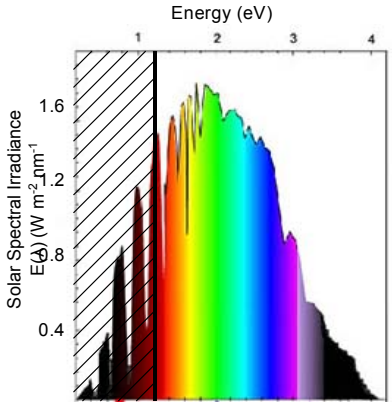

Figure 33. Solar spectrum displaying the incident radiation per electron volt indicating the region of sufficient energy for the multielectron splitting of water, 1.23 eV.

$$2H^+ + 2e^- \rightleftharpoons H_2 \quad \text{(rxn20)}$$

$$H_2O \rightleftharpoons 2e^- + 2H^+ + O_2 \quad \text{(rxn21)}$$

$$H_2O \rightleftharpoons H_2 + \tfrac{1}{2}O_2 \quad \text{(rxn22)}$$

Water is transparent in the visible and near UV regions of the spectrum so a catalyst must be employed to absorb the photons of the required energy. A catalyst is also needed to assist in the bond making/breaking process. A photochemical molecular device can be designed to meet these requirements. One approach is to create a photochemical molecular device using a supramolecular architecture.

B. Supramolecular Architecture for Photoinitiated Electron Collection

Balzani describes a supramolecular complex in a benchmark monograph on photochemical molecular devices.[36] In this context, a supramolecular complex is a large molecule made up of several components. Balzani describes each part as doing a specific task and when combined with sub-units performing other tasks this leads to a device that can perform complex functions. One component commonly employed in supramolecular assemblies is a light absorber. When a light absorbing unit is incorporated the complex is often referred to as a photoinitiated molecular device. Other components often utilized in photoinitiated molecular devices include connectors (bridging ligands), electron donors, electron acceptors, and electron collectors.

A supramolecular assembly can be designed to couple light absorbing units, electron donors, and electron acceptors to create photochemical molecular devices for photoinitiated charge separation, Figure 34. Multiple light induced charge transfers to a stable electron acceptor, or electron collector, can lead to photoinitiated electron

collection. The stored electrons can then be employed in catalysis like the photocatalytic splitting of water.

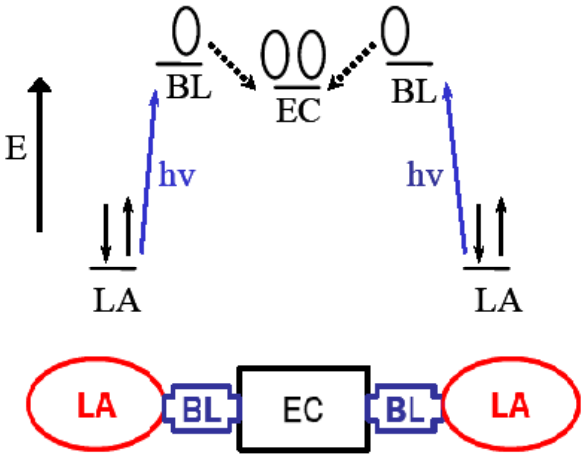

Figure 34. Molecular orbital diagram for a supramolecular complex of the form LA-BL-EC-BL-LA designed to photochemically collect electrons at the central EC.

C. Electrochemical Properties

Cyclic voltammetry was employed to study the trimetallic complex $[\{(bpy)_2Ru(dpp)\}_2RhCl_2](PF_6)_5$ and to evaluate the purity of its precursors. Cyclic voltammetry, now the most commonly used electrochemical technique among non electrochemists, has several advantages as compared to other electrochemical techniques. Linear sweep methods like cyclic voltammetry utilize a simple waveform that is presently available on most commercial potentiostats that ramps the applied potential linearly with time while measuring the current over time. Information about peak reversibility can be obtained using cyclic voltammetry an important aspect in the study of multimetallic systems. The cyclic voltammogram of the complex $[\{(bpy)_2Ru(dpp)\}_2RhCl_2](PF_6)_5$ is

shown in Figure 35. Anodic peak potentials, E_p^a, and cathodic peak potentials, E_p^c, for the redox potentials are given in Table 2. The peak to peak separation, ΔE_p ($\Delta E_p = E_p^c - E_p^a$), is independent of scan rate but dependent on temperature, equation 11, with ΔE_p (at 25° C) = 59/*n* mV (*n* = number of electrons transferred in the redox reaction) for a reversible redox couple.[65]

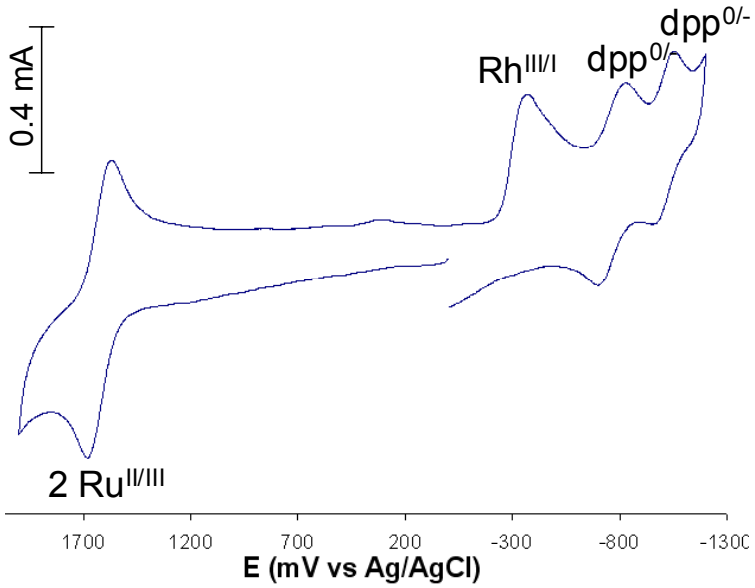

Figure 35. Cyclic voltammogram for the complex $[\{(bpy)_2Ru(dpp)\}_2RhCl_2](PF_6)_5$ (bpy = 2,2'-bipyridine; dpp = 2,3-bis(2-pyridyl)pyrazine) displaying a two electron $Ru^{II/III}$ couple corresponding to the near simultaneous oxidation of the two Ru centered light absorbers in the oxidative region. The reductive region displays an irreversible two electron $Rh^{III/II/I}$ reduction followed by two reversible one electron dpp reductions.

Table 2. Anodic, cathodic, and half wave peak potentials for the redox processes for the complex $[\{(bpy)_2Ru(dpp)\}_2RhCl_2](PF_6)_5$ (bpy = 2,2'-bipyridine; dpp = 2,3-bis(2-pyridyl)pyrazine). All potentials referenced vs. Ag/AgCl.

redox couple	E_p^a	E_p^c	ΔE_p	$E_{1/2}$
$Ru^{II/III}$	1.65	1.55	0.10	1.60
$Rh^{III/II/I}$		-0.37		-0.37
$dpp^{0/0}$, $dpp^{0/-}$	-0.69	-0.83	0.14	-0.76
$dpp^{0/-}$, $dpp^{-/-}$	-0.97	-1.07	0.09	-1.02

$$\Delta E_p = \frac{2.303\ RT}{nF} \qquad \text{(eq11)}$$

n is the number of electrons, F is Faraday's constant (96,485 $C \cdot mol^{-1}$),[22] the total charge of one mole of electrons, R is the gas constant (8.314 $J \cdot K^{-1} \cdot mol^{-1}$),[22] and T is temperature in K. ΔE_p for $Ru^{II/III}$ is 100 mV. When $\Delta E_p > 59/n$ mV, as is the case for the $Ru^{II/III}$ couple $\Delta E_p > 29.5$, the electrochemical process can be considered quasireversible, however, some deviation of ΔE_p is typically observed experimentally due to solution resistance, especially at higher scan rates. Another possibility is that it is not a single $Ru^{II/III}$ couple but instead the signal is composed of two closely separated $Ru^{II/III}$ couples This, however, would still result in $\Delta E_p > 59$ mV. No return wave is observed for the $Rh^{III/II/I}$ couple indicating an irreversible process. ΔE_p for the first and second dpp reductions are 143 mV and 92 mV respectively indicating quasireversibility. Again some contribution to $\Delta E_p > 59$ mV could be due to solution resistance.

Squarewave voltammetry was also used in the initial characterization of the trimetallic complex $[\{(bpy)_2Ru(dpp)\}_2RhCl_2](PF_6)_5$. Squarewave voltammetry is a potential step method, also known as a pulsed method, that is complimentary to cyclic voltammetry. Potential step methods main advantage is the capability of discriminating between the faradaic current (analyte signal) and the capacitive current or charging current (background). This is accomplished by taking advantage of the fact that the faradaic current decays as a function of $1/t^{1/2}$ whereas the capacitive current has an exponential decay. The waveform for pulsed voltammetric techniques is made up of a series of pulses or steps of the applied potential followed by a short pause after each step where the capacitive current diminishes faster than the faradaic current, after which the current is measured. This waveform results in higher signal to noise ratio, a lower limit

of detection, and a larger accessible potential window, as a result of the decreased charging current. Potential step techniques, however, are also relatively slow due to the pause after every potential step up. Potential step techniques are also effective for measuring closely spaced couples. A squarewave voltammogram for the complex $[\{(bpy)_2Ru(dpp)\}_2RhCl_2](PF_6)_5$ is shown in Figure 36.

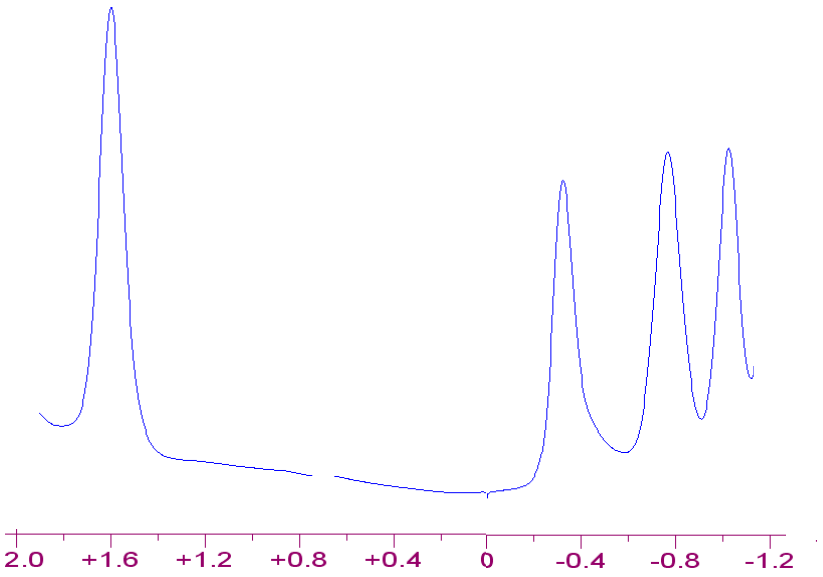

Figure 36. Squarewave voltammogram for the complex $[\{(bpy)_2Ru(dpp)\}_2RhCl_2](PF_6)_5$ (bpy = 2,2'-bipyridine; dpp = 2,3-bis(2-pyridyl)pyrazine) displaying a two electron $Ru^{II/III}$ couple in the oxidative region and a rhodium reduction followed by two dpp reductions in the reductive region.

The electrochemistry of the complex $[\{(bpy)_2Ru(dpp)\}_2RhCl_2](PF_6)_5$, shown in Figures 33 and 34, displays a reversible oxidation at 1.63 V vs Ag/AgCl, assigned to two overlapping $Ru^{II/III}$ couples.[66] The overlapping couples indicate that the two ruthenium centers are largely electronically isolated from each other. In the reductive region of the cyclic voltammogram, an irreversible $Rh^{III/II/I}$ couple at -0.37 V is observed followed by two reversible bridging ligand $dpp^{0/-}$ couples at -0.76 and -1.00 V. Since the first

oxidation is ruthenium based and the first reduction is rhodium based, the highest occupied molecular orbital has a Ru(dπ) nature and lowest unoccupied molecular orbital has a Rh(dσ*) nature.[66]

Bulk electrolysis was employed to investigate the electrochemical mechanism of the irreversible two electron rhodium reduction. The bulk electrolysis was performed on the complex $[\{(bpy)_2Ru(dpp)\}_2RhCl_2](PF_6)_5$ at –0.40 V vs. Ag/AgCl resulting in a two electron reduction to form a Rh^I centered complex, Figure 37. Rh^{III} is a d^6 metal center stable in an octahedral coordination environment, whereas Rh^I is a d^8 metal center preferring a square planar ligand geometry. Therefore the reduction of Rh^{III} to Rh^{II} to Rh^I should result in ligand loss. Upon reduction of $[\{(bpy)_2Ru(dpp)\}_2Rh^{III}Cl_2]^{5+}$ by two electrons, the complex could potentially release two chlorides to form the complex $[\{(bpy)_2Ru(dpp)\}_2Rh^I]^{5+}$ or one of the light adsorbing fragments could be lost forming the complex $[(bpy)_2Ru(dpp)Rh^ICl_2]^{3+}$.

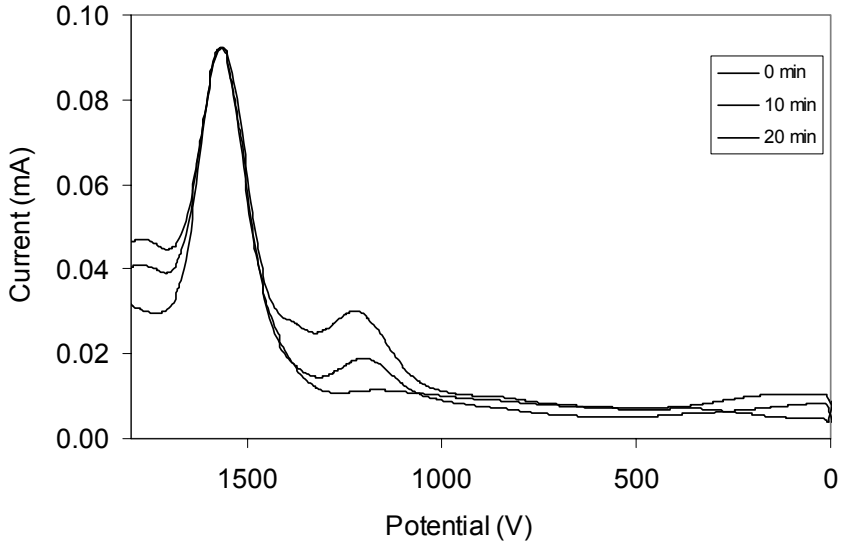

Figure 37. Squarewave voltammogram for the complex $[\{(bpy)_2Ru(dpp)\}_2RhCl_2](PF_6)_5$ (bpy = 2,2'-bipyridine; dpp = 2,3-bis(2-pyridyl)pyrazine) following bulk electrolysis showing the ruthenium oxidation and a peak growing in over time corresponding to the oxidation of free chloride.

DeArmond has studied ligand loss in octahedral Rh^{III} complexes which can serve as a model for ligand loss in the trimetallic complex $[\{(bpy)_2Ru(dpp)\}_2RhCl_2](PF_6)_5$. DeArmond uses cyclic voltammetry to probe reaction sequences for $[Rh^{III}(bpy)_3]^{3+}$ and $[Rh^{III}(bpy)_2Cl_2]^{+}$.[67] First, cyclic voltammograms were taken at two different sweep rates, 0.10 and 31 V/s, shown in Figure 38A. The slower sweep rate shows an irreversible two electron rhodium reduction followed by two one electron bpy reductions. The fast sweep rate reveals that the two electron rhodium reduction is actually two one electron reductions with little separation. Figure 38B shows the initial part of the first reduction at a very fast scan rate, 46 V/s. Reversing the potential after the initial part of the rhodium

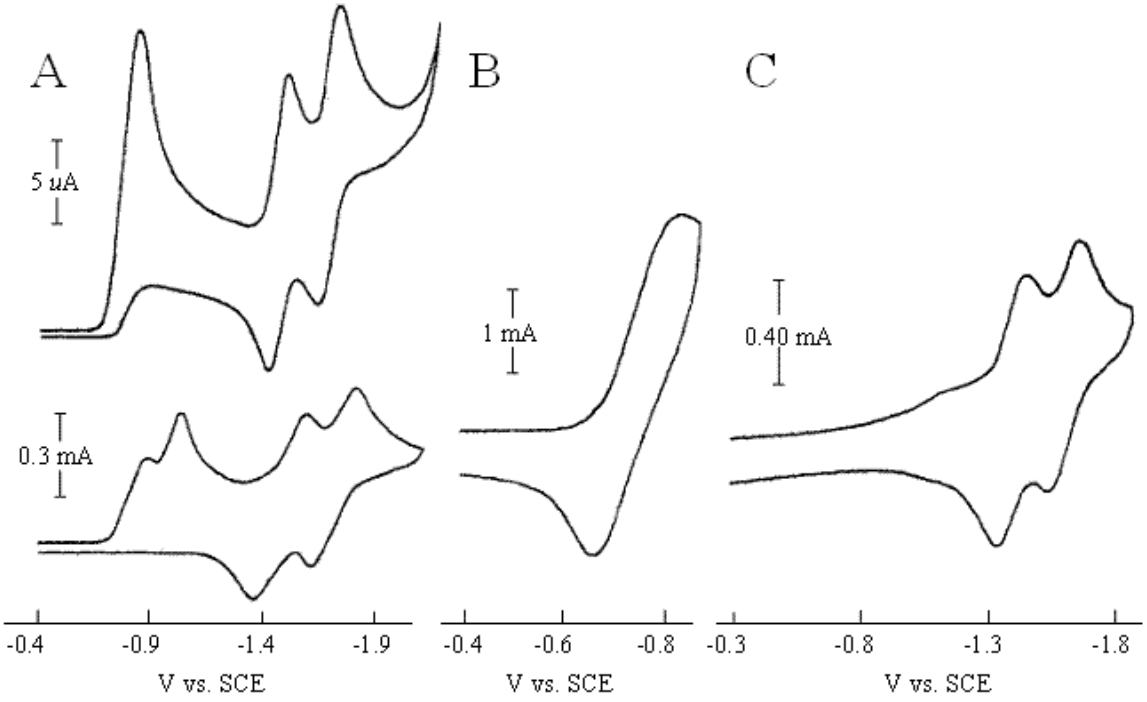

Figure 38. Cyclic voltammetry for $[Rh^{III}(bpy)_3]^{3+}$ (bpy = 2,2'-bipyridine) measured in CH_3CN with 0.1 M Et_4NClO_4 vs. SCE showing A) the reductive region at two different scan rates, 0.10 V and 31 V, B) the initial part of the first reduction at a high scan rate, 46 V, showing some reversibility , and C) reduction of the reduced complex $[Rh^{I}(bpy)]^{2+}$ showing the absence of the rhodium reduction as it is already in a reduced state, followed by two reversible $bpy^{0/-}$ reductions.[67] Reproduced with permission from Kew, G.; DeArmond, K.; Hanck, K. *J. Phys. Chem*. **1974**, *78*, 727. Copyright 2007 American Chemical Society.

reduction isolates the $Rh^{III/II}$ couple from the $Rh^{II/I}$ couple. Isolating couples can provide information about peak reversibility. At the fast 46 V/s scan rate, the first part of the reduction has a corresponding oxidation indicating reversibility for the first one electron reduction of $[Rh^{III}(bpy)_3]^{3+}$. This data suggests the irreversible nature of the $Rh^{III/II/I}$ couple at slower scan rates is due to the $Rh^{II/I}$ couple, indicating a chemical reaction takes place upon generation of Rh^{I}, i.e. loss of a bipyridine. The related complex, $[Rh^{III}(bpy)_2Cl_2]^{+}$, displays an irreversible reduction even when attempting to isolate the first couple. This indicates a reaction following the first one electron reduction to generate Rh^{II} i.e. loss of chloride, Figure 39A. Finally the complex $[Rh^{I}(bpy)_2]^{+}$ shows no reduction corresponding to the $Rh^{III/II/I}$ couple confirming the rhodium based identity

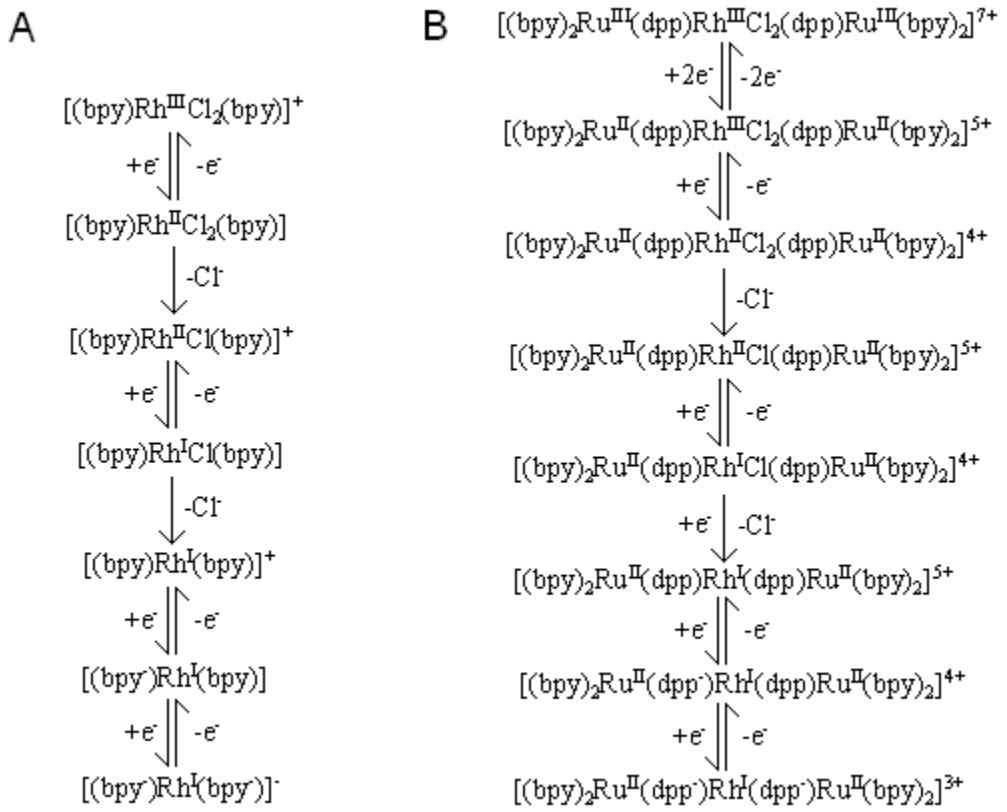

Figure 39. Electrochemical mechanism for the complexes A) $[(bpy)_2RhCl_2](ClO_4)$ (bpy = 2,2'-bipyridine),[67] and B) $[\{(bpy)_2Ru(dpp)\}_2RhCl_2](PF_6)_5$ (dpp = 2,3-bis(2-pyridyl)pyrazine).

of the first reduction in $[Rh^{III}(bpy)_3]^{3+}$ and $[Rh^{III}(bpy)_2Cl_2]^{+}$, Figure 38C.[65] Similar behavior is observed in the trimetallic complex $[(bpy)_2Ru^{II}(dpp)Rh^{I}Cl(dpp)Ru^{II}(bpy)_2]^{4+}$, Figure 39B. Squarewave voltammetry following bulk electrolysis at -0.40 V, Figure 37, shows an oxidation present corresponding to the oxidation of free chloride in solution. The free chloride observed is a result of the loss of chloride following the formation of the square planar Rh^{I} complex, Figure 40.

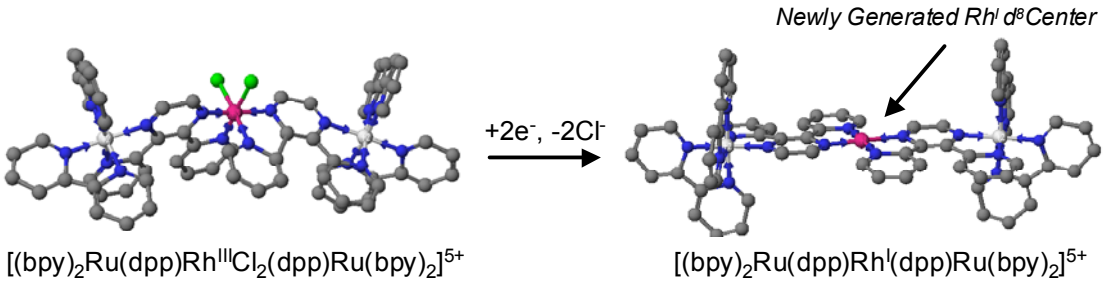

Figure 40. CAChe generated structures for the formation of a Rh^{I} d^8 square planar centered complex following two electron reduction of rhodium.

D. Spectroscopic Properties

Electronic absorption spectroscopy is a powerful technique and easy to perform which can provide information on electronic properties. The electronic absorption spectrum for the complex $[\{(bpy)_2Ru(dpp)\}_2RhCl_2](PF_6)_5$, shown in Figure 41, displays intraligand transitions in the UV and CT transitions in the visible, typical for supramolecular complexes of ruthenium-polyazines. These assignments can be made by examining the spectroscopy of simpler ruthenium-polyazine complexes like $[Ru(bpy)_3]^{2+}$ and $[Ru(bpy)_2(dpp)]^{2+}$, Table 3.[68-69] Gafney examined the electronic absorption spectroscopy of the monometallic precursor $[Ru(bpy)_2(dpp)](PF_6)_2$, Figure 42.[15] Both

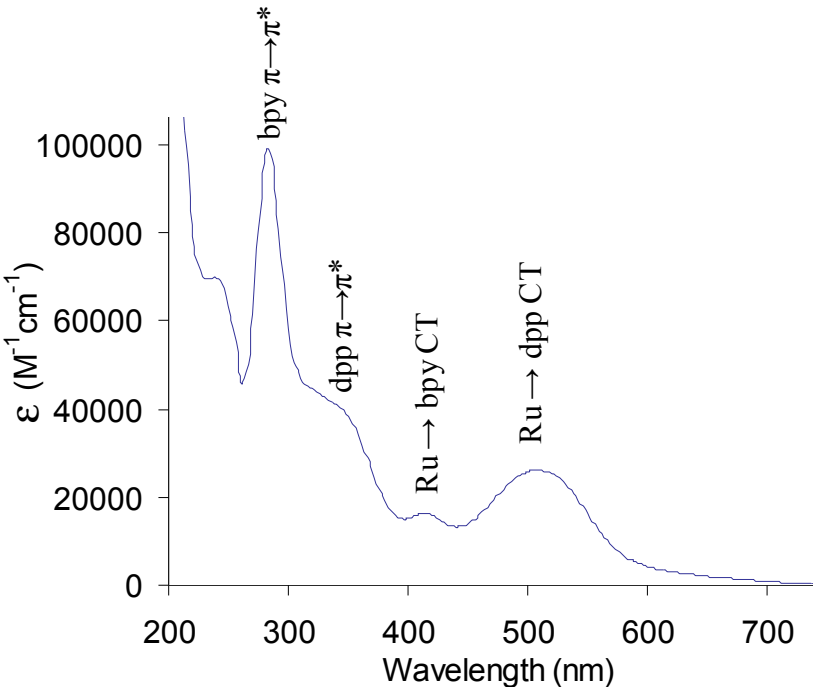

Figure 41. Electronic absorption spectrum for the complex $[\{(bpy)_2Ru(dpp)\}_2RhCl_2](PF_6)_5$ (bpy = 2,2'-bipyridine; dpp = 2,3-bis(2-pyridyl)pyrazine) displaying ligand based π→ π* based transitions in the UV and MLCT transitions in the visible.

Table 3. Spectroscopic properties of ruthenium-polyazine monometallic, bimetallic, and trimetallic complexes. All spectroscopic properties were determined in acetonitrile.

Complex[a]	λ_{max}^{abs} (nm)	ε ($M^{-1}cm^{-1}$)	Assignment	*ref*
$[Ru(bpy)_2(dpp)]^{2+}$	284	66600	bpy, dpp π → π*	*68*
	434	11500	Ru → bpy CT	
	468 sh	11000	Ru → dpp CT	
$[(bpy)_2Ru(dpp)Ru(bpy)_2]^{4+}$	284	114600	bpy, dpp π → π*	*68*
	425	19800	Ru → bpy CT	
	526	24700	Ru → dpp CT	
$[\{(bpy)_2Ru(dpp)\}_2RhCl_2]^{5+}$	284	96400	bpy π → π*	*69*
	344 sh	28700	dpp π → π*	
	414	17400	Ru → bpy CT	
	514	20100	Ru → dpp CT	

a- all complexes are PF_6^- salts

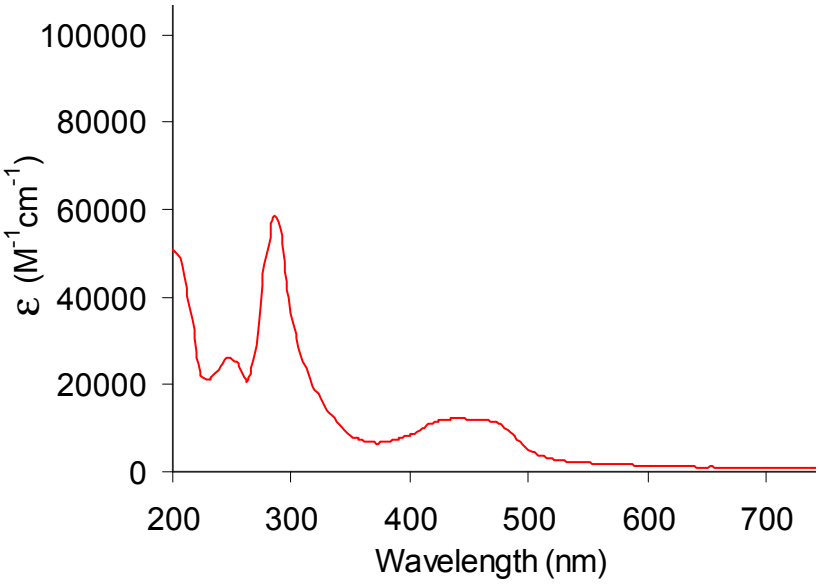

Figure 42. Electronic absorption spectrum for the complex $[(bpy)_2Ru(dpp)](PF_6)_2$ (bpy = 2,2'-bipyridine; dpp = 2,3-bis(2-pyridyl)pyrazine) at 298 K in CH_3CN displaying ligand based $\pi \rightarrow \pi^*$ based transitions in the UV and MLCT transitions in the visible.

bipyridine and dpp based $\pi \rightarrow \pi^*$ transitions are present in the UV region of the spectrum and $Ru(d\pi) \rightarrow bpy(\pi^*)$ and $Ru(d\pi) \rightarrow dpp(\pi^*)$ charge transfer transitions can be seen in the visible region of the spectrum. A similar spectrum is observed in the trimetallic complex $[\{(bpy)_2Ru(dpp)\}_2RhCl_2](PF_6)_5$ with bpy and dpp based $\pi \rightarrow \pi^*$ transitions present in the UV and $Ru(d\pi) \rightarrow bpy(\pi^*)$ and $Ru(d\pi) \rightarrow dpp(\pi^*)$ CT transitions in the visible. Both dpp based transitions, the dpp $\pi \rightarrow \pi^*$ and $Ru(d\pi) \rightarrow dpp(\pi^*)$ CT transitions, are red shifted relative to the monometallic complex $[Ru(bpy)_2(dpp)]^{2+}$. When the BL dpp is bound to two electron withdrawing metal centers, as in the complex $[(bpy)_2Ru(dpp)Ru(bpy)_2](PF_6)_4$, the dpp π^* acceptor orbital is stabilized, decreasing the HOMO-LUMO gap resulting in lower energy $Ru(d\pi) \rightarrow dpp(\pi^*)$ CT transitions. This is evident by the red shift observed in the λ_{max}^{abs} for the $Ru \rightarrow dpp$ CT when comparing the

ruthenium bimetallic complex to the monometallic complex $[Ru(bpy)_2(dpp)](PF_6)_2$. A similar red shift is observed when comparing the trimetallic complex $[\{(bpy)_2Ru(dpp)\}_2RhCl_2](PF_6)_5$ with the monometallic complex $[Ru(bpy)_2(dpp)](PF_6)_2$. Within the trimetallic complex, dpp bridges two electron withdrawing metal centers, a ruthenium(II) and a rhodium(III), which stabilizes the dpp π^* acceptor orbital resulting in a similar shift to lower energy for the Ru $\rightarrow$ dpp CT transition. The lowest energy observable, optically generated electronic transition in the visible region of the spectrum corresponds to the Ru($d\pi$) $\rightarrow$ dpp(π^*) charge transfer transition at 518 nm.

E. Photophysical Properties

1. Emission Spectroscopy

Photophysical properties of the complex $[\{(bpy)_2Ru(dpp)\}_2RhCl_2](PF_6)_5$ were investigated by emission spectroscopy. Population of the lowest lying molecular orbital established by the electrochemical methods (see section VIII. D.) via electron transfer from the higher energy dpp localized orbital is thermodynamically allowed. This rhodium localized lowest lying state is a ^{3}MMCT state. Population of this state by electron transfer can be investigated by emission spectroscopy with the aid of a model complex. The bimetallic complex $[(bpy)_2Ru(dpp)Ru(bpy)_2](PF_6)_4$ was used as a model for determination of electron transfer quenching. The energy state diagrams for the complexes $[(bpy)_2Ru(dpp)Ru(bpy)_2](PF_6)_4$ (left) and $[\{(bpy)_2Ru(dpp)\}_2RhCl_2](PF_6)_5$ (right) are shown in Figure 43.

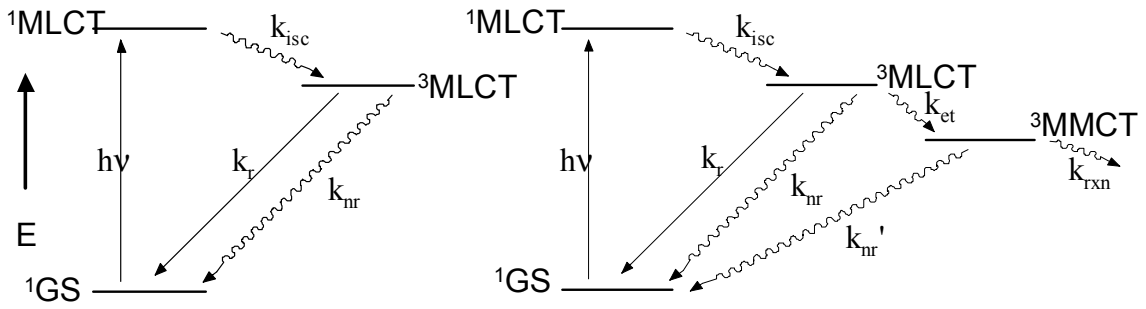

Figure 43. Energy state diagrams for the complexes $[(bpy)_2Ru(dpp)Ru(bpy)_2](PF_6)_4$ (bpy = 2,2'-bipyridine; dpp = 2,3-bis(2-pyridyl)pyrazine), left and $[\{(bpy)_2Ru(dpp)\}_2RhCl_2](PF_6)_5$, right. The bimetallic complex has a Ru → dpp ^{1}CT excited state which is rapidly deactivated by intersystem crossing, k_{isc}, to generate the more stable Ru → dpp ^{3}CT excited state which can undergo radiative or nonradiative decay back to the ground state. In contrast, the trimetallic complex has a ^{3}MMCT excited state that can be populated by electron transfer quenching of the ^{3}MLCT state.

The model complex $[(bpy)_2Ru(dpp)Ru(bpy)_2](PF_6)_4$ possesses an emission from a dpp localized ^{3}MLCT state that is not deactivated by electron transfer to a lower lying state. For this complex to be an effective model, k_r and k_{nr}, the radiative and nonradiative decay rate constants, must be approximately equal to k_r and k_{nr} for the trimetallic complex. The energy gap law states that the closer in energy two states are, the faster the nonradiative rate of deactivation will be. Comparison of the λ_{max}^{abs} and λ_{max}^{em} for the trimetallic complex and the bimetallic model complex can indicate whether or not the bimetallic complex should have similar k_r and k_{nr}. The energy gap law relates directly to deactivation of the ^{3}MLCT state, however, since there is a relation between the ^{1}MLCT and ^{3}MLCT energies, there is some value in the comparison of ^{1}MLCT energies. The λ_{max}^{abs} for the ^{1}MLCT state for the bimetallic model complex is at 524 nm (2.37 eV) while the λ_{max}^{abs} for the ^{1}MLCT state for the trimetallic complex is at 518 nm (2.39 eV), thus a difference of approximately 0.02 eV is observed. The emission spectrum for the trimetallic complex $[\{(bpy)_2Ru(dpp)\}_2RhCl_2](PF_6)_5$ shows phosphorescence from the

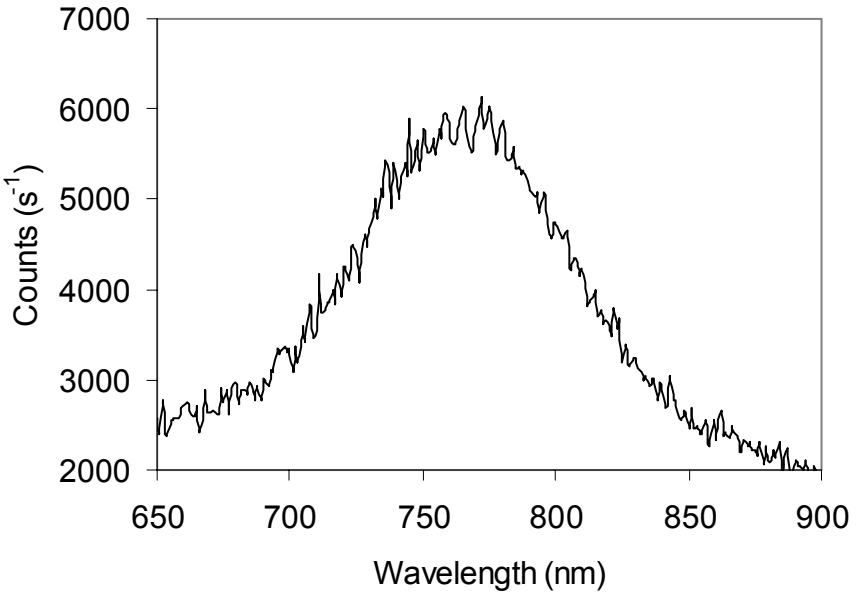

Figure 44. Emission spectrum for the complex $[\{(bpy)_2Ru(dpp)\}_2RhCl_2](PF_6)_5$ (bpy = 2,2'-bipyridine; dpp = 2,3-bis(2-pyridyl)pyrazine) showing phosphorescence from the ^{3}MLCT state.

Ru → dpp based ^{3}MLCT state at 760 nm (1.63 eV), Figure 45, with a quantum yield of emission, Φ^{em}, of 7.3 x 10^{-5}. The model complex $[(bpy)_2Ru(dpp)Ru(bpy)_2](PF_6)_4$ displays phosphorescence out of its dpp localized ^{3}MLCT state at 744 nm (1.67 eV), Figure 44, with a quantum yield of emission of 1.38 x 10^{-3}.[67] The energetically small differences in the ^{3}MLCT states in both the bimetallic and trimetallic complexes as determined by emission spectroscopy support $[(bpy)_2Ru(dpp)Ru(bpy)_2](PF_6)_4$ as an acceptable model for the study of electron transfer quenching from the Ru → dpp CT state for the trimetallic complex. Complex models for determination of excited state rate constants is common within supramolecular photochemistry and the assumptions made herein are in line with those typically made within this area of chemistry.[1] In addition, $E_{1/2}$s for $Ru^{II/III}$ and the first $dpp^{0/-}$ couples for both complexes are similar, which indicates similar ground state redox reactivity. There should be little difference in k_{nr} for

both the trimetallic complex and the bimetallic model complex as related to the energy gap law however some deviation could arise from the two complexes different vibrational modes of deactivation that are a result of structural differences.

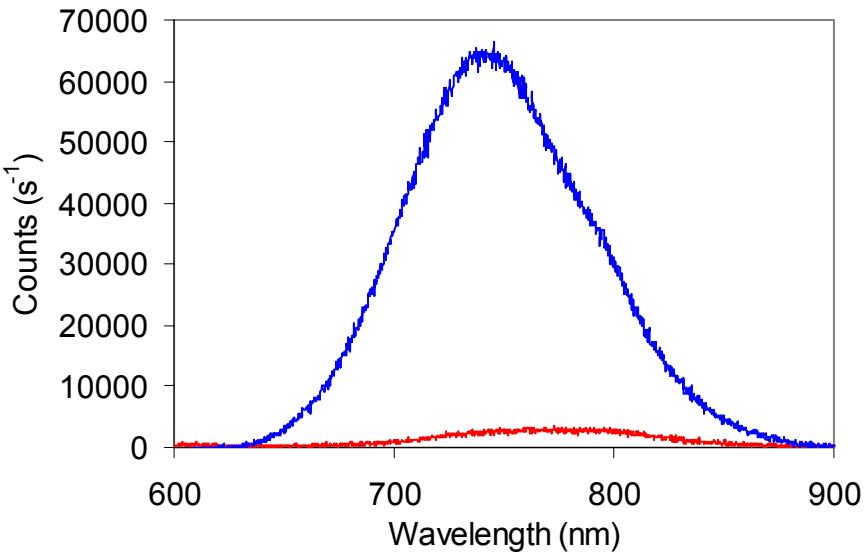

Figure 45. Emission spectrum for both the bimetallic model complex, $[(bpy)_2Ru(dpp)Ru(bpy)_2](PF_6)_4$ (bpy = 2,2'-bipyridine; dpp = 2,3-bis(2-pyridyl)pyrazine) (blue), and the trimetallic complex $[\{(bpy)_2Ru(dpp)\}_2RhCl_2](PF_6)_5$ (red).

2. ^{3}MLCT Excited State Lifetime Determination

The lifetime of the ^{3}MLCT excited state can be determined on a nanosecond timescale by monitoring the emission decay profile after excitation with a nitrogen dye laser. The excited state decay profile for the bimetallic model complex is shown in Figure 46A. The natural log of the decay profile is plotted from which the reciprocal of the slope is the excited state lifetime, τ, shown in Figure 46B. For the model complex, $[(bpy)_2Ru(dpp)Ru(bpy)_2](PF_6)_4$, τ = 150 ns and for the trimetallic complex, $[\{(bpy)_2Ru(dpp)\}_2RhCl_2](PF_6)_5$, τ is estimated to be approximately 8 ns as the lifetime

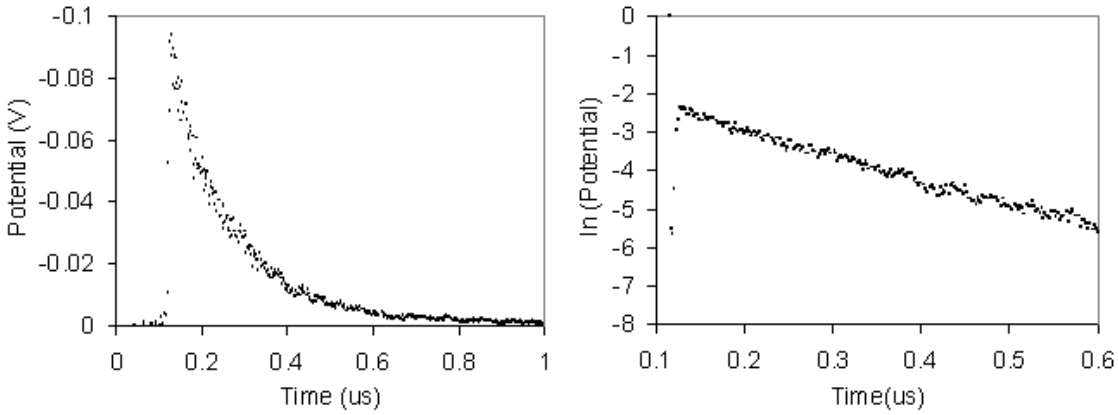

Figure 46. A) Lifetime decay profile for the bimetallic model complex $[(bpy)_2Ru(dpp)Ru(bpy)_2](PF_6)_4$ (bpy = 2,2'-bipyridine; dpp = 2,3-bis(2-pyridyl)pyrazine) and B) the natural log of the decay from which the slope gives the lifetime of the excited state.

approaches the minimum threshold. The rate of electron transfer quenching for the $Ru(d\pi) \rightarrow dpp(\pi^*)$ CT state for the complex $[\{(bpy)_2Ru(dpp)\}_2RhCl_2](PF_6)_5$ can be calculated by emission spectroscopy in conjunction with excited state lifetime measurements using the model complex $[(bpy)_2Ru(dpp)Ru(bpy)_2](PF_6)_4$. Equations 12 and 13 relate the quantum yield of emission with the processes of nonradiative decay (k_{nr}), radiative decay (k_r), and electron transfer (k_{et}).

$$\Phi^{em} \text{ (bimetallic)} = k_r / (k_r + k_{nr}) \qquad \text{(eq12)}$$

$$\Phi^{em} \text{ (trimetallic)} = k_r / (k_r + k_{nr} + k_{et}) \qquad \text{(eq13)}$$

Equation 14 relates the excited state lifetime τ with the deactivation pathways k_r and k_{nr} for the bimetallic complex.

$$\tau \text{ (bimetallic)} = 1 / (k_r + k_{nr}) \qquad \text{(eq14)}$$

Equation 14 can be substituted into equation 12 to give $k_r = (\Phi^{em})(\tau)$ for the bimetallic complex which solves for $k_r = 9.02 \times 10^3\ s^{-1}$. k_{nr} can then be solved using equation 12 resulting in $k_{nr} = 6.53 \times 10^6\ s^{-1}$. With k_r and k_{nr} known for the bimetallic complex the

approximation is made that k_r and k_{nr} are the same for the model complex and the trimetallic complex. Once Φ^{em} (trimetallic) is measured k_{et} can be calculated for the trimetallic complex using equation 13. Using the Φ^{em} for both complexes the rate constant of electron transfer quenching to generate the ^{3}MMCT state was found to be 1.2 x 10^8 s^{-1}. This corresponds to approximately 95% quenching of the ^{3}MLCT state i.e. 95% of the molecules that enter the ^{3}MLCT state that would otherwise decay back to the ground state instead undergo electron transfer to generate the ^{3}MMCT state. If a suitable model complex is available, electron transfer rates are typically determined from both emission quantum yield data using equations 12 and 13, and lifetime data. In this case, however, the lifetime for the trimetallic complex cannot be measured. The excited state lifetime is instead estimated using Φ^{em} for both complexes therefore the rate of electron transfer cannot be calculated from τ.

F. Spectroelectrochemistry

The following spectroelectrochemical and photolysis experiments were conducted to investigate the possibility of photoinitiated electron collection with the current supramolecular architecture. Spectroelectrochemistry was used to explore the properties of the complex $[\{(bpy)_2Ru(dpp)\}_2RhCl_2](PF_6)_5$ in various reduced states. Cyclic and squarewave voltammetry, as discussed in section VIII. C., was used to determine the $E_{1/2}$ values for the two electron rhodium reduction and the first two $dpp^{0/-}$ reductions. The complex was electrochemically reduced first at –0.40 V, just after the two one electron rhodium reductions. This potential was maintained for 60 min and the electronic absorption spectrum was recorded periodically over this time frame, Figure 47. During

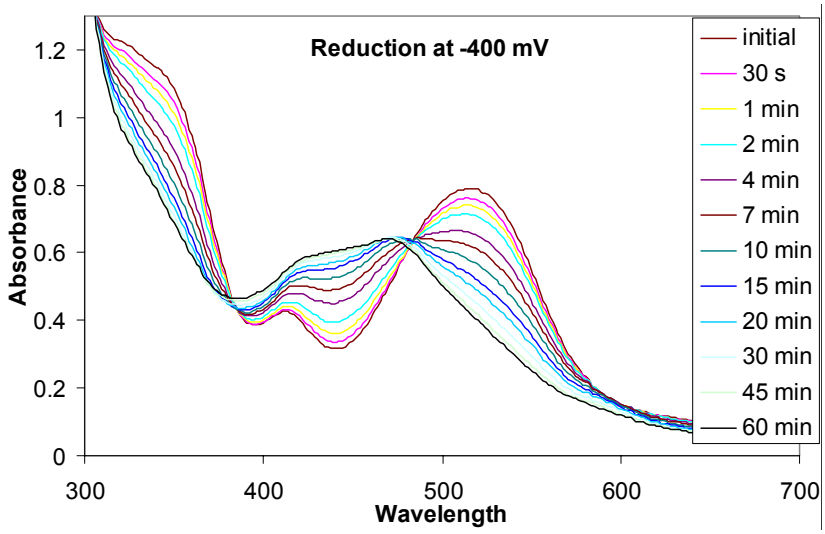

Figure 47. Spectroelectrochemistry for the complex $[\{(bpy)_2Ru(dpp)\}_2RhCl_2](PF_6)_5$ (bpy = 2,2'-bipyridine; dpp = 2,3-bis(2-pyridyl)pyrazine) in multiple redox states. The bulk solution is electrolyzed at –0.40 V for 60 min upon which a spectroscopic change is observed.

this electrolysis period a shift is observed in the electronic absorption spectrum corresponding to the two electron reduction of rhodium(III) to rhodium(I). As electrons are added there is a decreased electron withdrawing and increased electron-donating ability of rhodium(I) as compared to rhodium(III). The increased electron density at the rhodium results in a destabilization of the dpp π^* acceptor orbitals, which results in a blue shift for the Ru($d\pi$) $\rightarrow$ dpp(π^*) CT transition, from 520 nm to 480 nm, observed in the visible region of the electronic absorption spectrum. There is a corresponding movement to higher energy of the dpp based $\pi \rightarrow \pi^*$ band which is observed in the electronic absorption spectrum as the shoulder at 350 nm corresponding to the dpp $\pi \rightarrow \pi^*$ state moves to higher energy where it overlaps with the bpy $\pi \rightarrow \pi^*$ excited state. The Ru $\rightarrow$ bpy CT band at 420 nm is relatively unaffected by Rh reduction. After 30 min of bulk electrolysis these two blue shifts are largely complete. Spectroelectrochemistry

showed the reduction of the rhodium metal center is irreversible due to the loss of chloride as reoxidation of the reduced species did not generate the original spectrum.

G. Photochemical Reactions

Photolysis of $[\{(bpy)_2Ru(dpp)\}_2Rh^{III}Cl_2](PF_6)_5$ at 520 nm (+/- 10 nm) in the presence of a sacrificial electron donor, dimethylaniline (DMA), leads to the same spectroscopic changes as observed in the spectroelectrochemical experiment suggesting the formation of the same reduced species, $[\{(bpy)_2Ru(dpp)\}_2Rh^{I}]^{5+}$, Figure 48. This study combined with the spectroelectrochemical study in section VIII. E. establish this complex as a photoinitiated electron collector. The same blue shift in the Ru(dπ) → dpp(π*) CT transition from 520 nm to 480 nm is observed indicating a Rh^{III} to Rh^{I} reduction has taken place. The changes in the high-energy visible region of the spectrum are obscured due to the absorbance of the concentrated electron donor DMA. The blue

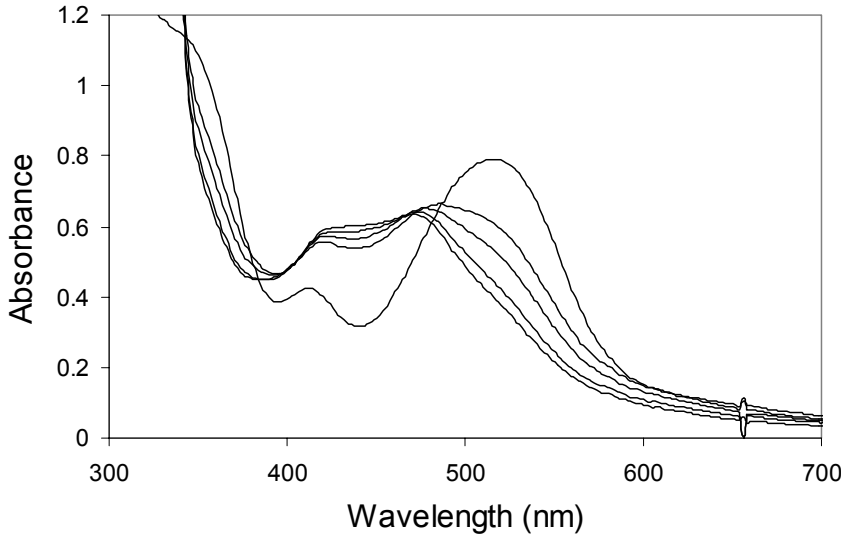

Figure 48. Electronic absorption spectra for the photochemical conversion of $[\{(bpy)_2Ru(dpp)\}_2Rh^{III}Cl_2]^{5+}$ (bpy = 2,2'-bipyridine; dpp = 2,3-bis(2-pyridyl)pyrazine) to the two-electron-reduced form $[\{(bpy)_2Ru(dpp)\}_2Rh^{I}]^{5+}$. 0.31μM complex was photolyzed at 520 (+/- 10 nm) in deoxygenated CH_3CN with 0.29 M DMA.

shift in the Ru(dπ) → dpp(π*) CT transition while undergoing photolysis in the presence of a sacrificial electron donor illustrates the ability of the complex to absorb visible light, and undergo multiple CT reactions leading to the formation of the multiply reduced rhodium metal center, Figure 49. This constitutes photoinitiated electron collection at a metal center. This multielectron process can potentially take place through a variety of mechanisms. Quenching of an excited trimetallic molecule by an electron donor is a part of the proposed mechanism as photolysis of the complex without the electron donor does not lead to the formation of the reduced complex $[\{(bpy)_2Ru(dpp)\}_2Rh^{I}]^{5+}$. There are, however, multiple excited states that can potentially be reductively quenched resulting in a complex mechanism, figure 50. Reductive quenching of both the ^{3}MLCT and ^{3}MMCT states is potentially feasible. A detailed kinetic investigation of this photoreduction is discussed below in section VIII. H.

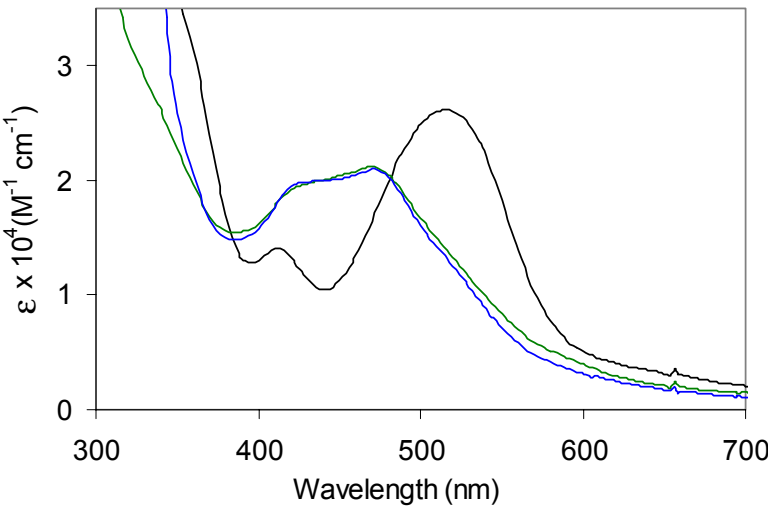

Figure 49. Electronic absorption spectra for the photochemical (blue) and electrochemical (green) conversion of $[\{(bpy)_2Ru(dpp)\}_2Rh^{III}Cl_2]^{5+}$ (bpy = 2,2'-bipyridine; dpp = 2,3-bis(2-pyridyl)pyrazine) to the two-electron-reduced form $[\{(bpy)_2Ru(dpp)\}_2Rh^{I}]^{5+}$.

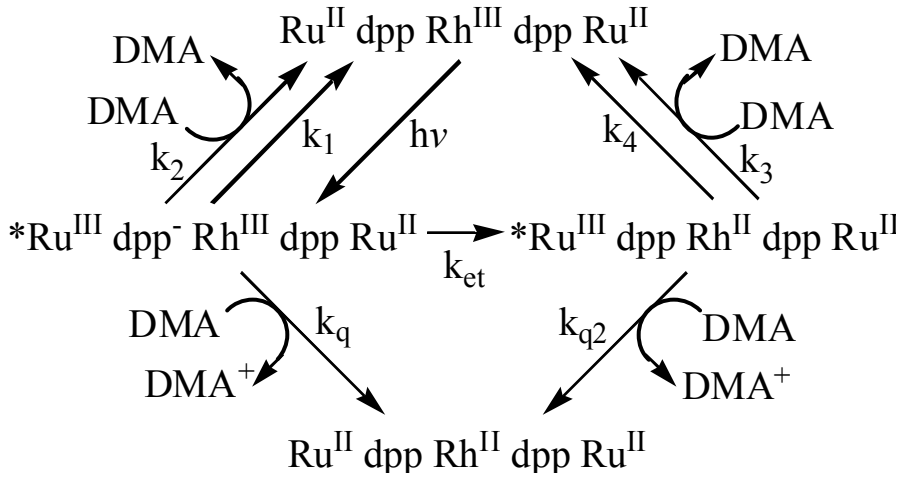

Figure 50. Proposed mechanism for photoinitiated electron transfer. bpy, Cl, and charges are omitted for clarity. $Ru^{II}dppRh^{III}dppRu^{II}$ is $[\{(bpy)_2Ru(dpp)\}_2RhCl_2]^{5+}$ (bpy = 2,2'-bipyridine; dpp = 2,3-bis(2-pyridyl)pyrazine). DMA is N,N-dimethylaniline. k_1 and k_4 are the unimolecular decay pathways from the ^{3}MLCT and ^{3}MMCT states, respectively, whereas k_2 and k_3 are the bimolecular deactivation rates from the same states. k_{et} is the rate of electron transfer to generate the ^{3}MMCT state. k_q and k_{q2} are the rates of reductive quenching by DMA to generate the Rh^{II} complex from the ^{3}MLCT and ^{3}MMCT states, respectively.

H. Kinetic Investigation of Photoinitiated Electron Collection

1. Introduction to Kinetic Analysis

A kinetic investigation has been undertaken to probe photoreduction of $[\{(bpy)_2Ru(dpp)\}_2RhCl_2]^{5+}$ in more detail. The generation of the two-electron-reduced form of the trimetallic complex, $[\{(bpy)_2Ru(dpp)\}_2Rh^{I}]^{5+}$, is assumed to occur through production of the Rh^{II} form, which is consistent with the electrochemical properties of $[Rh(bpy)_2Cl_2]^+$ and $[Rh(dpp)_2Cl_2]^+$.[39,67] The observed electrochemical behavior between the two rhodium monometallic complexes and the trimetallic rhodium core suggests the formation of the rhodium(II) intermediate should be possible. The kinetic analysis

focuses on the initial photochemical steps leading to the first-electron reduction of the trimetallic complex.

An emission-quenching analysis by the electron donor DMA can provide insight into the reactivity of the ^{3}MLCT state. The interaction between *$[Ru(bpy)_3]^{2+}$ and DMA has been studied previously which can serve as a model for the analysis of emission quenching of the trimetallic complex $[\{(bpy)_2Ru(dpp)\}_2Rh^{III}Cl_2](PF_6)_5$.[69,70] The excited-state reduction potential for the species LA, where in this case LA is $[Ru(bpy)_3]^{2+}$, E (LA^{2+}*/LA^+), is equal to the ground state reduction potential, E (LA^{2+}/LA^+), plus the $E_{0\text{-}0}$ energy, eq15.

$$E\ (LA^{2+}*/LA^+) = E\ (LA^{2+}/LA^+) + E_{0\text{-}0} \qquad \text{(eq15)}$$

The $E_{0\text{-}0}$ energy is the energy between the ground vibrational state of the first electronic excited state to the ground vibrational, ground electronic state, which is often estimated

$$LA^{2+} + h\nu \rightarrow *LA^{2+} \qquad \text{(rxn23)}$$

$$*LA^{2+} + ED \rightarrow LA^+ + ED^+ \qquad \text{(rxn24)}$$

by emission spectroscopy. The excited state reduction potential for $[Ru(bpy)_3]^{2+}$, E(A^{2+*}/A^+), is 0.77 V while the oxidation potential for DMA is 0.81 V (vs SCE).[70] In this case there is a small driving force for reductive quenching of *$[Ru(bpy)_3]^{2+}$. This results in quenching of the ^{3}MLCT for $[Ru(bpy)_3]^{2+}$, k_q, by DMA at a rate of 7.1 x 10^7 $M^{-1}s^{-1}$. The back electron transfer rate, k_b, the rate of the reverse process of k_q resulting in the reoxidation of the reduced complex, was determined to be 4.1 x 10^9 $M^{-1}s^{-1}$.[69,70] The rate of back electron transfer was determined to be much faster than the forward rate which is common in transition metal-polyazine coordination complexes resulting in an overall slower rate for generation of the reduced species. The excited-state reduction potential

for $[\{(bpy)_2Ru(dpp)\}_2RhCl_2]^{5+}$ is 0.90 V. There is a comparative increase in driving force for reductive quenching of the Ru → dpp CT state by DMA. The ^{3}MLCT state of the trimetallic complex, however, can undergo competitive electron transfer to Rh to generate the ^{3}MMCT state. This gives rise to a complicated mechanism, Figure 50. This complicated mechanism is still less complex compared to the overall mechanism involving the formation of the two electron reduced product which can be formed through additional multiple paths including disproportionation. The mechanism including the formation of the two electron reduced species $[\{(bpy)_2Ru(dpp)\}_2Rh^I]^{5+}$ will be briefly covered from a qualitative standpoint in section VIII. H. 6.

2. Emission Quenching Analysis

An emission-quenching analysis by the electron donor DMA can provide insight into the reactivity of the ^{3}MLCT state. The formation of the ^{3}MLCT excited state proceeds by optical population of the ^{1}MLCT state followed by intersystem crossing to generate the ^{3}MLCT state, which is represented kinetically as I_a (rxn25). Overall charges, bpy, and Cl are omitted for clarity.

$$Ru^{II}\ dpp\ Rh^{III}\ dpp\ Ru^{II} + h\nu \xrightarrow{I_a} {}^*Ru^{III}\ dpp^-\ Rh^{III}\ dpp\ Ru^{II} \quad \text{(rxn25)}$$

$${}^*Ru^{III}\ dpp^-\ Rh^{III}\ dpp\ Ru^{II} \xrightarrow{k_1} Ru^{II}\ dpp\ Rh^{III}\ dpp\ Ru^{II} \quad \text{(rxn26)}$$

$${}^*Ru^{III}\ dpp^-\ Rh^{III}\ dpp\ Ru^{II} + DMA \xrightarrow{k_2} Ru^{II}\ dpp\ Rh^{III}\ dpp\ Ru^{II} + DMA \quad \text{(rxn27)}$$

$${}^*Ru^{III}\ dpp^-\ Rh^{III}\ dpp\ Ru^{II} + DMA \xrightarrow{k_q} Ru^{II}\ dpp^-\ Rh^{III}\ dpp\ Ru^{II} + DMA^+ \quad \text{(rxn28)}$$

$${}^*Ru^{III}\ dpp^-\ Rh^{III}\ dpp\ Ru^{II} \xrightarrow{k_{et}} {}^*Ru^{III}\ dpp\ Rh^{II}\ dpp\ Ru^{II} \quad \text{(rxn29)}$$

$${}^*Ru^{III}\ dpp\ Rh^{II}\ dpp\ Ru^{II} \xrightarrow{k_4} Ru^{II}\ dpp\ Rh^{III}\ dpp\ Ru^{II} \quad \text{(rxn30)}$$

$${}^*Ru^{III}\ dpp\ Rh^{II}\ dpp\ Ru^{II} + DMA \xrightarrow{k_3} Ru^{II}\ dpp\ Rh^{III}\ dpp\ Ru^{II} + DMA \quad \text{(rxn31)}$$

$${}^*Ru^{III}\ dpp\ Rh^{II}\ dpp\ Ru^{II} + DMA \xrightarrow{k_{q2}} Ru^{II}\ dpp\ Rh^{II}\ dpp\ Ru^{II} + DMA^+ \quad \text{(rxn32)}$$

The ^{3}MLCT state can then decay through radiative (k_r) or nonradiative processes (k_{nr}), k_1 ($k_1 = k_r + k_{nr}$), back to the ground state (rxn26). In the presence of an electron donor the ^{3}MLCT state can be deactivated through a bimolecular nonradiative/energy transfer process (rxn27) or can be reductively quenched to generate the one electron reduced product (rxn28). The ^{3}MLCT state can also undergo intramolecular electron transfer quenching (section VIII. D.) to generate the ^{3}MMCT state (rxn29). The ^{3}MMCT state can deactivate to the ground state through nonradiative decay or possibly radiative decay, however, if the radiative pathway is active, its emission is either too weak and/or to low in energy to be detected by the available instrumentation (rxn30). In the presence of an electron donor the ^{3}MMCT state can be deactivated through a bimolecular reaction (rxn31) or can be reductively quenched to generate the one electron reduced product (rxn32).

A kinetic analysis of emission quenching of the ^{3}MLCT state of $[\{(bpy)_2Ru(dpp)\}_2RhCl_2]^{5+}$ by DMA can provide information on the mechanism for the formation of the one electron reduced product $[\{(bpy)_2Ru(dpp)\}_2Rh^{I}Cl]^{5+}$. Experimentally, the quantum yield of emission of the ^{3}MLCT state was monitored as the sacrificial donor DMA was added. If reductive quenching is dependent on DMA concentration, i.e. reactions 28 and 32, altering the electron donor concentration should have an experimentally observable impact. The emission spectrum shows the impact of adding DMA, Figure 51A, displaying increased quenching as the concentration of DMA is increased. A Stern-Volmer analysis of the data, plotting the quantum yield of the ^{3}MLCT state for the complex $[\{(bpy)_2Ru(dpp)\}_2RhCl_2]^{5+}$ without the presence of an electron donor, Φ_o^{em}, versus the quantum yield of the ^{3}MLCT state with varying donor

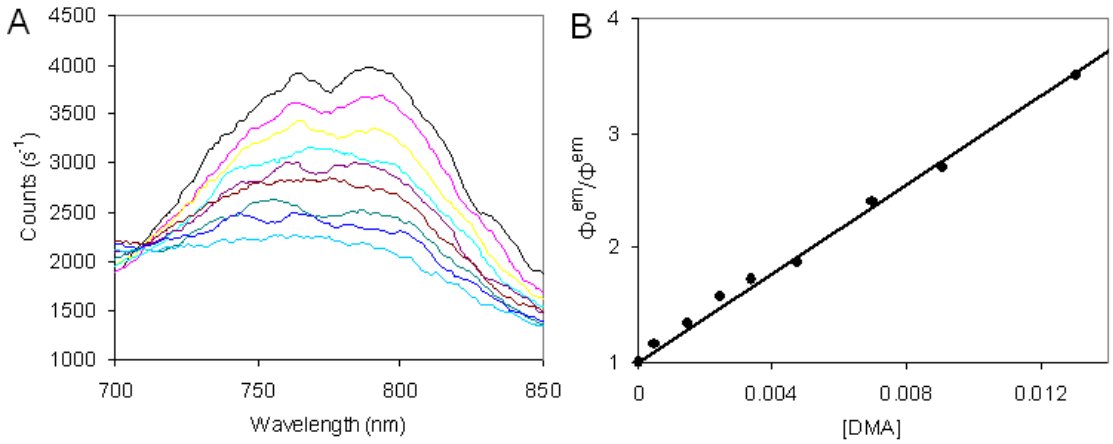

Figure 51. A) Emission spectrum for the complex $[\{(bpy)_2Ru(dpp)\}_2RhCl_2]^{5+}$ (bpy = 2,2'-bipyridine; dpp = 2,3-bis(2-pyridyl)pyrazine) displaying quenching with varying concentrations of electron donor. B) Plot of the degree of quenching versus electron donor concentration.

concentrations, Φ^{em}, Figure 51B, using the mechanism in figure 50 can be written as

$$\Phi_o^{em}/\Phi^{em} = 1 + (k_q + k_2)[DMA]/(k_1 + k_{et}) \qquad \text{(eq16)}$$

Emission from the ^{3}MLCT state of $[\{(bpy)_2Ru(dpp)\}_2RhCl_2](PF_6)_5$ is quenched efficiently by DMA. The slope of the Stern-Volmer plot (using $k_1 = k_r + k_{nr} = 1.2 \times 10^8$ s^{-1}) yields $k_q + k_2 = 2.37 \pm 0.01 \times 10^{10}$ M^{-1} s^{-1}, which is consistent with efficient ^{3}MLCT emission quenching. Back electron transfer for amine quenching of ruthenium polyazine systems is often efficient, reducing the net product formation. In the case of $*[Ru(bpy)_3]^{2+}$ quenched by DMA, the back electron transfer rate, $k_b = 4.1 \times 10^9$ M^{-1} s^{-1}, is two orders of magnitude larger than the forward rate of quenching, k_q, which is 7.1×10^7 M^{-1} s^{-1}.[69,70] The rate of bimolecular quenching, 2×10^{10} M^{-1} s^{-1}, is approximately four times the rate of diffusion which is typically estimated to be ~5×10^9 M^{-1} s^{-1}. This can be explained through a discussion on the types of quenching.

Two types of quenching of note are dynamic quenching and static quenching. Both modes of quenching are usually concentration dependent, however, dynamic

quenching is a diffusion controlled process whereas static quenching is not. For static quenching to take place, there must be a preassociation of the electron donor and the substrate. In the case of an excited trimetallic complex quenched by DMA, bimolecular quenching is not diffusion controlled, therefore static quenching must contribute to the overall rate of quenching.

3. Stern-Volmer Analysis of Product Formation via the ^{3}MLCT State

An investigation into the excited state reactivity of the complex $[\{(bpy)_2Ru(dpp)\}_2RhCl_2](PF_6)_5$ can benefit from a Stern-Volmer analysis of product formation. One potential excited state reaction can involve reductive quenching of the ^{3}MLCT state by the electron donor DMA, Figure 50. Due to the complexity of the mechanism for the formation of the rhodium(II) centered trimetallic complex it is necessary to treat each of the two paths from a kinetic standpoint separately. Each of these two paths for product formation, reductive quenching of the ^{3}MLCT state and reductive quenching of the ^{3}MMCT state are analyzed separately below in order to solve for the rate constants of reductive quenching.

The electron donor, N,N-dimethylaniline (DMA), was chosen in part because it is a sacrificial electron donor, i.e. an irreversible electron donor. The anodic oxidation of dimethylaniline has been studied previously, which shows its irreversible nature.[72-76] Upon electrochemical oxidation DMA forms a cation radical, Figure 52, which can be written with several resonance forms. The resonance form with the unpaired electron in the para position is probably an important contribution. Two $DMA^{+\bullet}$ radicals can then dimerize to form tetramethylbenzidine (TMB), shown in Figure 52. TMB, a neutral

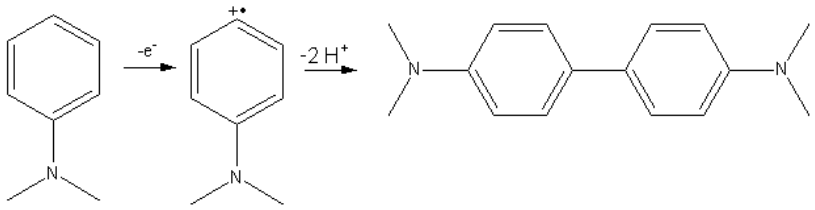

Figure 52. Reaction scheme showing the dimerization of the oxidation products of N,N-dimethylaniline.

species, is not as good an electron acceptor as a $DMA^{+\bullet}$ radical cation, which can impact back electron transfer.

A series of experiments with varying donor concentrations while monitoring product formation were used to conduct a Stern-Volmer analysis. Figure 53 is one example of such an experiment showing the formation of the two electron reduced photoproduct in the presence of 0.20 M DMA. Individual experiments were evaluated in terms of quantum yield with respect to the formation of the two electron reduced product with the assumption that the formation of the one electron reduced product is an

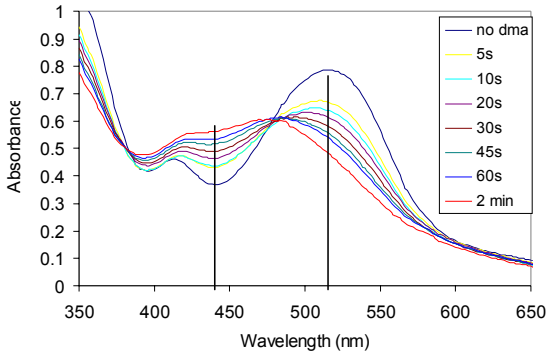

% converted measured at 518 nm

[DMA]	no dma	initial	5 s	10 s	20 s	30 s	45 s	60 s	120 s
0.025	0	0.004	0.13	0.16	0.19	0.23	0.26	0.28	
0.033	0	0.015	0.16	0.21	0.26	0.27	0.30	0.35	
0.05	0	0.003	0.13	0.19	0.25	0.30	0.36	0.40	
0.1	0	0.010	0.26	0.33	0.43	0.50	0.52	0.60	
0.2	0	-0.037	0.38	0.48	0.56	0.67	0.76	0.81	1.00

% converted measured at 440 nm

[DMA]	no dma	initial	5 s	10 s	20 s	30 s	45 s	60 s	120 s
0.025	0	0.010	0.20	0.25	0.31	0.32	0.40	0.44	
0.033	0	0.070	0.22	0.25	0.30	0.37	0.42	0.46	
0.05	0	0.12	0.29	0.34	0.40	0.44	0.48	0.55	
0.1	0	0.15	0.51	0.57	0.59	0.62	0.68	0.71	
0.2	0	0.32	0.49	0.51	0.62	0.72	0.82	0.89	1.00

Figure 53. Electronic absorption spectrum for the complex $[\{(bpy)_2Ru(dpp)\}_2RhCl_2]^{5+}$ (bpy = 2,2'-bipyridine; dpp = 2,3-bis(2-pyridyl)pyrazine) with 0.20 M DMA over time. Formation of the two electron reduced product occurs as the λ_{max}^{abs} for the MLCT shifts to higher energy. The conversion to the reduced product is evaluated in terms of % converted where the spectrum at 120 seconds is "complete", and is evaluated at two wavelengths, 440 nm and 518 nm. From the % converted a quantum yield for the formation of the reduced product can be determined for each time interval.

intermediate step that occurs initially. This is consistent with the properties of $[Rh(bpy)_2Cl_2]^+$ and $[Rh(dpp)_2Cl_2]^+$.[67,69] The conversion to the reduced product is evaluated in terms of % converted where the spectrum at 120 seconds is considered "complete". Accurate determination of the % converted is difficult so two wavelengths, 440 nm and 518 nm, are evaluated and averaged. From the % converted a quantum yield for the formation of the reduced product can be determined for each time interval. Determination of quantum yields are difficult for two reasons, the accurate determination of the product formation and the accurate determination of the light absorbed. At early photolysis times, <5 seconds, the formation of Rh^{II} should dominate and would display Ru → dpp CT transitions intermediate between the Rh^{III} and Rh^{I} forms. At high donor concentrations the initial quantum yield approaches unity, Figure 54A. The limiting quantum yield was estimated using the quantum yield determined at 5 seconds. Product formation can occur from the ^{3}MLCT or ^{3}MMCT state or a combination of both. An in depth analysis is necessary to tackle the kinetics of this complex mechanism, Figure 50.

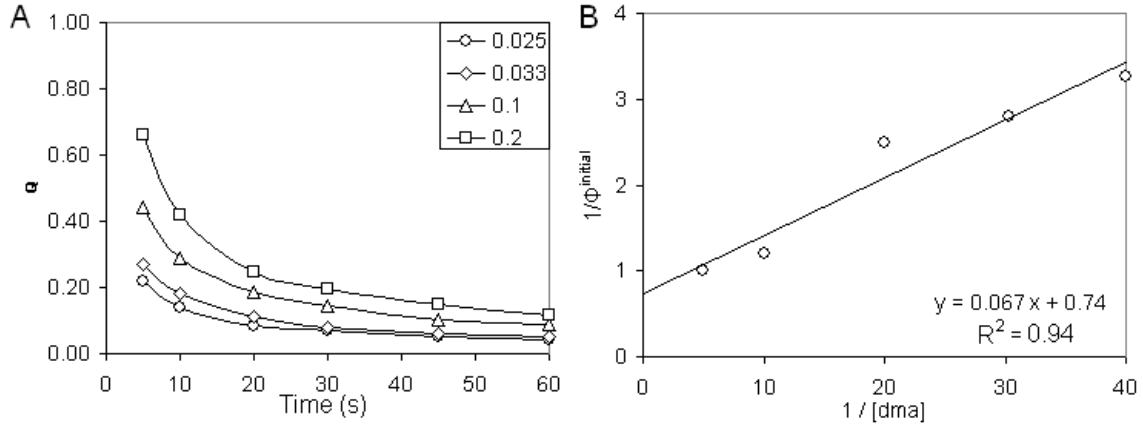

Figure 54. A) Quantum yield for the formation of the one electron reduced photoproduct in the presence of varying electron donor concentrations. The limiting quantum yield was estimated using the quantum yield determined at five seconds. B) Stern-Volmer plot for the formation of the one electron reduced rhodium(II) intermediate plotting the reciprocal of the limiting quantum yield versus the reciprocal of the electron donor concentration.

If product formation primarily comes via the ^{3}MLCT state, kinetically, k_{et} is considered a deactivation pathway (rxn35) along with k_1 (rxn34) and k_2 (rxn36). Abbreviations used for kinetic analysis are shown in {wavy brackets}.

$$Ru^{II}\ dpp\ Rh^{III}\ dpp\ Ru^{II} + h\nu \xrightarrow{I_a} {}^*Ru^{III}\ dpp^-\ Rh^{III}\ dpp\ Ru^{II}\ \{MLCT\} \quad \text{(rxn33)}$$

$${}^*Ru^{III}\ dpp^-\ Rh^{III}\ dpp\ Ru^{II} \xrightarrow{k_1} Ru^{II}\ dpp\ Rh^{III}\ dpp\ Ru^{II}\ \{GS\} \quad \text{(rxn34)}$$

$${}^*Ru^{III}\ dpp^-\ Rh^{III}\ dpp\ Ru^{II} \xrightarrow{k_{et}} Ru^{II}\ dpp\ Rh^{III}\ dpp\ Ru^{II}\ \{MMCT\} \quad \text{(rxn35)}$$

$${}^*Ru^{III}\ dpp^-\ Rh^{III}\ dpp\ Ru^{II} + DMA \xrightarrow{k_2} Ru^{II}\ dpp\ Rh^{III}\ dpp\ Ru^{II} \quad \text{(rxn36)}$$

$${}^*Ru^{III}\ dpp^-\ Rh^{III}\ dpp\ Ru^{II} + DMA \xrightarrow{k_q} Ru^{II}\ dpp\ Rh^{II}\ dpp\ Ru^{II}\ \{reduced\} \quad \text{(rxn37)}$$

The quantum yield for the formation of the product, Φ (Ru^{II} dpp Rh^{II} dpp Ru^{II}), can be defined as

$$\Phi\{reduced\} = [\{reduced\}] / I_a \quad \text{(eq17)}$$

where the concentration of the reduced product, [{reduced}], is dependent on the concentration of the complex in the ^{3}MLCT state and the concentration of the electron donor (eq18).

$$[\{reduced\}] = k_q[\{MLCT\}][DMA] \quad \text{(eq18)}$$

Equation 18 can be substituted into equation 17 and rearranged to generate equation 19.

$$[\{MLCT\}] = \frac{\Phi\{reduced\}\cdot I_a}{k_q[DMA]} \quad \text{(eq19)}$$

A steady state approximation is made such that the change in the concentration of the molecules in the ^{3}MLCT excited state, d[{MLCT}]/dt, is zero, where in a constant photolysis experiment such an approximation is appropriate.

$$\frac{d[\{MLCT\}]}{dt} = 0 = I_a - k_1[\{MLCT\}] - k_{et}[\{MLCT\}] - k_q[\{MLCT\}][DMA] - k_2[\{MLCT\}][DMA] \quad \text{(eq20)}$$

Equation 20 relates the steady state approximation for the concentration of the complex in its ^{3}MLCT excited state with the formation and deactivation of this state through both unimolecular (k_1, k_{et}) and bimolecular (k_q, k_2) processes. Equation 19 can be substituted into equation 20 and rearranged to equation 21

$$1/\Phi = (k_1 + k_{et})/(k_q[DMA]) + (k_q + k_2)/k_q \quad \text{(eq21)}$$

where $1/\Phi$ can be plotted versus 1/[DMA], Figure 54B.

From Figure 54B the slope of this plot, 0.065, is equal to $(k_1+k_{et})/k_q$, where both k_1 and k_{et} are known, allowing one to solve for k_q which is $1.9 \pm 0.1 \times 10^9$ M^{-1} s^{-1}. k_q for quenching of the trimetallic complex by DMA is higher relative to quenching of $[Ru(bpy)_3]^{2+}$ by DMA which is consistent with the increased driving force for electron transfer.

4. Stern-Volmer Analysis of Product Formation via the ^{3}MMCT State

If product formation comes primarily from the ^{3}MMCT state, the following kinetic pathways are used to determine the rate of product formation.

$$Ru^{II}\ dpp\ Rh^{III}\ dpp\ Ru^{II} + h\nu \xrightarrow{I_a} *Ru^{III}\ dpp^{-}\ Rh^{III}\ dpp\ Ru^{II}\ \{MLCT\} \quad \text{(rxn38)}$$

$$*Ru^{III}\ dpp^{-}\ Rh^{III}\ dpp\ Ru^{II} \xrightarrow{k_{et}} *Ru^{III}\ dpp\ Rh^{II}\ dpp\ Ru^{II}\ \{MMCT\} \quad \text{(rxn39)}$$

$$*Ru^{III}\ dpp\ Rh^{II}\ dpp\ Ru^{II} + DMA \xrightarrow{k_4} Ru^{II}\ dpp\ Rh^{III}\ dpp\ Ru^{II}\ \{GS\} \quad \text{(rxn40)}$$

$$*Ru^{III}\ dpp\ Rh^{II}\ dpp\ Ru^{II} + DMA \xrightarrow{k_{q2}} Ru^{II}\ dpp\ Rh^{II}\ dpp\ Ru^{II}\ \{reduced\} \quad \text{(rxn41)}$$

The quantum yield for the formation of the product, Φ (Ru^{II} dpp Rh^{II} dpp Ru^{II}), is still defined as

$$\Phi\{reduced\} = [\{reduced\}] / I_a \quad \text{(eq18)}$$

however the concentration of the product (Ru^{II} dpp Rh^{II} dpp Ru^{II}) is dependent on the concentration of the complex in the ^{3}MMCT state and the concentration of the electron donor which can be stated as

$$[\{reduced\}] = k_{q2} \cdot \Phi\{MMCT\}[\{MMCT\}][DMA] \quad \text{(eq22)}$$

This can be substituted into equation 17 and rearranged to generate equation 23.

$$[\{MMCT\}] = \frac{\Phi\{reduced\} \cdot I_a}{k_{q2} \cdot \Phi\{MMCT\}[DMA]} \quad \text{(eq23)}$$

A steady state approximation is made such that the change in the concentration of the molecules in the ^{3}MMCT excited state, d[{MMCT}]/dt, is zero, where in a constant photolysis experiment such an approximation is appropriate.

$$\frac{d[\{MMCT\}]}{dt} = 0 = I_a - k_4[\{MMCT\}] - k_{q2}[\{MMCT\}][DMA] - k_3[\{MMCT\}][DMA] \quad \text{(eq24)}$$

Equation 24 relates the steady state approximation for the concentration of the complex in its ^{3}MMCT excited state with the formation and deactivation of this state through both unimolecular (k_4) and bimolecular (k_{q2}, k_3) processes. Equation 23 can be substituted into equation 24 can be rearranged to generate equation 25.

$$1/\Phi = (k_4)/(\Phi\{MMCT\}k_{q2}[DMA]) + (k_{q2} + k_3)/k_{q2} \quad \text{(eq25)}$$

where $1/\Phi$ can be plotted versus 1/[DMA], figure 52B.

If the rhodium(II) product results from quenching of the ^{3}MMCT state, k_4/k_{q2} is 0.062 ± 0.004 and the value of k_{q2} would depend on the lifetime of the ^{3}MMCT state. Emission spectroscopy with a red sensitive photomultiplier tube was unable to detect emission from the lower energy ^{3}MMCT state. Either the emission energy is too low to be detected by the available instrumentation or the radiative component is not intense enough to be detected. The potential difference for the $Rh^{III/II/I}$ and $dpp^{0/-}$ couples,

measured electrochemically, predicts a ^{3}MMCT state λ_{max} of greater than 1000 nm where even the red sensitive Hamamatsu 1527 photomultiplier tube loses most of its sensitivity. Related trischelated systems show rapid back electron transfer (7.1×10^9 s^{-1}),[31] which would require a very large k_{q2} for the ^{3}MMCT path to lead to product. If the rate of charge recombination in the trimetallic complex $[\{(bpy)_2Ru(dpp)\}_2RhCl_2](PF_6)_5$ is similar, this would result in a k_{q2} of 1.1×10^{11}. Considering the much smaller driving force for quenching the ^{3}MMCT as compared to the ^{3}MLCT state, it is unlikely the k_{q2} rate constant would be so large. The above emission-quenching analysis and this product formation analysis suggest quenching of the ^{3}MLCT state may be the primary path for the formation of product however quenching of the ^{3}MMCT state may contribute as well.

5. Impact of Driving Force of Reductive Quenching

Investigation of the driving force for reductive quenching of both the ^{3}MLCT and ^{3}MMCT states by the electron donor may be useful in determining the mechanism for the formation of the photoreduced complex. The excited state reduction potential for the ^{3}MLCT state for the complex $[\{(bpy)_2Ru(dpp)\}_2Rh^{III}Cl_2](PF_6)_5$ can be calculated using equation 5. The $E_{0\text{-}0}$ energy was estimated to be 1.61 V from the ^{3}MLCT $\lambda_{max}{}^{em}$ of 770 nm measured by emission spectroscopy resulting in an excited state reduction potential of 1.29 V (vs. SCE). Since no phosphorescence is observed from the ^{3}MMCT state the $E_{0\text{-}0}$ for this state cannot be measured, however a rough estimation can be made from the measured electrochemical potentials for the first dpp and rhodium couples since the orbitals involved in the some of the electrochemical processes are the same as the orbitals involved in the HOMO and LUMO. The first electrochemical oxidative process, the

oxidation of $Ru^{II/III}$, corresponds to the removal of an electron from the HOMO, while the first rhodium based reduction corresponds to the addition of an electron into the LUMO. The energy gap between these two processes is indicative of the gap between the HOMO and LUMO.

The $E_{0\text{-}0}$ energy for the ^{3}MMCT state was estimated using the ^{3}MLCT energy with an adjustment made for the difference in the $Rh^{III/II/I}$ couple versus the first $dpp^{0/-}$ couple. By subtracting the energy difference from the first $dpp^{0/-}$ and rhodium reductions (0.39 V) from the $E_{0\text{-}0}$ energy for the ^{3}MLCT state results in an $E_{0\text{-}0}$ of 0.90 V for the ^{3}MMCT state. Using equation 5 the excited state reduction potential for the ^{3}MMCT state can be calculated to be 0.90 V.

The oxidation potential for N,N-dimethylaniline is 0.81 V (vs SCE).[70] The driving force for reductive quenching can be calculated by subtracting the oxidation potential from the excited state reduction potential, eq 26,

$$E \text{ (driving force)} = E\ (A^{+*}/A^0) + E\ (Q^0/Q^+) \qquad \text{(eq26)}$$

where Q is the quencher or electron donor. This results in a positive driving force for reductive quenching of the ^{3}MLCT state of 0.48 V and a very small driving force, ~0.09 V, for reductive quenching of the ^{3}MMCT state. Considering only the thermodynamic driving force, the rate of quenching of the ^{3}MLCT state should be larger than that of the ^{3}MMCT state.

6. Modulation of Driving Force using Alternative Electron Donors

Alternative electron donors can be used to modulate the driving force for reductive quenching for both the ^{3}MLCT and ^{3}MMCT states. Selecting donors with a

larger oxidation potential will decrease the driving force for quenching of the ^{3}MLCT state. If the observed rate of photoreduced product is impacted, then quenching of the ^{3}MLCT state is most likely important to the overall mechanism. In this scenario, the driving force for quenching of the ^{3}MMCT state is essentially zero so any changes to the rate are most likely due to quenching of the ^{3}MLCT state.

Alternatively, an electron donor with a less positive oxidation potential can be selected resulting in an increase in the driving force for quenching both the ^{3}MLCT and ^{3}MMCT states. If there is a large increase in the rate of product formation it is possible that quenching of the ^{3}MMCT is an operable mechanism of quenching. In this scenario, the driving force for reductive quenching of the ^{3}MMCT state is increased from essentially zero to a large value. Any increase in the observed rate, however, cannot only be attributed to quenching of the ^{3}MMCT since it is possible that the increase in driving force for quenching of the ^{3}MLCT state contributes to the overall increase in product formation.

An emission quenching Stern-Volmer analysis can provide information on the degree of impact various electron donors will have on the ^{3}MLCT state by selecting donors, as in the first example above, that have no driving force for quenching the ^{3}MMCT state. This information coupled with data from the product formation experiments can provide a better understanding of the mechanism. The rate constant of quenching of the ^{3}MLCT state, k_q, which is 1.9×10^9 M^{-1} s^{-1}, is in line with rates of reductive quenching of $[Ru(bpy)_3]^{2+}$ with similar driving forces.[71] If the rhodium(II) product results from quenching of the ^{3}MMCT state, $k_4/k_{q2} = 0.062$ and the value of k_{q2} would depend on the lifetime of the ^{3}MMCT state. Related trischelated systems show

rapid back electron transfer (7.1×10^9 s^{-1}),[31] which would require a very large k_{q2} for the ^{3}MMCT path to lead to product. The above emission-quenching analysis suggests quenching of the ^{3}MLCT state may be more likely, however, it cannot be ruled out from the present data that both the ^{3}MLCT and ^{3}MMCT states may lead to photoreduced products.

Driving force for reductive quenching is not the only factor to consider when selecting an electron donor. Donor-complex, donor-solvent, and complex-solvent interactions can all impact device functioning and any difference in the rate of formation of the photoreduced product must be elucidated from these interactions.

An emission quenching analysis with an alternative electron donor was undertaken to further investigate the mechanism of the photoreduction of $[\{(bpy)_2Ru(dpp)\}_2RhCl_2]^{5+}$. The electron donor phenothiazine was used which has an oxidation potential of 0.53 V. The driving force for reductive quenching of the ^{3}MLCT state is 0.76 V, an increase of 0.28 V relative to DMA, while the driving force for reductive quenching of the ^{3}MMCT state is increased from ~0.09 V to ~0.37 V. Experimentally, the quantum yield of emission of the ^{3}MLCT state was monitored as the electron donor phenothiazine was added. DMA concentration was shown to have an impact on emission quenching. If phenothiazine has similar impact, the addition of phenothiazine should result in a decrease of the quantum yield of emission. This is observed experimentally, Figure 55A. A Stern-Volmer analysis of the data, plotting the quantum yield of emission from the ^{3}MLCT state for the complex $[\{(bpy)_2Ru(dpp)\}_2RhCl_2]^{5+}$ without the presence of an electron donor, Φ_o^{em}, versus the quantum yield of the ^{3}MLCT state with varying donor concentrations, Φ^{em}, Figure 55B, using the mechanism in Figure 50 can be written as,

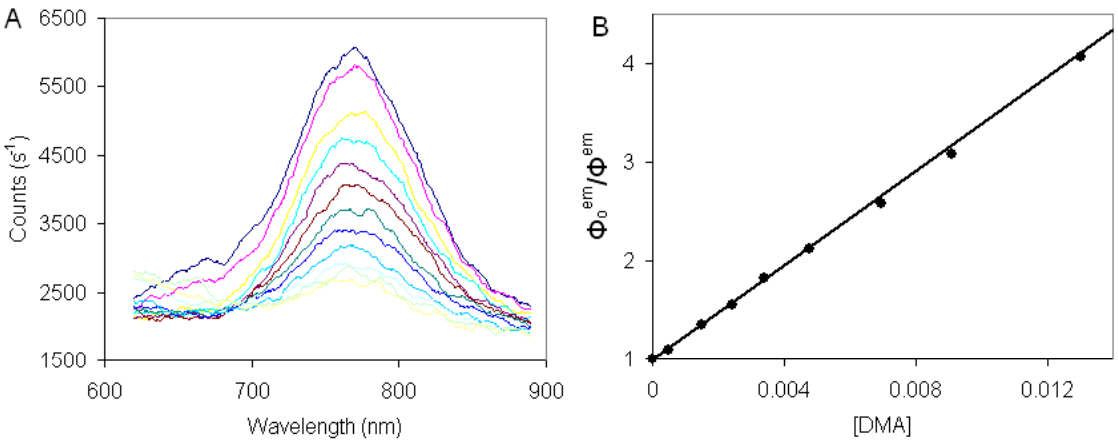

Figure 55. A) Emission spectrum for the complex $[\{(bpy)_2Ru(dpp)\}_2RhCl_2]^{5+}$ (bpy = 2,2'-bipyridine; dpp = 2,3-bis(2-pyridyl)pyrazine) displaying quenching with varying concentrations of the electron donor phenothiazine. B) Plot of the degree of quenching versus electron donor concentration.

$$\Phi_o^{em}/\Phi^{em} = 1 + (k_q + k_2)[\text{phenothiazine}]/\{(k_1 + k_{et}\}. \qquad \text{(eq27)}$$

which is similar to equation 16, except for replacing [DMA] with [phenothiazine]. The increase in driving force for quenching of the ^{3}MLCT state with phenothiazine as compared to quenching of the ^{3}MLCT state with DMA, a difference of 0.28 V, is accompanied by an increase in the rate constant of bimolecular deactivation, $k_q + k_2$. The slope of the Stern-Volmer plot (using $k_1 = k_r + k_{nr} = 1.2 \times 10^8$ s^{-1}) yields $k_q + k_2 = 2.9 \times 10^{10}$ M^{-1} s^{-1}, an increase of approximately 30% relative to the rate constant of bimolecular deactivation of the ^{3}MLCT state with DMA. This is indicative of a correlation between driving force and the rate of reductive quenching as expected. The increase in rate of quenching is in line with the increase in the rate of quenching for $[Ru(bpy)_3]^{2+}$ when similar increases in driving force were applied.[71]

Constant photolysis of the complex $[\{(bpy)_2Ru(dpp)\}_2RhCl_2](PF_6)_5$ in the presence of the electron donor phenothiazine for 20 minutes resulted in no spectroscopically detectable accumulation of the reduced complex

$[\{(bpy)_2Ru(dpp)\}_2Rh^I]^{5+}$. Emission quenching experiments have shown that phenothiazine efficiently quenches the ^{3}MLCT state so the absence of any accumulated photoreduced product can be attributed to efficient back electron transfer to the oxidized phenothiazine, a good electron acceptor. The oxidation products of phenothiazine have been previously been studied.[77] In the case of the anodic oxidation of phenothiazine, it was found that under conditions where the pH was greater than three the phenothiazine radical cation was stable. Photolysis of $[\{(bpy)_2Ru(dpp)\}_2Rh^{III}Cl_2]^{5+}$ in the presence of oxidized phenothiazine results in back electron transfer with no detectable accumulation of the catalytically active species $[\{(bpy)_2Ru(dpp)\}_2Rh^I]^{5+}$. This result was not unexpected and although this electron donor does not result in the formation of the reduced trimetallic complex, the emission quenching analysis can still contribute to the understanding of the system.

The above kinetic analysis focused on the photochemical process that results in the Rh^{II} product as an intermediate to the formation of the Rh^I product that can be monitored spectroscopically. Mechanistically the formation of the Rh^I product can take place via a second photochemical process akin to the formation of the Rh^{II} product, shown as 1 in Figure 56. A chemical process, disproportionation, can also take place resulting in the Rh^I and Rh^{III} species, shown as 2 in Figure 56. The complexity of the resulting proposed mechanism makes a full kinetic analysis difficult.

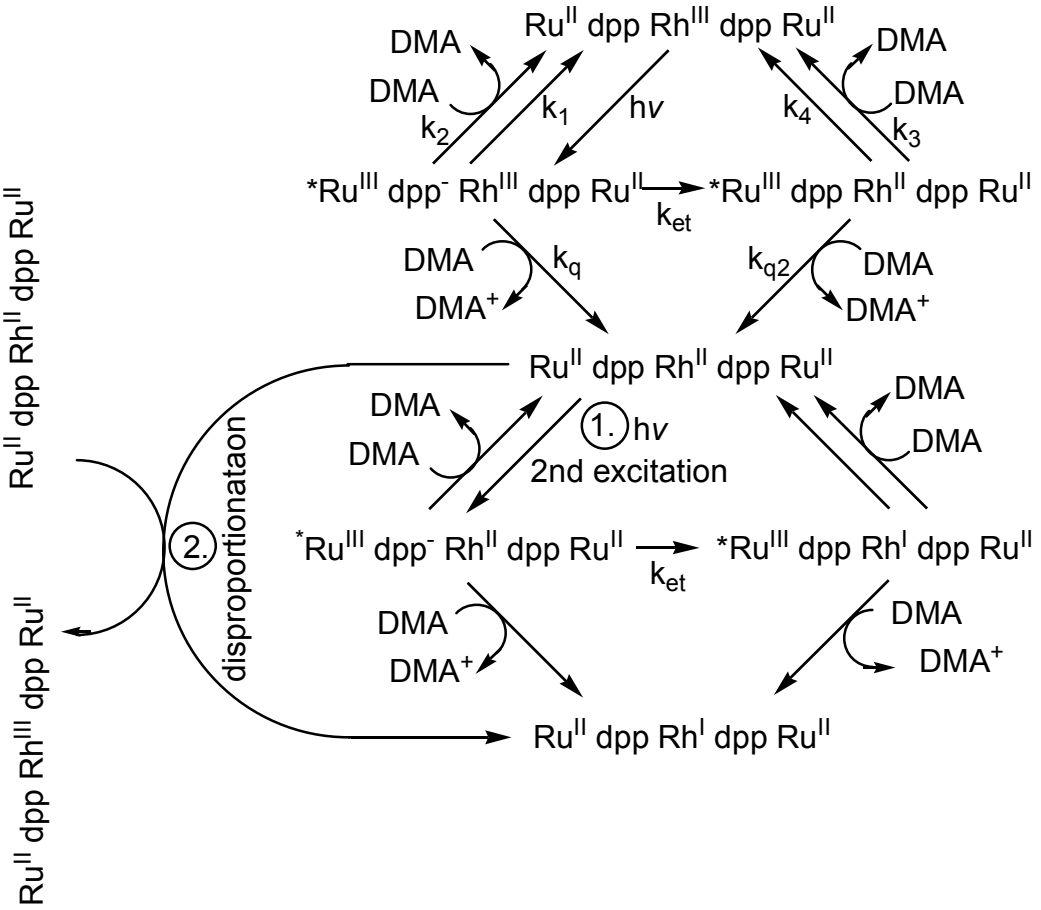

Figure 56. Proposed mechanism for photoinitiated electron transfer. bpy, Cl, and charges are omitted for clarity. $Ru^{II}dppRh^{III}dppRu^{II}$ is $[\{(bpy)_2Ru(dpp)\}_2RhCl_2]^{5+}$ where bpy = 2,2'-bipyridine and dpp = 2,3-bis-2-pyridylpyrazine. DMA is dimethylaniline. k_1 and k_4 are the unimolecular decay pathways from the ^{3}MLCT and ^{3}MMCT states, respectively, whereas k_2 and k_3 are the bimolecular deactivation rates from the same states. k_{et} is the rate of electron transfer to generate the ^{3}MMCT state. k_q and k_{q2} are the rates of reductive quenching by DMA to generate the Rh^{II} complex from the ^{3}MLCT and ^{3}MMCT states, respectively. This mechanism includes proposed paths for the formation of the two electron reduced rhodium(I) product which can occur through a second photoinitiated process (1), or can be formed through a disproportionation reaction (2).

I. Rh Centered Supramolecular Complex as a Photocatalyst for H_2 Production

1. Introduction for Hydrogen Photocatalysis

One potential application for a photoinitiated electron collector is photocatalytic hydrogen production from water. A light to energy conversion scheme involving the production of H_2 from water must utilize multi-electron catalysis to minimize the necessary driving force. The solar spectrum that reaches the earth's surface is composed primarily of visible light. The multielectron splitting of water can proceed with a low driving force, 1.23 eV, enabling the possibility of a visible light driven process. A single electron water splitting reaction requires a 5 eV driving force where very little radiation of that energy reaches the earths surface.

The Rh centered supramolecular complexes are a new class of photoinitiated electron collectors that collect reducing equivalents on the Rh metal center. Following electron collection, the supramolecular assembly remains intact. This is an unprecedented result in the literature and makes these complexes applicable as photocatalysts for multi-electron reactions like the reduction of water to hydrogen. When water is added to the photolysis of $[\{(bpy)_2Ru(dpp)\}_2RhCl_2](PF_6)_5$ in CH_3CN solution in the presence of DMA, spectroscopically the production of the Rh^I form of the complex, $[\{(bpy)_2Ru(dpp)\}_2Rh^I]^{5+}$, is observed, Figure 57. Subsequently, H_2 evolution is observed via headspace analysis by gas chromatography.

The analysis of the H_2 production for the complex $[\{(bpy)_2Ru(dpp)\}_2RhCl_2](PF_6)_5$ in CH_3CN/H_2O solution in the presence of the electron donor DMA has been investigated using an LED photolysis system that has previously been evaluated for power output stability.[62] The photolysis uses an optimized LED array described in the experimental

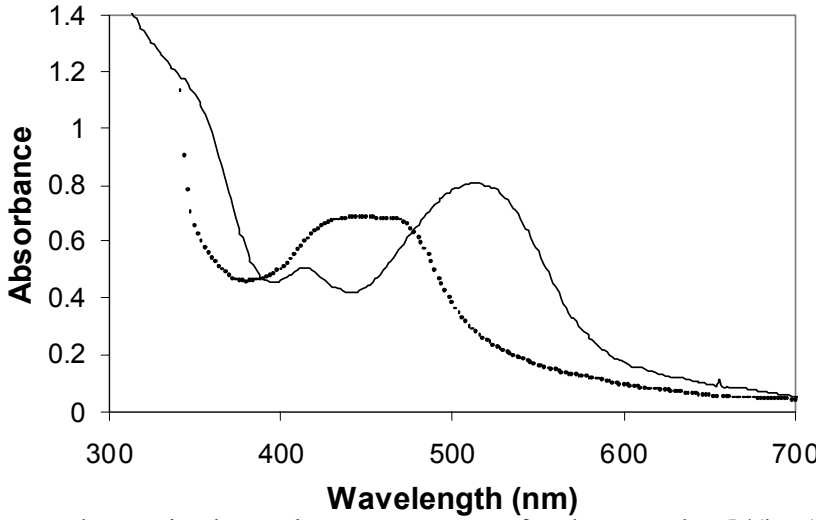

Figure 57. Electronic absorption spectroscopy for the complex $[\{(bpy)_2Ru(dpp)\}_2Rh^I]^{5+}$ (bpy = 2,2'-bipyridine; dpp = 2,3-bis(2-pyridyl)pyrazine), showing the complex before photolysis and the production of the Rh^I form of the complex (dotted line) during a hydrogen photocatalysis experiment.

section using multiple LEDs wired in series with power control for each LED to maintain a reproducible light delivery. The statistical analysis shows that the LEDs function well with this wiring method as light sources for this photochemistry. The variation between LEDs is not statistically different and it is possible to use each LED as an independent light source for H_2 production photochemistry. Light flux from the LED array using 470 nm LEDs was determined by chemical actinometry to be 9.26×10^{18} photons min^{-1}.

2. Hydrogen Production as a Function of Time

The production of H_2 by the photocatalyst $[\{(bpy)_2Ru(dpp)\}_2RhCl_2](PF_6)_5$ in CH_3CN/H_2O solution with dimethylaniline as the electron donor was measured as a function of photolysis time. Eight cells were prepared by adding 1.5 mL of a stock solution of 1.8×10^{-4} M $[\{(bpy)_2Ru(dpp)\}_2RhCl_2](PF_6)_5$, 2.09 mL of CH_3CN, and 0.05 mL of H_2O to each cell. The water added was acidified using triflic acid and adjusted to

pH 2.0. It should be noted that the final solutions were basic due to the high concentration of DMA, which is discussed in detail later. These solutions were sealed with a septum screw top and degassed for 10 min while sonicated to assist degassing. A stock solution of concentrated DMA was also degassed and sonicated for 30 min. Following sonication, 0.82 mL of DMA was added to each cell bringing all solutions to their final concentrations. The solution concentrations consisted of 0.065 mM $[\{(bpy)_2Ru(dpp)\}_2RhCl_2](PF_6)_5$ with 0.62 M H_2O, 1.5 M DMA, and 0.11 mM triflate. All eight cells were placed in the photolysis wells where photolysis was initiated. Two cells were removed upon 1 hour of total photolysis time and analyzed for gaseous content, followed by an additional hour for cells 3 and 4, two additional hours for cells 5 and 6, and 3 additional hours for the final two cells. The headspaces of each cell were analyzed by gas chromatography. A sample gas chromatogram is shown in Figure 58. After 1 hour of photolysis it was determined that 2.4 μmol of H_2 was present in the headspace, followed by 4.7 ± 0.7 μmol of H_2 after 2 hours, 6.3 ± 0.3 μmol of H_2 after 3

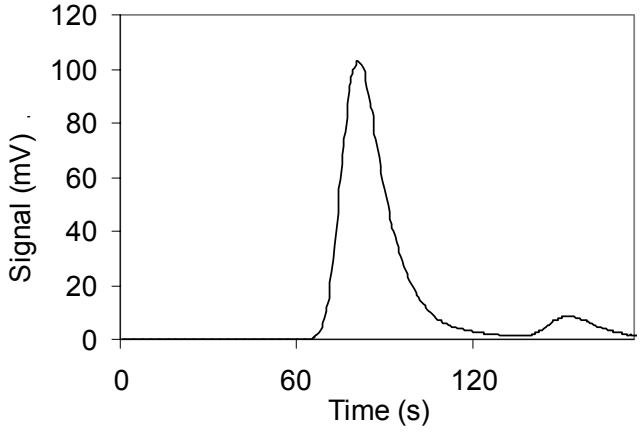

Figure 58. Sample gas chromatogram for a hydrogen generation experiment showing the elution first of hydrogen followed by a small tail of nitrogen and lastly a small peak consisting of oxygen. For this individual measurement the peak corresponding to hydrogen was integrated from 62 s to 112 s to avoid integration of the tailing nitrogen peak.

hours and 8.2 ± 0.3 μmol of H_2 after 4 hours. The solution was also evaluated in terms of dissolved hydrogen. Dissolved hydrogen was calculated using Henry's Law (eq28).[51]

$$p_B = x_B K_B \quad \text{(eq28)}$$

p_B is the partial pressure of hydrogen, K_B is Henry's law constant (for hydrogen is 5.34 x 10^7 K/Torr)[51], χ_B is the mole fraction of hydrogen in the photolysis cell solution. The saturated mole fraction for hydrogen in acetonitrile is 1.78 x 10^{-4}.[78] The partial pressures of hydrogen was calculated for each cell from which the mole fraction and moles of hydrogen were determined. Dissolved hydrogen typically resulted in an additional 22% to 23% of the overall hydrogen content per cell. Dissolved hydrogen calculated for each hour resulted in an additional 0.7 μmol of H_2 after one hour of photolysis, 1.3 μmol of H_2 after two hours of photolysis, 1.7 μmol of H_2 after three hours of photolysis, and an additional 2.0 μmol of H_2 after 4 hours of photolysis. This brings the total μmol of H_2 produced for each time period to 3.10 ± 0.01 after 1 hour, 6.1 ± 0.8 after 2 hours, 8.0 ± 0.4 after 3 hours, and 10.4 ± 0.6 after 4 hours of photolysis. Figure 59 shows the total quantities of H_2 produced in μmol determined, from headspaces and dissolved hydrogen, for this time based experiment. The figure shows the photocatalyst produces H_2 linearly with time with no drop in quantum yield over the measured period of time. This data suggests the catalyst is relatively stable over a period of 4 hours. The hydrogen produced does not appear to mirror the formation of the rhodium(I) species as formation of the rhodium(I) species is essentially complete after 15 minutes of photolysis while hydrogen production appears to be slower initially and continues throughout the time measured.

Additional experiments were performed varying the concentrations of water, electron donor, and metal complex to probe the impact of various factors on H_2

production. A summary of all experimental results is shown at the end of this section in Table 4. The experimental design for all three experiments sets the standard conditions for the final concentrations as 0.061 mM $[\{(bpy)_2Ru(dpp)\}_2RhCl_2](PF_6)_5$, 0.62 M H_2O, 1.5 M DMA, and 0.11 mM triflate. The standard photolysis time was 2 hours.

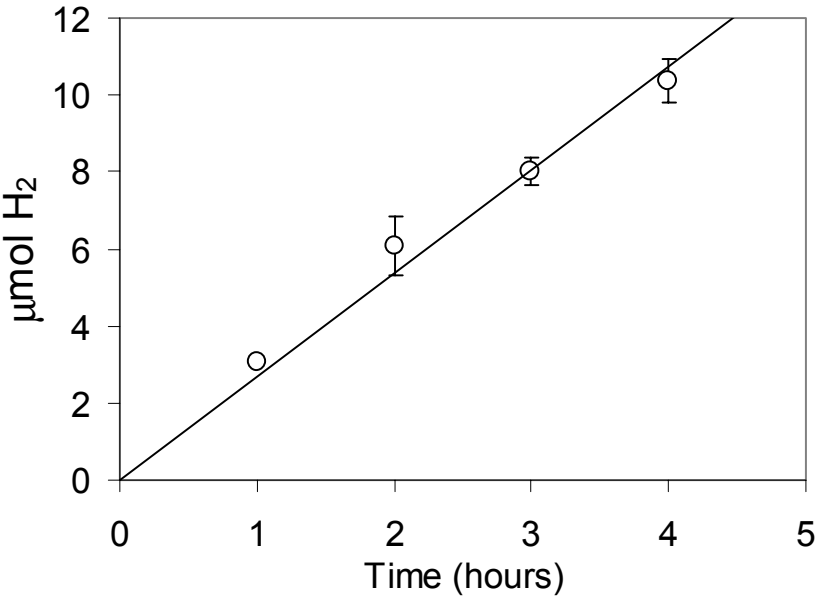

Figure 59. µmol of hydrogen produced as a function of photolysis time using 0.065 mM $[\{(bpy)_2Ru(dpp)\}_2RhCl_2](PF_6)_5$ (bpy = 2,2'-bipyridine; dpp = 2,3-bis(2-pyridyl)pyrazine), the trimetallic photocatalyst, 0.62 M water, 0.11 mM triflate, and 1.5 M dimethylaniline, the electron donor.

3. Impact of Metal Complex Concentration on Hydrogen Production

Varying the metal complex concentration could potentially have an impact on hydrogen production through multiple avenues. The metal complex $[\{(bpy)_2Ru(dpp)\}_2RhCl_2](PF_6)_5$, is a photocatalyst, meaning it uses light to perform a catalytic function, i.e. the reduction of water to generate H_2. Since the catalytic process is dependent on light, the total amount of light absorbed by the system will have an impact on hydrogen production. Varying the absorbance of the solution, therefore, should have a

noticeable impact on hydrogen generation until >99% of the incident radiation is absorbed upon which there should be no noticeable impact on hydrogen generation as a result of light absorbed. Varying the metal complex concentration could potentially have another impact on hydrogen production. If hydrogen production involves a bimolecular pathway, an increase in the metal complex concentration should result in an increase in the rate of hydrogen formation. This possibility can be explored by varying the metal complex concentration in the range such that >99% of the light is absorbed, so that any impact on hydrogen production is not a result of light absorbed, rather the impact would be a result of an operable bimolecular pathway for hydrogen production.

Preparation of the "varying metal complex concentration" experiment was a collaborative effort with Shamindri Arachchige, and is detailed as follows. Four cells were prepared by adding varying amounts of a stock solution of 8.6×10^{-5} M $[\{(bpy)_2Ru(dpp)\}_2RhCl_2](PF_6)_5$, prepared spectroscopically using Beer's Law. The absorbance of the stock solution of metal complex prepared was 0.45 at 518 nm in a 0.20 cm cell. The stock solution (2.86 mL) was added to cells one and two, and 3.59 mL were added to cells three and four. CH_3CN (0.73 mL) was also added to cells one and two to make the volume for all four cells equivalent. 0.05 mL of acidified H_2O was then added to each cell. The water added was adjusted to pH 2.0 using triflic acid. The cells were sealed with a screw top septum and degassed and sonicated for 10 min. A stock solution of concentrated DMA was also degassed and sonicated for 30 min. Following sonication, 0.82 mL of DMA was added to each cell bringing all solutions to their final concentrations. The final metal complex concentration for cells one and two was of 0.055 mM and cells three and four was 0.069 mM. The metal complex concentration was

varied such that all of the available light was absorbed in each cell. All four cells also had 0.62 M H_2O, 1.5 M DMA, and 0.11 mM triflate. All four cells were placed in the photolysis wells and irradiated with 470 nm light for 2 hours. The headspaces were analyzed by gas chromatography. Dissolved hydrogen was calculated as above. Figure 60 shows the total quantities (headspace and dissolved) of H_2 produced in µmol with varying metal complex concentration. A 0.055 mM solution of $[\{(bpy)_2Ru(dpp)\}_2RhCl_2](PF_6)_5$ yielded 5.8 ± 1.3 µmol of H_2 (including dissolved hydrogen). A 0.065 mM solution of $[\{(bpy)_2Ru(dpp)\}_2RhCl_2](PF_6)_5$ yielded 6.1 ± 0.8 µmol of H_2 (data point from 2 hours of photolysis from "vary time" experiment; 0.62 M H_2O, 1.5 M DMA, 0.11 mM triflic acid). Finally a 0.069 mM solution of $[\{(bpy)_2Ru(dpp)\}_2RhCl_2](PF_6)_5$ yielded 6.0 ± 1.3 µmol of H_2. The data indicates that varying the metal complex concentration in the range where all of the light is absorbed had little or no impact on hydrogen generation lending support to a unimolecular

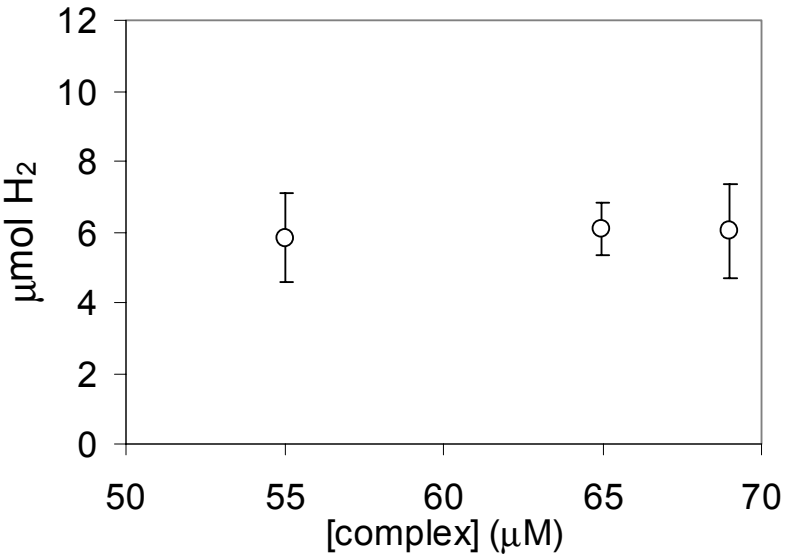

Figure 60. µmol of hydrogen produced as a function of metal complex concentration using $[\{(bpy)_2Ru(dpp)\}_2RhCl_2](PF_6)_5$ (bpy = 2,2'-bipyridine; dpp = 2,3-bis(2-pyridyl)pyrazine), the trimetallic photocatalyst, 0.62 M water, 0.11 mM triflate, and 1.5 M dimethylaniline, the electron donor.

hydrogen production mechanism. An expansion of this study may be necessary to rule out an operable bimolecular pathway for the formation of hydrogen since the concentration range probed was small. The mechanism for hydrogen production is discussed in more detail in section VIII. I. 7.

4. Impact of Electron Donor Concentration on Hydrogen Production

The impact of electron donor concentration on hydrogen photocatalysis was also studied in a systematic fashion, which was a collaborative effort with Shamindri Arachchige. From the Stern-Volmer analysis, dynamic quenching was observed suggesting the rate of hydrogen production could vary with the electron donor concentration. Eight cells were prepared by adding 3.14 mL of a stock solution of 8.6 x 10^{-5} M $[\{(bpy)_2Ru(dpp)\}_2RhCl_2](PF_6)_5$, prepared spectroscopically for determination of the concentration. The absorbance of the stock solution of metal complex was 0.45 using a 0.20 cm path length cell. 1.07 mL of CH_3CN was added to cells one and two, 0.86 mL of CH_3CN was added to cells three and four, and 0.45 mL of CH_3CN was added to cells five and six. No additional CH_3CN was added to cells seven and eight. 0.05 mL of acidified H_2O was added adjusted to pH 2.0 using triflic acid. The cells were sealed with a screw top septum and degassed and sonicated for 10 min. A stock solution of concentrated DMA was also degassed and sonicated for 30 min. Following sonication, 0.20 mL of DMA was added to cells one and two, 0.41 mL of DMA was added to cells three and four, 0.82 mL of DMA was added to cells five and six, and 1.27 mL of DMA was added to cells seven and eight, bringing all solutions to their final concentrations. The final DMA concentration for cells one and two was 0.35 M, cells three and four was

0.72 M, cells five and six was 1.5 M, cells seven and eight was 2.2 M. All eight cells also had 0.061 mM $[\{(bpy)_2Ru(dpp)\}_2RhCl_2](PF_6)_5$, 0.62 M H_2O, and 0.11 mM triflate. All eight cells were placed in the photolysis wells and irradiated with 470 nm light for 2 hours. Following photolysis the headspaces were analyzed by gas chromatography. Figure 61 shows the quantities of H_2 produced including dissolved hydrogen in µmol with varying electron donor concentrations. 0.35 M DMA resulted in 0.4 ± 0.1 µmol of H_2, while 0.72 M DMA resulted in 1.6 ± 0.4 µmol of H_2. 1.5 M DMA resulted in 7.6 ± 1.3 µmol of H_2, and 2.2 M DMA resulted in 10.6 ± 1.3 µmol of H_2. Using 2.2 M DMA resulted in the highest quantum yield, 0.012 , of any hydrogen photocatalysis experiment and the highest turnover of 39. The data indicates there is a strong dependency on electron donor concentration for hydrogen generation as evident by the large increase in hydrogen produced at higher DMA concentrations. This indicates that quenching of the ^{3}MLCT or ^{3}MMCT state by DMA is involved before or during the rate limiting step for hydrogen generation.

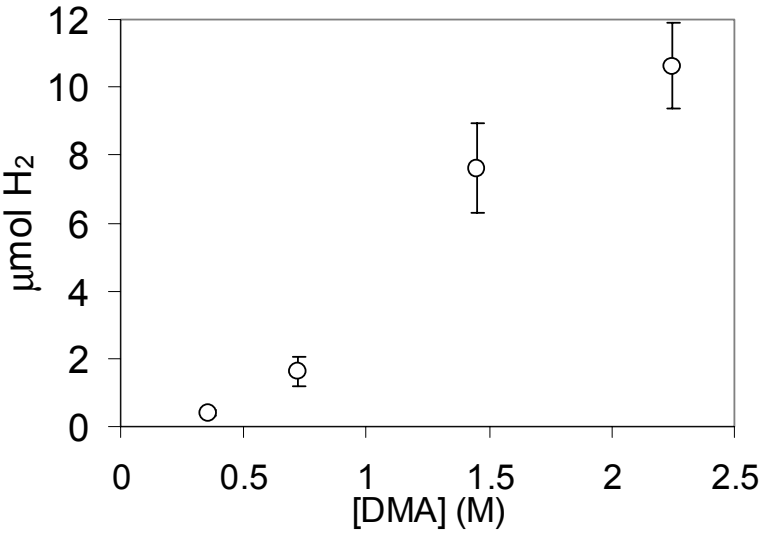

Figure 61. µmol of hydrogen produced as a function of electron donor concentration using 0.061 mM $[\{(bpy)_2Ru(dpp)\}_2RhCl_2](PF_6)_5$ (bpy = 2,2'bipyridine; dpp = 2,3-bis(2-pyridyl)pyrazine), the trimetallic photocatalyst, 0.62 M water, 0.11 mM triflate, with varying electron donor concentration.

5. Impact of Water Concentration on Hydrogen Production

Varying the water concentration was also studied to see what impact if any it has on the efficiency of hydrogen generation. Care must be taken as to not also vary the overall acidity/basicity of the final solutions since the water added is also a source of protons. Since the solution is primarily organic, CH_3CN, by definition pH is not directly relatable to this system since pH is the proton concentration in an aqueous system. Calculation of the solution "pH", however, can provide a rough idea as to the solution proton concentration. A rough calculation of pH can provide an estimation of protonation of the trimetallic complex, which could play a role in the mechanism for hydrogen production. The mechanism for hydrogen production will be discussed in more detail in section VIII. 7. Calculation of the pH for an aqueous system with 1.5 M DMA ($pK_B = 8.93$)[51] and 0.11 mM triflic acid results in a pH of approximately 9.0. Studies regarding the impact water concentration has on hydrogen production was a collaborative effort with Shamindri Arachchige.

The overall water concentration was varied from 0.062 M to 6.2 M. Four cells were prepared by first adding 3.14 mL of a stock solution of 8.6×10^{-5} M $[\{(bpy)_2Ru(dpp)\}_2RhCl_2](PF_6)_5$, prepared spectroscopically using Beer's Law to each cell. The absorbance of the stock solution of metal complex was 0.45 using a 0.20 cm path length cell. CH_3CN (0.495 mL) was also added to cells one and two to make the final volume for all four cells equivalent once water and DMA have been added. A solution of 0.1 M CF_3SO_3H was prepared (pH = 1) from which 5 μL was added to each of the four cells. 0.495 mL of deionized water was added to cells three and four. Despite the amount of acid added to each cell, due to the large concentration of DMA all

solutions are still basic. The cells were sealed with a screw top septum and degassed and sonicated for 10 min. A stock solution of concentrated DMA was also degassed and sonicated for 30 min. Following sonication, 0.82 mL of DMA was added to each cell bringing all solutions to their final concentrations. All four cells had 0.061 mM $[\{(bpy)_2Ru(dpp)\}_2RhCl_2](PF_6)_5$, and 1.5 M DMA. Cells one and two had 0.062 M H_2O while cells three and four had 6.2 M H_2O, however the triflic acid concentration for all four cells was equivalent. All four cells were placed in the photolysis wells and irradiated with 470 nm light for 2 hours. Following photolysis the headspaces were analyzed by gas chromatography. Figure 62 shows the quantities of H_2 produced in µmol including dissolved hydrogen with the two different water concentrations. It was found that 0.062 M water resulted in 6.6 ± 1.1 µmol of H_2, 0.62 M water resulted in 6.1 ± 0.8 µmol of H_2 (data point from 2 hours of photolysis from "vary time" experiment; 0.061 mM $[\{(bpy)_2Ru(dpp)\}_2RhCl_2](PF_6)_5$, 1.5 M DMA, 0.11 mM triflic acid), and 6.2 M

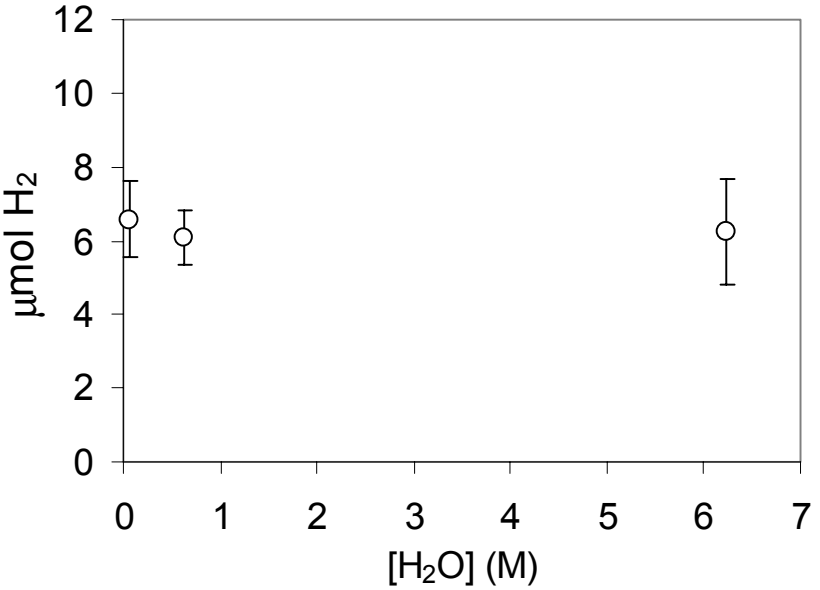

Figure 62. µmol of hydrogen produced as a function of water concentration using 0.065 mM $[\{(bpy)_2Ru(dpp)\}_2RhCl_2](PF_6)_5$ (bpy = 2,2'-bipyridine; dpp = 2,3-bis(2-pyridyl)pyrazine), the trimetallic photocatalyst, 0.11 M triflate, and 1.5 M dimethylaniline, the electron donor, and varying water concentration.

water resulted in 6.2 ± 1.4 μmol of H_2. It appears from these results that water concentration does not greatly impact the generation of hydrogen as the amount of variation is within experimental error. Even at low water concentrations there is still a large excess of water. The experimental conditions could be such that any change in water concentration does not impact the rate determining step.

6. Impact of Acid Counterion on Hydrogen Production

The impact of the acid counterion was also studied by using HCl and CF_3SO_3H as a source of protons. The experimental design consisted of the following. A stock solution of 1.8 x 10^{-4} M $[\{(bpy)_2Ru(dpp)\}_2RhCl_2](PF_6)_5$ was prepared spectroscopically. The absorbance of the stock solution of metal complex was 0.95 using a 0.20 cm path length cell. 1.5 mL of the metal complex stock solution was added to each of the six cells followed by 2.09 mL of CH_3CN. Two aqueous acid stock solutions were prepared, one from hydrochloric acid and the other from triflic acid. Each of the acid solutions were adjusted to pH 2.0 using the respective acid. 0.050 mL of the aqueous HCl solution, pH 2.0, was added to cell one, two, and three, and 0.050 mL of aqueous triflic acid, pH = 2.0, was added to cells four, five, and six. The cells were then sealed with a screw top septum and degassed and sonicated for 10 min. A stock solution of concentrated DMA was also degassed and sonicated for 30 min. Following sonication, 0.82 mL of DMA was added to each cell bringing all solutions to their final concentrations. The solution concentrations consisted of 0.065 mM $[\{(bpy)_2Ru(dpp)\}_2RhCl_2](PF_6)_5$ with 0.62 M H_2O, 1.5 M DMA, and 0.11 mM chloride/triflate. All six cells were placed in the photolysis wells and photolysis was initiated. After 2 hours of photolysis the headspaces were

analyzed by gas chromatography. The headspace analysis resulted in an average of 3.4 ± 0.7 μmol of H_2 when HCl was used as the proton source, while 4.7 ± 0.2 μmol of H_2 was produced when triflic acid was used as the proton source. Once dissolved hydrogen had been accounted for the total quantities of hydrogen produced were 4.3 ± 0.9 μmol of H_2 when HCl was used, and 5.9 ± 0.3 μmol of H_2 was produced when triflic acid was used as the proton source. From this analysis it is apparent that the use of HCl inhibits the production of hydrogen relative to triflic acid and that Cl^- is in some way inhibiting the reaction. Examination of the initial photoreduction can provide a possible explanation. Following the two electron reduction of the rhodium core, two chloride anions are lost in the process of generating the d^8 square planar complex. The presence of additional chloride anions in solution may inhibit the formation of the catalytically active rhodium(I) form of the trimetallic complex by allowing back electron transfer to generate the original rhodium(III) complex $[\{(bpy)_2Ru(dpp)\}_2Rh^{III}Cl_2](PF_6)_5$. Another possibility to consider is that Cl^- could preferentially bind to any catalytically active species instead of water, which would impair catalysis.

Table 4 summarizes the results for all of the hydrogen photocatalysis experiments. Complex concentration, DMA concentration, water concentration, and photolysis time were all probed with respect to μmol of H_2 produced, turnover, and quantum yield. Each variable that is probed is highlighted in blue. The summary of results show the impact photolysis time has on the hydrogen production while the quantum yield remains relatively steady over the course of the experiment. The electron donor concentration was also found to have a large impact on the hydrogen produced with the highest quantum yield for any experiment resulting from the highest DMA concentration. The

metal complex concentration and water concentration was not found to impact the rate determining step of hydrogen production.

Table 4. Summary of photocatalysis experiments for H_2 production using the supramolecular catalyst $[\{(bpy)_2Ru(dpp)\}_2RhCl_2](PF_6)_5$ (bpy = 2,2'-bipyridine; dpp = 2,3-bis(2-pyridyl)pyrazine).

[Complex] (μM)	[DMA] (M)	$[H_2O]$ (M)[a]	photolysis time (hr)	H_2 (μ mol)	turnover	Φ_{H2}[d] x 10^{-3}
65	1.5	0.62	1	3.1	11	6.7
65	1.5	0.62	2	6.1	23	6.6
65	1.5	0.62	3	8.0	30	5.8
65	1.5	0.62	4	10.4	39	5.6
55	1.5	0.62	2	5.8	21	6.3
69	1.5	0.62	2	6.0	22	6.5
65	1.5	0.62 (HCl)[b]	2	4.3	16	4.7
61	0.35	0.62	2	0.4	1.5	0.4
61	0.72	0.62	2	1.6	5.9	1.7
61	2.2	0.62	2	10.6	39	11.5
61	1.5	0.062[c]	2	6.6	24	7.2
61	1.5	6.2[d]	2	6.2	23	6.7

[a] M of H_2O in final photolysis solution. pH of H_2O added was adjusted to 2.0 with HCF_3SO_3.
[b] pH of H_2O adjusted to 2.0 with HCl
[c] pH of H_2O added was adjusted to 3.0 with HCF_3SO_3
[d] ϕ_{H2} = (mol H_2 x 2) / (mol photons)

7. Electrochemistry in the presence of H_2O

Electrochemistry can be used to probe the catalytic behavior of the complex $[\{(bpy)_2Ru(dpp)\}_2RhCl_2](PF_6)_5$. Squarewave voltammetry for the trimetallic complex was performed both in the absence and in the presence of water to probe any possible electrocatalytic behavior. It should also be noted that the reduction of H^+ by one electron (rxn42), is pH dependent, and thus the reduction of H_2O to form H_2 and OH^- (rxn43). By using the Nernst equation (eq29)[80] and the known standard reduction

$$2\ H^+ + 2e^- \rightleftharpoons H_2 \qquad \text{(rxn42)}$$

$$2\ H_2O + 2e^- \rightleftharpoons H_2 + 2\ OH^- \qquad \text{(rxn43)}$$

$$E = E° - \frac{2.303\ RT}{nF} \times \log Q \qquad \text{(eq29)}$$

potentials, E°, the potential can be calculated for nonstandard conditions, E, i.e. at varying pHs, and thus the pH dependence can be determined. R is the gas constant (8.314 $J \cdot K^{-1} \cdot mol^{-1}$),[22] T is temperature in K, *n* is the number of electrons, F is Faraday's constant (96,485 $C \cdot mol^{-1}$),[22] and Q is the reaction quotient of [product] / [reactant]. The standard conditions for E° are 1 M for ions and 1 atmosphere for gases. For reaction 42, E° = 0 V,[80] which is also the normal hydrogen reference electrode, and for reaction 43, E° = -0.828 V.[80] At pH 9 the reduction potential for reactions 42 and 43 is -0.53 V vs. NHE or -0.82 V vs. Ag/AgCl. As the solution becomes more basic, larger potentials are needed to provide a thermodynamic driving force for generating H_2. The reductive region of the square wave voltammogram is shown in Figure 63. A $Rh^{I/II/III}$ reduction is observed followed by two $dpp^{0/-}$ reductions. Upon the addition of 0.62 M H_2O no change

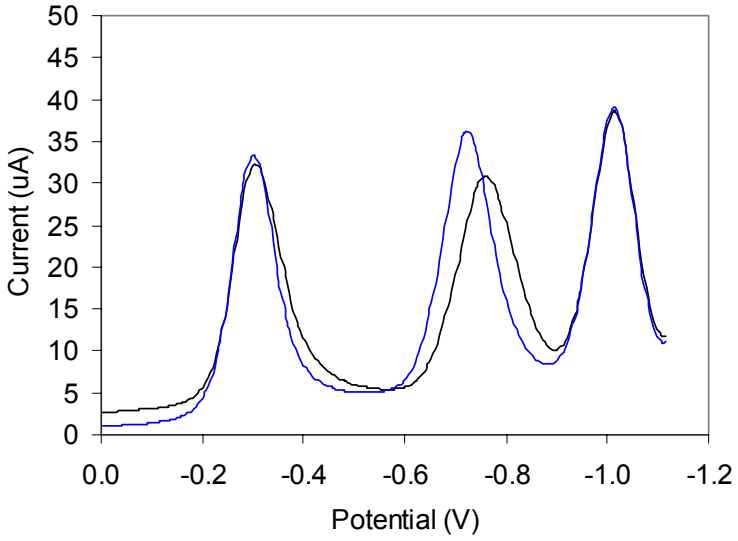

Figure 63. Squarewave voltammogram for the complex $[\{(bpy)_2Ru(dpp)\}_2RhCl_2](PF_6)_5$ (bpy = 2,2'-bipyridine; dpp = 2,3-bis(2-pyridyl)pyrazine) in the absence (black) and in the presence of 0.62 M H_2O. The reductive region is shown displaying a rhodium reduction followed by two dpp reductions. A small increase in current is observed for the first $dpp^{0/-}$ reduction upon the addition of water, which could be a result of electrocatalysis of H_2O to generate H_2.

is observed in the peak potentials or the oxidative electrochemistry. The second $dpp^{0/-}$ reduction, however, displays an enhancement in the current upon H_2O addition. This would be consistent with the electrogenerated $[(bpy)_2Ru^{II}(dpp^{-})Rh^{I}(dpp)Ru^{II}(bpy)_2]^{4+}$ reduced form of the complex being a catalyst for H_2O reduction.

8. Proposed Mechanism for Hydrogen Production

A basic understanding of how hydrogen is catalytically generated from water is necessary for future work involving system modifications like converting to an aqueous medium, complex component modifications, and the eventual tethering of the complex to an electroactive surface. The trimetallic complex $[\{(bpy)_2Ru(dpp)\}_2Rh^{III}Cl_2]^{5+}$ has been shown to undergo photoinitiated electron collection resulting in the doubly reduced rhodium(I) d^8 square planar complex $[\{(bpy)_2Ru(dpp)\}_2Rh^{I}]^{5+}$ along with the loss of two chlorides, Figure 39. The unsaturated coordination environment can facilitate the coordination of a substrate potentially leading to a catalytic reaction. The d^8 pseudo-square planar rhodium complex, $[(bpy)_2Rh^{I}]^{+}$, will be used as a model for the construction of a mechanism for hydrogen catalysis for the trimetallic complex due to the similarities between the rhodium core and the rhodium monometallic complex and due to the availability of data. It should be noted, however, that structural and electronic differences arise from substituting two bpys with two dpp bound LAs. Structurally, this substitution can result in steric constraints which can impede the formation of certain substrate bound intermediates and/or dimerization. These steric constraints are discussed below in more detail. It should also be noted that two bpys bound to rhodium(I) result in a different electronic environment than two dpp bound LAs most notably due to the

presence of two pyrazine components versus pyridines. Two pyrazines result in a shift of electronic density from the rhodium core to the dpp bridges relative to the bpy bound rhodium complex. With a second metal bound to dpp this electron withdrawing effect is even more pronounced. This results in a rhodium(I) trimetallic complex that is a poorer Lewis base as it is less able to donate a pair of electrons to a Lewis acid, i.e. a proton, resulting in lower pK_as relative to those reported for $[(bpy)_2Rh^I]^+$.

The speciation of $[(bpy)_2Rh^I]^+$ has been studied in an aqueous environment with respect to pH. It was determined that several forms of the complex exist at varying pHs. pKs were determined for the following equilibria

$$2\,[(bpy)_2Rh^I]^+ \rightleftharpoons [(bpy)_2Rh^I]_2^{2+} \qquad \text{(rxn44)}$$

$$[(bpy)_2Rh^I]^+ + H_3O^+ \rightleftharpoons [(bpy)_2Rh^{III}(H)(OH_2)]^{2+} \qquad \text{(rxn45)}$$

$$[(bpy)_2Rh^I]_2^{2+} + H^+ \rightleftharpoons [\{(bpy)_2Rh^I\}_2(H)]^{3+} \qquad \text{(rxn46)}$$

where the pK for reaction 44 is 4.0 ± 0.2, the pK_b for reaction 45 is 6.7 ± 0.1, and the pK_b for reaction 46 is 4.7 ± 0.3.[80] pKs were determined spectroscopically for reactions 44 and 45 by monitoring the disappearance of the Rh → bpy CT transition. The pK_b was determined for reaction 46 by monitoring the spectroscopy of the formation the protonated dimer, a brown colored complex. $[(bpy)_2Rh^I]^+$ can serve as a good model for reactivity for the photochemically or electrochemically reduced trimetallic complex $[\{(bpy)_2Ru(dpp)\}_2Rh^I]^{5+}$ since the coordination environment for rhodium(I) in both systems is very similar.

Reactions 44 and 46 involve the formation of a rhodium(I)-rhodium(I) dimer, an unlikely reaction in the case of the trimetallic complex considering the bulky nature of the light absorbers attached via the bridging dpp ligands. The rhodium(I) dimer, as

shown by Creutz, can also be protonated more easily than the rhodium(I) mononuclear complex. The formation of the protonated dimer would lead to the halting of the catalytic cycle since one of the coordination sites in no longer available. The rhodium(I)-rhodium(I) distance for the closest approach can be estimated using CAChe, which can indicate whether a rhodium-rhodium bond is possible. The CAChe generated structures show the minimum distance between the pseudo square planar rhodium centers is approximately 5 Å, whereas a typical rhodium-rhodium bond ranges from 2.4 to 2.8 Å,[46] making any direct rhodium-rhodium bound dimerization an unlikely occurrence, Figure 64. Oishi has shown the catalytic production of H_2 through a bimolecular process as shown in reaction 47.[57]

$$2[Rh^{II}HCl(dpm)_3]^{3-} \rightarrow 2\ [Rh^{I}Cl(dpm)_3]^{3-} + H_2 \qquad \text{(rxn47)}$$

Rhodium-hydride bond lengths are typically 1.4 to 1.6 Å making the formation of a hydride bridged dimer unlikely as well.[81] There is additional evidence to support the lack

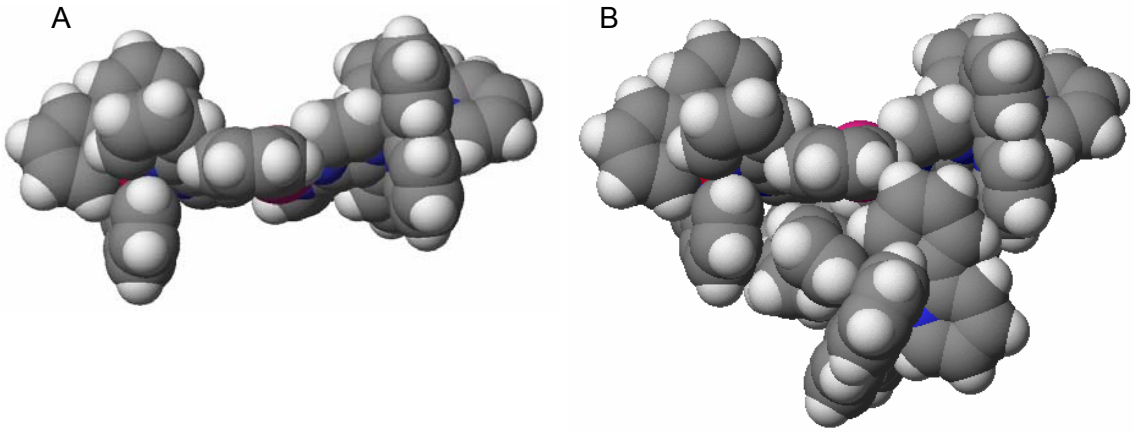

Figure 64. CAChe generated space filling models for A) the rhodium(I) centered complex $[\{(bpy)_2Ru(dpp)\}_2Rh^{I}]^{5+}$ (bpy = 2,2'-bipyridine; dpp = 2,3-bis(2-pyridyl)pyrazine) and B) two such complexes arranged for the closest rhodium-rhodium approach.

of formation of a rhodium(I) dimer with the trimetallic complex. Hydrogen photocatalysis experiments have shown that metal complex concentration has no impact on hydrogen production in the range in which all of the visible light is absorbed. Increasing the metal complex concentration should increase dimerization leading to a decrease in the production of hydrogen, however, since there is no observable impact of increasing the complex concentration, it is unlikely that dimerization occurs.

It is well known that transition metal coordination complexes that are coordinatively unsaturated can act as Lewis acids, i.e. electron donating ligands can coordinate to them. This is especially the case with electron deficient early transition metal complexes. Electron rich transition metal complexes like 16 and 18 e- complexes that have accessible electron pairs, however, can also act as Lewis bases. These metallic bases can be very basic and are especially reactive toward oxidative addition reactions, which have been studied in detail for decades. d^8 and d^{10} metals like Fe^0, Ru^0, Os^0, Rh^I, Ir^I, Ni^0, Pd^0, Pt^{II}, and Pt^0 are particularly reactive toward oxidative additions, which is a frequent mode for entering a catalytic cycle.[82] Protonation or oxidative addition of H_3O^+ or H_2O to the reduced rhodium(I) trimetallic complex is a possible first step in the mechanism for hydrogen production due to the basicity of the solution.

Determination of the solution "pH" can help probe possible hydrogen catalysis mechanisms which involve protonation of the photoreduced complex $[\{(bpy)_2Ru(dpp)\}_2Rh^I]^{5+}$. The reaction solution consists of a complex equilibrium of the dissociation water (rxn48), the dissociation of the strong acid CF_3SO_3H (rxn49), protonation of the electron donor DMA (rxn50), and protonation of the rhodium(I) complex $[\{(bpy)_2Ru(dpp)\}_2Rh^I]^{5+}$ by one proton (rxn51) and by a second proton (rxn52),

were solved using the Henderson-Hasselbalch equation (eq30) and a spreadsheet. A number of assumptions were made in the process.

$$H_2O \rightleftharpoons H^+ + OH^- \quad \text{(rxn48)}$$

$$CF_3SO_3H \rightleftharpoons H^+ + CF_3SO_3^- \quad \text{(rxn49)}$$

$$DMA + H_2O \rightleftharpoons HDMA^+ + OH^- \quad \text{(rxn50)}$$

$$[\{(bpy)_2Ru(dpp)\}_2Rh^I]^{5+} + H_3O^+ \rightleftharpoons [\{(bpy)_2Ru(dpp)\}_2Rh^{III}(H)(H_2O)]^{6+} \quad \text{(rxn51)}$$

$$[\{(bpy)_2Ru(dpp)\}_2Rh^{III}(H)(H_2O)]^{6+} + H_2O \rightleftharpoons [\{bpy)_2Ru(dpp)\}_2Rh^{III}(H)(H_3O)]^{7+} \quad \text{(rxn52)}$$

$$pH = pK_A + \log \frac{[base]}{[acid]} \quad \text{(eq30)}$$

Photocatalytic generation of hydrogen with the trimetallic complex currently takes place in acetonitrile using the electron donor dimethylaniline, which has a pK_b of 8.93.[51] Since the current system is nonaqueous, any pK_as and pK_bs determined for an aqueous system are not directly applicable, however, calculation of the pH for an aqueous system can provide an estimation of the extent of protonation for the reduced trimetallic complex $[\{(bpy)_2Ru(dpp)\}_2Rh^I]^{5+}$. Reaction 45 shows the protonation and coordination of H_2O to the complex $[(bpy)_2Rh^I]^+$, which has a pK_b of 6.7 ± 0.1. The resulting rhodium(III) complex, $[(bpy)_2Rh^{III}(H)(H_2O)]^{2+}$, has a reported pK_b of 4.5.[83] These two rhodium monometallic species will be used as a model for determining the pH of the solution and the extent of protonation for the trimetallic complex. A spreadsheet was used to calculate the pH and the concentrations of the species in solution including $[H^+]$, $[OH^-]$, $[HCF_3SO_3]$, $[CF_3SO_3^-]$, [DMA], $[HDMA^+]$, $[\{(bpy)_2Ru(dpp)\}_2Rh^I]^{5+}$, $[\{(bpy)_2Ru(dpp)\}_2Rh^{III}(H)(H_2O)]^{6+}$, and $[\{bpy)_2Ru(dpp)\}_2Rh^{III}(H)(H_3O)]^{7+}$ for an

aqueous system, with the reported Ks corrected for the actual water concentration which was 0.62 M. The initial concentrations of the species added were 0.061 mM $[\{(bpy)_2Ru(dpp)\}_2RhCl_2](PF_6)_5$, 1.5 M DMA and 0.11 mM triflic acid. The pH was determined to be approximately 9.0. The complex $[\{(bpy)_2Ru(dpp)\}_2Rh^{I}]^{5+}$ and the singly and doubly protonated forms were present in solution at 95.9%, 1.3% and 2.8% respectively. Protonation of the rhodium(I) trimetallic complex resulting in the complex $[\{(bpy)_2Ru(dpp)\}_2Rh^{III}(H)(H_2O)]^{6+}$, is shown as step 1 of Figure 65. The subsequent protonation to generate the complex $[\{(bpy)_2Ru(dpp)\}_2Rh^{III}(H)(H_3O)]^{7+}$ is shown as step 2 of Figure 65. After the second protonation, the proposed mechanism involves a photoinduced electron transfer to generate the rhodium(II) centered complex resulting in the dissociation of H_3O^+, step 3 of Figure 65, followed by electrophilic attack of the metal bound hydride by H_3O^+, step 4 of Figure 65. It is also possible that steps 2 and 3 occur in the reverse order, photoinduced electron transfer occurs resulting in dissociation of H_2O, followed by protonation. It has been previously shown that the rhodium(III) complex $[(bpy)_2Rh^{III}(H)]^{2+}$ is unreactive toward H_3O^+ (rxn44) however upon the formation of the reduced rhodium(II) complex $[(bpy)_2Rh^{II}(H)]^+$ reaction with H_3O^+ or possibly H_2O occurs to generate H_2, the unsaturated rhodium(II) complex $[(bpy)_2Rh^{II}]^{2+}$, and H_2O or OH^-.[82] The proposed mechanism involves the same rhodium(II) reaction with H_3O^+ or possibly H_2O, shown as step 4 of Figure 65. A photoinduced electron transfer to reduce the complex back to the rhodium(I) square planar complex completes the catalytic cycle.

A number of variations of this mechanism are potentially feasible as well. The first protonation, step 1 of Figure 65, could be replaced by oxidative addition of H_2O

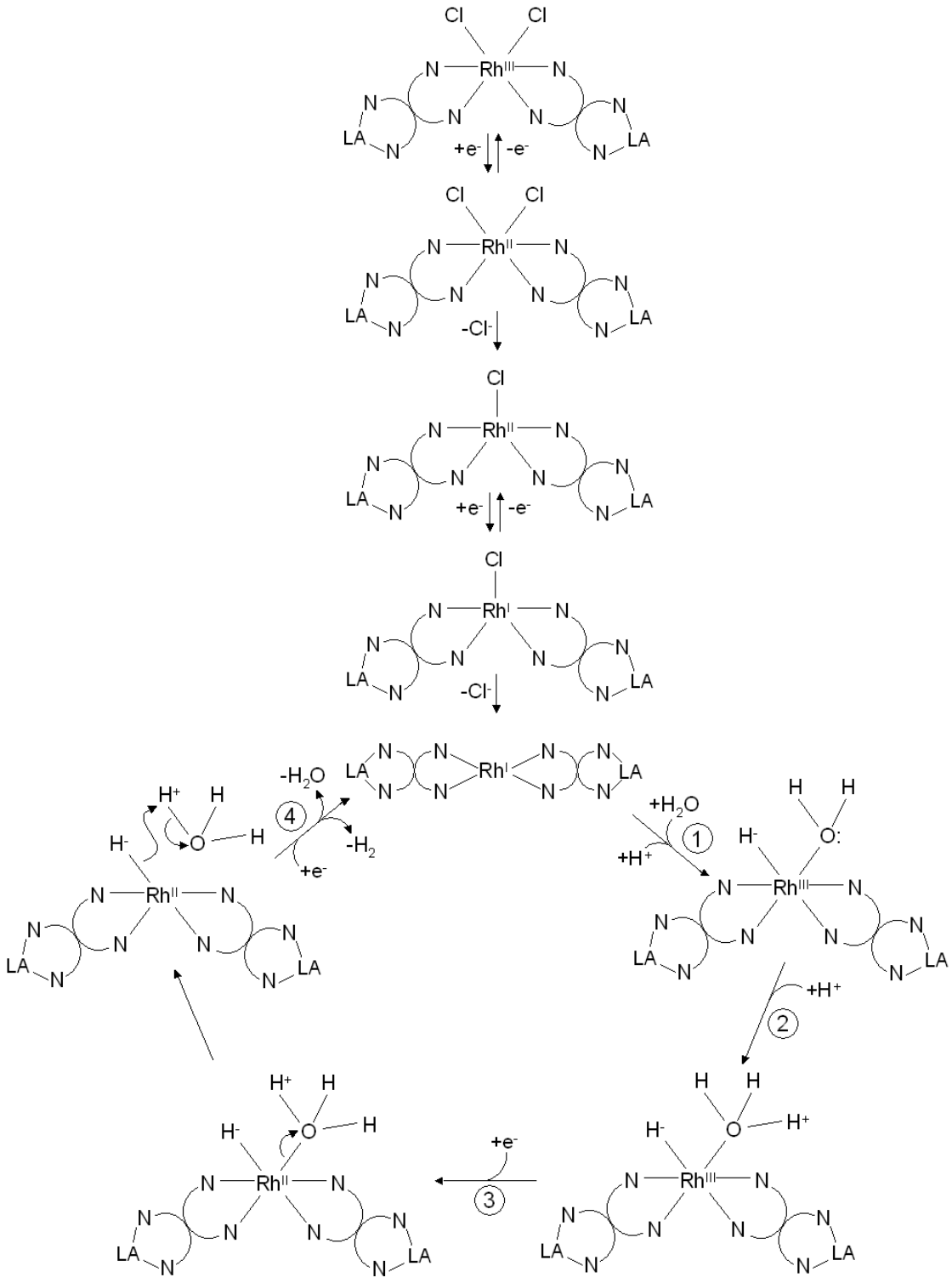

Figure 65. Proposed catalytic cycle for hydrogen generation from the trimetallic complex $[\{(bpy)_2Ru(dpp)\}_2RhCl_2]^{5+}$ [{(bpy)$_2$Ru (bpy = 2,2'-bipyridine; dpp = 2,3-bis(2-pyridyl)pyrazine). Ruthenium-polyazine light absorbers (LA) are abbreviated for clarity.

which would result in the complex $[\{(bpy)_2Ru(dpp)\}_2Rh^{III}(H)(OH)]^{5+}$, which could then undergo protonation or photoinitiated electron transfer to generate the rhodium(II) complex. Reduction of octahedral rhodium (III) complexes to rhodium(II) typically result in ligand loss, in this case OH^- or H_2O would likely be lost. Following a subsequent photoinitiated electron transfer to generate the rhodium(I) complex, hydride could be eliminated and react with H_2O in solution to form H_2, OH^-, and the initial form of the catalyst, $[\{(bpy)_2Ru(dpp)\}_2Rh^{I}]^{5+}$. A more accurate pK_b for the protonation of $[\{(bpy)_2Ru(dpp)\}_2Rh^{I}]^{5+}$ should be determinable be spectroelectrochemistry. It has been shown that the two electron reduction of $[\{(bpy)_2Ru(dpp)\}_2Rh^{III}Cl_2](PF_6)_5$ to form $[\{(bpy)_2Ru(dpp)\}_2Rh^{I}]^{5+}$ is accompanied by a blue shift for the $Ru(d\pi) \rightarrow dpp(\pi^*)$ CT transition, from 520 nm to 480 nm, which is observable in the visible region of the electronic absorption spectrum. Protonation of the resulting reduced complex by adding a small amount of acid likely result in spectroscopically observable shift upon the formation of $[\{(bpy)_2Ru(dpp)\}_2Rh^{III}(H)(H_2O)]^{6+}$. The pK_b of this protonation could be determined by titrating triflic acid into a buffered solution of $[\{(bpy)_2Ru(dpp)\}_2Rh^{III}Cl_2](PF_6)_5$. The formation of the rhodium(III) complex via protonation or oxidative addition can be probed further by ^1H NMR analysis of the hydride proton. The presence of hydride proton would confirm the presence of a rhodium-hydride intermediate. The hydride proton would be very sensitive to changes in the electronic environment and oxidation state of rhodium. Analysis by ^1H NMR may make it possible to corroborate or disprove steps of the hydrogen catalysis mechanism which involve rhodium-hydride bonds, i.e. $[\{(bpy)_2Ru(dpp)\}_2Rh^{III}(H)(OH)]^{5+}$, $[\{(bpy)_2Ru(dpp)\}_2Rh^{III}(H)(H_2O)]^{6+}$, and/or $[\{bpy)_2Ru(dpp)\}_2Rh^{III}(H)(H_3O)]^{7+}$.

An additional variation of the proposed mechanism involves photoinitiated electron transfer to generate the triply reduced complex $[\{(bpy)_2Ru(dpp^-)\}_2Rh^I]^{4+}$, where one of the dpp BLs receives an electron subsequent to the reduction of rhodium(III) to rhodium(I). This possibility remains unproven, however, the already reduced complex $[\{(bpy)_2Ru(dpp)\}_2Rh^I]^{5+}$ still has a strong absorption in the visible region of the spectrum at approximately 480 nm, which could possibly lead to additional photoinitiated processes. The reduction of dpp by one electron would have the result of adding electron density to the central rhodium(I) core, which would make rhodium a better Lewis base and thus shift the pK_B to a lower value, allowing for protonation of the complex $[\{(bpy)_2Ru(dpp)\}_2Rh^I]^{5+}$ at a more basic pH or at the same pH the percentage of complex in its protonated and doubly protonated forms would be higher.

VI. Conclusions

Since 1987 the incorporation of bis-bidentate bridging ligands like dpp into coordination complexes has opened up a new area of coordination chemistry. Balzani introduced the idea of using supramolecular complexes as photochemical molecular devices. In this context a supramolecular complex is made up of individual components connected together with bridging ligands to form a supramolecular architecture. Each component essentially retains its own properties and provides a specific function, which can be combined in certain architectures to exploit the component's function. Initially the electronic properties and electron/energy transfer were the focus of much study in order to gain a better understanding of the functioning of supramolecular assemblies. More recently this knowledge has led to the construction of supramolecular assemblies that are designed to use light to provide the necessary energy to "store electrons", or reducing equivalents. This type of photochemical molecular device is also referred to as a photoinitiated electron collector.

A system for photoinitiated electron collection must efficiently absorb light, undergo efficient successive and/or multiple electron transfer(s), and be stable in the multielectron-reduced form. Meeting all of these requirements makes the realization of a functional photoinitiated electron collector difficult. Prior to this work only four such systems have been reported.[39-50] Herein, the trimetallic complex $[\{(bpy)_2Ru(dpp)\}_2RhCl_2](PF_6)_5$, has been shown through electrochemical and photochemical experiments to undergo photoinitiated electron collection resulting in the doubly reduced rhodium(I) centered complex. The experiments discussed herein establish this system as one only a handful of photoinitiated electron collectors along

with the dpb bridged trimetallic complex $[\{(bpy)_2Ru(dpb)\}_2IrCl_2]^{5+}$,[39] the ruthenium bimetallic system $[(phen)_2Ru(BL)Ru(phen)_2]^{4+}$, where BL is tatpp (phenanthroline-pyrazine-benzene-pyrazine-phenanthroline) or tatpq (phenanthrolinepyrazine-quinone-pyrazine-phenanthroline),[41-43] and the platinum centered trimetallic complex $[\{(NC)_5M^{II}(CN)\}_2Pt^{IV}(NH_3)_4]^{4-}$ where M is Fe, Ru, or Os.[48-50] The trimetallic complex discussed herein is the first reported example that can collect electrons at a metal center and remains intact following photoinitiated electron transfer. This supramolecular architecture can be used to design a series of systems in order to fine tune the properties of the photochemical molecular device.

Supramolecular assemblies designed for photoinitiated electron collection are a relatively new class of molecular devices. Each reported supramolecular assembly that has been shown to undergo photoinitiated electron collection functions to some extent differently giving rise to certain advantages/disadvantages, which can depend on the desired application. The supramolecular assemblies $[\{(bpy)_2Ru(dpb)\}_2IrCl_2]^{5+}$,[39] $[(phen)_2Ru(tatpp)Ru(phen)_2]^{4+}$, and $[(phen)_2Ru(tatpq)Ru(phen)_2]^{4+}$ function by undergoing photoinitiated electron collection on the bridging ligands. The dpb bridged trimetallic has been shown to collect an electron on each of the dpb bridges, whereas the tatpp and tatpq bridged bimetallic complex has shown the ability to collect up to 2 and 4 electrons respectively on the bridge. The platinum centered trimetallic complex $[\{(NC)_5M^{II}(CN)\}_2Pt^{IV}(NH_3)_4]^{4-}$ where M is Fe, Ru, or Os,[48-50] was the first reported complex to undergo photoinitiated electron collection at a metal center, in this case platinum. Photoinduced electron transfer to generate the platinum(II) species, however,

results in dissociation of the light absorbing moieties precluding its use as a photocatalyst as it is presently constituted.

One potential application for a photoinitiated electron collector is in a light to chemical energy conversion scheme. The "stored electrons" could be used for the reduction of a substrate to generate a fuel. There are many difficulties associated with the design of a functional photochemical molecular device. In addition, the necessary photochemical reactivity towards a specific substrate is required, from both a kinetic and thermodynamic standpoint, adding to the difficulty in designing a photochemical molecular device that can be used in a light to energy conversion scheme. Prior to this work only one such system consisting of a light absorber and the site of catalysis within a single molecule has been reported that has shown functionality in a light to energy conversion scheme. In the system designed by Nocera, the catalytic production of hydrogen ensues from the fuel substrate, hydrohalic acid. The trimetallic complex $[\{(bpy)_2Ru(dpp)\}_2RhCl_2](PF_6)_5$, has also been shown to function as a photocatalyst for the production of hydrogen. The system reported herein is only the second hydrogen photocatalyst that functions with the light absorbing moiety, the site of collecting reducing equivalents, the coordinated of the substrate, and the catalytic formation of hydrogen all take place at a single molecule. More specifically, however, this complex appears to function by catalyzing the reduction of water to hydrogen, which would be the first reported system that uses water as a fuel feedstock, where the light absorber, electron collector, and site of catalysis are all located within a single molecule. This is of importance in that a system could potentially be designed around this catalyst for solar water splitting, the generation of hydrogen and oxygen from water. The system

requirements involving the photoinitiated aspect and the reductive half of solar water splitting have already been met in such a system.

The research presented here has expanded the knowledge of supramolecular photochemistry from a fundamental standpoint through the study of the complex $[\{(bpy)_2Ru(dpp)\}_2RhCl_2](PF_6)_5$. Electron transfer within this complex from the ^{3}MLCT state to the ^{3}MMCT state has been studied, as has bimolecular electron transfer from the sacrificial electron donor DMA to the ^{3}MLCT state and possibly the ^{3}MMCT state as well. This excited state electron transfer, or reductive quenching, has been studied in detail from a kinetic standpoint through a Stern-Volmer analysis. The rate of bimolecular quenching was determined to be 2×10^{10} M^{-1} s^{-1} for DMA, which has been shown to statically and dynamically quench the ^{3}MLCT and possibly the ^{3}MMCT state as well. A Stern-Volmer analysis of the formation of the reduced complex was also undertaken to probe the mechanism of product formation. It was determined that if quenching of the ^{3}MLCT state is the primary pathway for the formation of the reduced product, the rate of reductive quenching, k_q, is 1.9×10^9 M^{-1} s^{-1}. If, however, quenching of the ^{3}MMCT state is the primary pathway for the formation of the reduced product, where k_4 is the rate of unimolecular deactivation, i.e. radiative/nonradiative decay, and k_{q2} is the rate of quenching of the ^{3}MMCT state, k_4/k_{q2} is 0.062 and the value of k_{q2} would depend on the lifetime of the ^{3}MMCT state. In a related ruthenium/rhodium bimetallic system the rate of back electron transfer is reported to be 7.1×10^9.[31] If the rate of charge recombination in the trimetallic complex $[\{(bpy)_2Ru(dpp)\}_2RhCl_2](PF_6)_5$ is similar this would result in a k_{q2} of 1.1×10^{11}. Considering the much smaller driving force for quenching the ^{3}MMCT as compared to the ^{3}MLCT state is unlikely the k_{q2} rate constant would be so large. This

kinetic analysis suggests quenching of the ^{3}MLCT state may be the primary path for the formation of product however quenching of the ^{3}MMCT state may contribute as well.

The trimetallic complex $[\{(bpy)_2Ru(dpp)\}_2RhCl_2](PF_6)_5$ has also been shown to function as a photocatalyst for the reduction of water to hydrogen, the first reported system where the light absorber, electron collector, and site of catalysis are all located within a single molecule. A series of hydrogen photocatalysis experiments were performed to probe the impact of various factors like metal complex concentration, electron donor concentration, water concentration and catalysis as a function of time. Determining the impact of these factors can lead to a better understanding of the functioning of this system. From these catalysis studies it was determined that over the course of four hours of photolysis the production of hydrogen was linear with respect to time, indicating the complex remains catalytically active and is resistant to poisoning within the timeframe of the experiment. From the Stern-Volmer analysis it was shown that DMA both statically and dynamically quenches the excited complex. In addition, from the hydrogen catalysis experiments it was shown that electron donor concentration has a significant impact on the rate of hydrogen production. It was also determined that water concentration had little impact on the rate of hydrogen production in the range probed. This could be a result of several factors. Water could have an affinity towards the complex making any change in water concentration less impactful, if this were the case a change in hydrogen production should be expected at some lower concentration of water. Alternatively, hydrogen production may not be impacted by changes in water concentration because it is not the rate limiting step. Finally, it was found that metal

complex concentration has little impact on the rate of hydrogen production, indicating that it is unlikely hydrogen production takes place through a bimolecular pathway.

VII. Future Work

A. Hydrogen Photocatalysis in an Aqueous Environment

Applied research toward a commercially viable hydrogen photocatalyst is not the primary goal of this work, but is one aspect of future research. Conversion from an organic solvent system to a more environmentally friendly aqueous system is one such applied research future goals. There are a number of factors to consider when designing an aqueous system that will still function to produce hydrogen photocatalytically. One of the primary concerns is that the catalyst and the chosen electron donor must both be soluble in water. The catalyst, $[\{(bpy)_2Ru(dpp)\}_2RhCl_2](PF_6)_5$, has limited solubility in water, however, the chloride version of the complex, $[\{(bpy)_2Ru(dpp)\}_2RhCl_2]Cl_5$, has excellent solubility in water. A simple metathesis is all that is required to convert the trimetallic complex to the water soluble form.

In addition to having water solubility, the electron donor must also meet several additional requirements: the electron donor must also have a pK_A low enough to result in protonation of the trimetallic complex; a strong association between the donor and catalyst is preferable to increase the limiting quantum yield; an electron donor that is sacrificial in nature, i.e. decomposes to form a harder to reduce product following oxidation, to limit back electron transfer is necessary; and the electron donor must have an oxidation potential low enough to donate an electron to the ^{3}MLCT excited state of the trimetallic complex and possibly the ^{3}MMCT excited state as well. Two possible electron donors currently under investigation are ascorbic acid and triethylamine. A systematic screening of electron donors can probe the relative importance of donor pK_A,

donor-complex association, and driving force. The impact of driving force by utilizing alternative electron donors is discussed below in more detail.

B. Modulation of Driving Force using Alternative Electron Donors

A thorough study modulating the driving force for quenching can shed light on the mechanism for the formation of the reduced rhodium(II) and rhodium(I) complexes via the ^{3}MLCT and/or ^{3}MMCT states. This can be achieved through multiple avenues including modulation of the supramolecular architecture or employing alternative electron donors. The chosen electron donor has a direct impact on the driving force of reductive quenching for both the ^{3}MLCT and ^{3}MMCT states. Selecting a donor with a higher oxidation potential will decrease the driving force for quenching the ^{3}MLCT and ^{3}MMCT states, whereas selecting a donor with a lower oxidation potential will increase the driving force for quenching both states. Table 5 consists of a list of potentially useful

Table 5. Electron donors listing their corresponding $E_{1/2}$s for oxidation vs. SCE, the rate of bimolecular quenching for $[Ru(bpy)_3]^{2+}$ (bpy = 2,2'-bipyridine) and the driving force for quenching the ^{3}MLCT and ^{3}MMCT states of the trimetallic complex $[\{(bpy)_2Ru(dpp)\}_2RhCl_2](PF_6)_5$ (dpp = 2,3-bis(2-pyridyl)pyrazine).

			driving force for quenching (V)		
Quencher	$E_{1/2}$ (Q/Q^+)	k_q ($M^{-1}s^{-1}$)	^{3}MLCT	^{3}MMCT	*ref*
N,N,N',N'-tetramethylphenylenediame	0.12	1.3×10^{10}	1.17	0.78	*84*
phenylenediamine	0.18	1.1×10^{10}	1.11	0.72	*84*
N,N,N',N'-tetramethylbenzidine	0.43	1.0×10^{10}	0.86	0.47	*84*
phenothiazine	0.53	5.6×10^{9}	0.76	0.37	*71, 84*
1-napthylamine	0.63	1.6×10^{8}	0.66	0.27	*84*
p-anisidine	0.71	7.5×10^{8}	0.58	0.19	*84*
N,N-diethylaniline	0.76	2.5×10^{8}	0.53	0.14	*84*
o-anisidine	0.76	5.4×10^{7}	0.53	0.14	*84*
N-methylaniline	0.77	2.4×10^{7}	0.52	0.13	*84*
N,N-dimethylaniline	0.81	9.9×10^{7}	0.48	0.09	*71, 84*
diphenylamine	0.83	1.8×10^{7}	0.46	0.07	*71, 84*
aniline	0.98		0.31		*71*
triphenylamine	1.06		0.23		*71*

electron donors, their oxidation potentials, and the corresponding driving force for quenching for both the ^{3}MLCT and ^{3}MMCT states for the complex $[\{(bpy)_2Ru(dpp)\}_2RhCl_2](PF_6)_5$.

Driving force for reductive quenching is not the only factor to consider when selecting an electron donor. Donor-solvent, complex-solvent, and donor-complex, interactions can all impact device functioning. Donor-solvent and complex-solvent interactions are simply the solubility of the electron donor and complex in the chosen solvent which is currently acetonitrile. Some solubility is required to allow for homogeneous interactions between the donor and the catalyst. Donor-complex interactions consist of the attraction of the donor to the catalyst including any preassociation prior to photolysis, which can impact the limiting quantum yield and overall device functioning. Any difference in the rate of formation of the photoreduced product must be elucidated from these interactions resulting in a potentially complex study.

C. Modulation of Driving Force by Modifications to the Supramolecular Framework

The supramolecular architecture employed for the photocatalyst discussed throughout this work is composed of two ruthenium-polyazine light absorbers covalently bound via bridging ligands to a central rhodium core acting as a multielectron collector. Each component plays a role and has an impact on the orbital energetics, which is a key in the functioning of the supramolecular device. As demonstrated in section IV. C. the substitution of rhodium for iridium and dpp for dpb results in a device that does not result

in electron collection on the central metal but instead collects an electron on each dpb bridging ligand, the location of the lowest lying molecular orbital. Terminal ligands, bridging ligands, peripheral metal and central metal can all be interchanged with other ligands/metals which can result in small or large changes to the overall electronic environment.

A study involving the modulation of driving force for reductive quenching by an electron donor by modifying the supramolecular framework must be carefully designed to allow meaningful changes to be measurable through quenching studies and assignable to a specific factor. A single change to the supramolecular framework often impacts many electronic transitions within the molecule. The experimental design attempts to minimize the impact of a structural modification to a single measurable transition, although in reality this is difficult to achieve. One such experiment involves the bromide version of the trimetallic complex of the form $[\{(bpy)_2Ru(dpp)\}_2RhBr_2](PF_6)_5$. Bromide is lower in the spectrochemical series than chloride so substituting the rhodium bound chlorides for the weaker ligand field bromides should lower the rhodium based LUMO, Figure 66. This should impact the molecular device in two ways. The driving force for

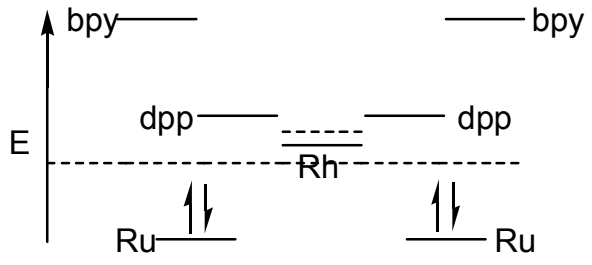

Figure 66. Molecular orbital diagram for the complex $[\{(bpy)_2Ru(dpp)\}_2RhBr_2]^{5+}$ (bpy = 2,2'-bipyridine; dpp = 2,3-bis(2-pyridyl)pyrazine) indicating the lowering of the rhodium based lowest lying molecular orbital by replacing the chloros for bromos.

transfer, however if the increased energy gap between states is large enough the energy electron transfer to generate the ^{3}MMCT state should be increased by increasing the dpp orbital, rhodium orbital gap. This could result in a higher, lower or unchanged rate of gap law would dictate a decrease in the rate of deactivation from the ^{3}MLCT state electron transfer. The increased driving force should increase the rate of electron through electron transfer. The overall change could be measured through emission spectroscopy by using the chloride complex as a model for electron transfer. Secondly, the substitution of chlorides for bromides can impact the driving force for quenching the ^{3}MMCT state while the driving force for quenching the ^{3}MLCT state should remain largely unchanged. A Stern-Volmer analysis for product formation akin to the one performed on the chloride trimetallic complex can help in determining the impact of the bromide substitution and also help elucidate the overall mechanism for the formation of the photoreduced product. It would be expected to lower the driving for reductive quenching of the ^{3}MMCT state. If the rate of product formation is unchanged, quenching of the ^{3}MLCT state is most likely the primary pathway for the formation of the rhodium(II) product. If there is a decrease in rate of product formation it is likely that quenching of the ^{3}MMCT state plays a role in the formation of product. It is possible, however, that a decrease in product formation could be a result of an increased k_{et}, where in the ^{3}MLCT quenching mechanism it is treated as a deactivation pathway.

Another modification to the supramolecular architecture that may provide information on the mechanism for photoinitiated electron collection is the substitution of the terminal ligands. Substituting the two bipyridine ligands for a single terpyridine and a halide like chloride would raise the ruthenium based HOMO, Figure 67. The complex,

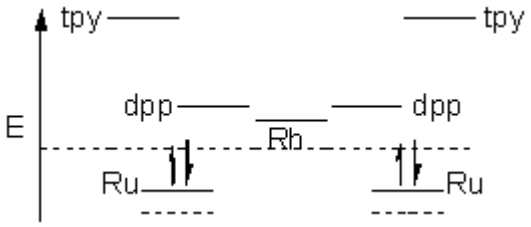

Figure 67. Molecular orbital diagram for the complex $[\{(tpy)ClRu(dpp)\}_2RhCl_2]^{5+}$ (tpy = 2,2‘,2“-terpyridine; dpp = 2,3-bis(2-pyridyl)pyrazine) indicating the raising of the ruthenium based highest occupied molecular orbital by replacing the two bipyridines on each light absorber for a terpyridine and a chloride.

$[\{(tpy)ClRu(dpp)\}_2RhCl_2](PF_6)_5$, Figure 68, should possess lower energy ^{3}MLCT and ^{3}MMCT states while the dpp orbital – rhodium orbital gap should remain unchanged thus the rate of electron transfer should remain unchanged. This should result in a lower driving force for quenching both states. In conjunction with the previous study any impact on the rate of product formation could help in the determination of the mechanism for photoinitiated electron collection.

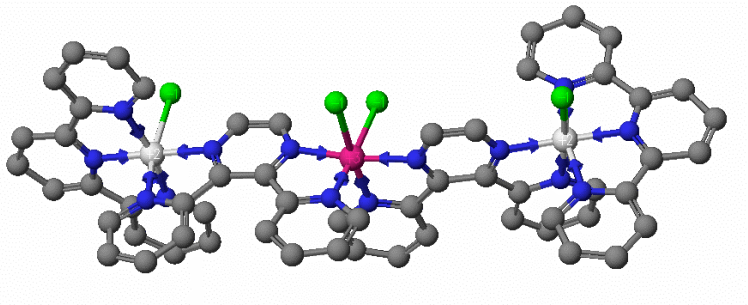

Figure 68. CAChe generated structure for the trimetallic complex $[\{(tpy)ClRu(dpp)\}_2RhCl_2]^{5+}$ (tpy = 2,2‘,2“-terpyridine; dpp = 2,3-bis(2-pyridyl)pyrazine) a potential photoinitiated electron collector.

D. Real Time Detection of Hydrogen

Future work will incorporate a hydrogen sensor for monitoring hydrogen production in real time. We have acquired a Model 700 in-line process monitor custom designed by H2scan, Figure 69, calibrated to measure hydrogen concentrations as low as 15 ppm. Photolysis cells have been designed and constructed in house which can be attached directly onto the sensor unit via a compression fitting. The photolysis cells are designed to minimize the overall headspace volume in order to improve the lower limit of detection. The hydrogen sensor is shown in Figure 69. Real time data collection allows for a detailed kinetic analysis of hydrogen production. Real time data also enables a more detailed analysis of early photolysis times, which can provide insight into the mechanism of catalyst functioning.

Much of the future work including but not limited to studying the modulation of the driving force for reductive quenching of the MLCT and MMCT states using alternative electron donors or through modifications to the supramolecular framework, and the utilization of real time detection of hydrogen generation using the supramolecular photocatalyst $[\{(bpy)_2Ru(dpp)\}_2RhCl_2]^{5+}$ are planned for the near future or are already in their initial stages. This work is intended to probe the mechanism of photoinitiated electron collection, and potentially provide data that can assist in the elucidation of the mechanism of hydrogen photocatalysis, which is essential in understanding the functioning of these systems. A thorough understanding of catalyst functioning can lead to system modulations and ultimately enhance catalytic efficiency.

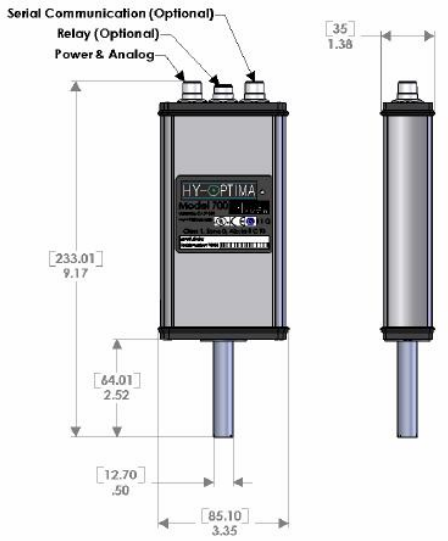

Figure 69. Model 700 in-line process monitor custom designed by H2scan used for real time hydrogen detection.

VIII. References

1.) Balzani, V; Juris, A; Venturi, M; Campagna, S; Serroni, S. *Chem. Rev*. **1996**, *96*, 759.

2.) Brewer, K. *Comments Inorg. Chem*. **1999**, *21*, 201.

3.) Cola, L; Belser, P. *Coordination Chemistry Reviews*. **1998**, *177*, 301.

4.) Flamigni, L; Barigelletti, F; Armaroli, N; Collin, J; Dixon, I; Sauvage, J; Williams, J; *Coordination Chemistry Reviews*. **1999**, *190-192*, 371.

5.) Burstall, F. *J. Chem. Soc*. **1936**, 173.

6.) Durham, B.; Caspar, J.; Nagle, J.; Meyer, T. *J. Am. Chem. Soc.* **1982**, *104*, 4803-4810.

7.) Kirch, M.; Lehn, J.; Sauvage, J. *Helvetica Chimica Acta.* **1979**, *62*, 1345-84.

8.) Lehn, J.; Sauvage, J.; Ziessel, R. *Nouveau Journal de Chimie.* **1981**, 5, 291-5.

9.) Chan, S; Creutz, C; Matsubara, T; Sutin, N. *J. Am. Chem. Soc.* **1981**, *103*, 369.

10.) Brown, G; Chan, S; Creutz, C; Schwarz, H; Sutin, N. *J. Am. Chem. Soc.* **1979**, *101*, 7638.

11.) Schwarz, H; Creutz, C. *Inorg. Chem.* **1983**, *22*, 707.

12.) Chou, M; Creutz, C; Mahajan, D; Sutin, N; Zipp, A. *Inorg. Chem.* **1982**, *21*, 3989.

13.) Creutz, C; Keller, A; Sutin, N; Zipp, A. *J. Am. Chem. Soc.* **1982**, *104*, 3618.

14.) Fuchs, Y.; Lofters, S.; Dieter, T.; Shi, W.; Morgan, S.; Strekas, T.; Gafney, H.; Baker, A. *J. Am. Chem. Soc.* **1987**, *109*, 2691.

15.) Rasmussen, S; Richter, M; Yi, E; Place, H; Brewer, K. *Inorg. Chem.* **1990**, *29*, 3926.

16.) Scandola, F; Bignozzi, C; Chiorboli, C; Indelli, M; Rampi, M. *Photoprocesses in Transition Metal Complexes, Biosystems and other Molecules. Experiment and Theory, Kluwer, The Netherlands*. **1992**, 253.

17.) Marcus, R.; Sutin, N. *Biochem. Biophys. Acta 811*. **1985**, 265

18.) Kavarnos, G. *Fundamentals of Photoinduced Electron Transfer, NewYork.* **1993**.

19.) Barbara, P; Meyer, T; Ratner, M. *J. Phys Chem*. **1996**, *100*, 13148.

20.) Rehm, D; Weller, A; *Isr. J. Chem*. **1970**, *8*, 59.

21.) Marcus, R. *Annu. Rev. Phys. Chem*. **1964**, *15*, 155.

22.) Atkins, P. Physical Chemistry, 6th ed. W. H. Freeman and Company, NY (1998).

23.) Kalyanasundaram, K; Gratzel, M; Nazeeruddin, K. *J. Phys. Chem*. **1992**, *96*, 5865.

24.) Meyer, T. J. *Pure Appl. Chem*. **1986**, *58*, 1193.

25.) Lei, Y; Buranda, T; Endicott, J. *J. Am. Chem. Soc.* **1990**, *112*, 8820.

26.) Calef, D; Wolynes, P. *J. Phys. Chem*. **1983**, *87*, 3387.

27.) Nozaki, K; Ohno, T; Haga, M. *J. Phys. Chem*. **1992**, *96*, 10880.

28.) Indelli, M; Scandola, F; Collin, J; Sauvage, J. *Inorg. Chem.* **1996**, *35*, 303.

29.) Indelli, M; Scandola, F; Collin, J; Sauvage, J. *Inorg. Chem.* **1997**, *36*, 4247.

30.) Lee, J; Vrana, L; Bullock, E; Brewer, K. *Inorg. Chem.* **1998**, *37*, 3575.

31.) Scandola, F; Argazzi, R; Bignozzi, C; Indelli, M. *J. Photochem. Photobiol*. **1994**, *82*, 191.

32.) Campagna, S.; Serroni, S.; Puntoriero, F.; Di Pietro, C.; Ricevuto, V. *In Electron Transfer in Chemistry*; Balzani, V., Ed.; Wiley-VCH: New York, **2001**; Vol. 5, p 168 and references cited therein.

33.) Balzani, V.; Moggi, L.; Manfrin, M. F.; Bolletta, F.; Laurence, G. A. *Coord. Chem. Rev.* **1975**, *15*, 321.

34.) Meyer, T. J. *Pure Appl. Chem.* **1986**, *58*, 1576.

35.) Kalyanasundaram, K. *Coord. Chem. Rev.* **1982**, *46*, 159.

36.) Balzani, V.; Moggi, L.; Scandola, F. *In Supramolecular Photochemistry*; Balzani, V., Ed.; NATO Advanced Study Institute Series 214; Reidel: Dordrecht, The Netherlands, **1987**; p 1 and references cited therein.

37.) Balzani, V.; Juris, A.; Venturi, M.; Campagna, S.; Serroni, S. *Chem. Rev.* **1996**, 96, 759.

38.) Serroni, S.; Campagna, S.; Puntoriero, F.; Loiseau, F.; Ricevuto, V.; Passsalacqua, R.; Galletta, M. *C. R. Chim.* **2003**, *6*, 883.

39.) Molnar, S. M.; Nallas, G.; Bridgewater, J. S.; Brewer, K. J. *J. Am. Chem. Soc.* **1994**, *116*, 5206.

40.) Rasmussen, S.; Richter, M.; Yi, E.; Place, H.; Brewer, K. *Inorg. Chem.* **1990**, *29*, 3926.

41.) Konduri, R.; Ye, H.; MacDonnell, F. M.; Serroni, S.; Campagna, S.; Rajeshwar, K. *Angew. Chem., Int. Ed.* **2002**, *41*, 3185.

42.) Chiorboli, C.; Fracasso, S.; Scandola, F.; Campagna, S.; Serroni, S.; Konduri, R.; MacDonnell, F. M. *Chem. Commun.* **2003**, 1658.

43.) Chiorboli, C.; Fracasso, S.; Ravaglia, M.; Scandola, F.; Campagna, S.; Wouters, K.; Konduri, R.; MacDonnell, F. *Inorg. Chem.* **2005**, *44*, 8368.

44.) Heyduk, A. F.; Nocera, D. G. *Science* **2001**, *293*, 1639.

45.) Nocera, D.; Heyduk, A. *PCT Int. Appl.* **2003**, 157.

46.) Dempsey, J.; Esswein, A.; Manke, D.; Rosenthal, J.; Soper, J; Nocera, D. *Inorg. Chem*. **2005**, *44*, 6879.

47.) Esswein, A.; Veige, A.; Nocera, D. *J. Am. Chem. Soc*. **2005**, *127*, 16641.

48.) Chang, C. C.; Pfennig, B.; Bocarsly, A. B. *Coord. Chem. Rev*. **2000**, *208*, 33.

49.) Watson, D. F.; Tan, H. S.; Schreiber, E.; Mordas, C. J.; Bocarsly, A. B. *J. Phys. Chem. A*. **2004**, *108*, 3261.

50.) Mordas, C.; Pfennig, B.; Schreiber, E.; Bocarsly, A. B. *Springer Ser. Chem. Phys*. **2003**, *71*, 453.

51.) Lide, D. Handbook of Chemicstry and Physics 87th ed. CRC Press, LLC (2006).

52.) Dempsey, J.; Esswein, A.; Manke, D.; Rosenthal, J.; Soper, J.; Nocera, D. *Inorg. Chem*. **2005**, *44*, 6879-6892.

53.) Rosenthal, J.; Bachman, J.; Dempsey, J.; Esswein, A.; Gray, T.; Hodgkiss, J.; Manke, D.; Luckett, T.; Pistorio, B.; Veige, A.; Nocera, D. *Coord. Chem. Rev.* **2005**, *249*, 1316-1326.

54.) Bard, A.; Fox, M. *Acc. Chem. Res.*, **1995**, *28*, 141-145.

55.) Bolton, J. R., *Science*, **1978**, *202*, 705-711.

56.) Balzani, V. M.; Moggi, M.; Manfrin, M. F.; Bolletta, F.; Gleria, M. *Science*, **1975**, *189*, 852-856.

57.) Oishi, S. *J. Mol. Cat*. **1987**, *39*, 225.

58.) Bauer, R., Werner, H. *Int. J. Hydrogen Energy*, **1994**, 19, 497.

59.) Sullivan, B.; Salmon, D.; Meyer, T. *Inorg. Chem.* **1978**, *17*, 3335.

60.) Gennett, T.; Milner, D. F.; Weaver, M. *J. Phys. Chem*. **1985**, *89*, 2787.

61.) Caspar, J.; Kober, E.; Sullivan, B.; Meyer, T. *J. Am. Chem. Soc.* **1982**, *104*, 630.

62.) Kober, E.; Sullivan, B.; Dressick, W.; Caspar, J.; Meyer, T. *J. Am. Chem. Soc.* **1980**, *102*, 1383.

63.) Brown, J.; Elvington, M.; Mongelli, M.; Zigler, D.; Brewer, K. *Proceedings of the SPIE, Optics and Photonics, Solar Hydrogen and Nanotechnology* **2006**, *Proc. of SPIE Vol. 6340*, 634007W1-13.

64.) Gordon, A.; Ford, R. The Chemists Companion: A Handbook of Practical Data, Techniques and References. John Wiley & Sons, NY (1972).

65.) Bard, A.; Faulkner, L. Electrochemical Methods. John Wiley & Sons, NY (2001).

66.) Elvington, M.; Brewer, K. *Inorg. Chem*. **2006,** *45*, 5242-5244.

67.) Kew, G.; DeArmond, K.; Hanck, K. *J. Phys. Chem*. **1974**, *78*, 727.

68.) Kalyanasundaram, K.; Nazeeruddin, K. *Inorg. Chem*. **1990**, *29*, 1888-1897.

69.) Swavey, S.; Brewer, K. *Inorg. Chem.* **2002**, *41*, 4044-4050.

70.) Anderson, C.; Salmon, D.; Meyer, T.; Young, R. *J. Am. Chem. Soc.* **1977**, *99*, 1980.

71.) Haga, M.; Dodsworth, E.; Eryavec, G.; Seymour, P.; Lever, B. *Inorg. Chem.* **1985**, *24*, 1901.

72.) Indelli, M.; Bignozzi, C.; Harriman, A.; Schoonover, J.; Scandola, F. *J. Am. Chem. Soc.* **1994**, *116*, 3775.

73.) Hand, R.; Nelson, R. *J. Electrochem. Soc.* **1970**, *117*, 1353-1357.

74.) Yang, H.; Wipf, D.; Bard, A. *J. Electroanal. Chem.* **1992**, *331*, 913-924.

75.) Mizoguchi, T.; Adams, R. *J. Am. Chem. Soc.* **1962**, *84*, 2058-2061.

76.) Galus, Z.; Adams, R. *J. Am. Chem. Soc.* **1962**, *84*, 2061-2065.

77.) Galus, Z.; White, R.; Rowland, F.; Adams, R. *J. Am. Chem. Soc.* **1962**, *84*, 2065-2068.

78.) Pankratov, A.; Uchaeva, I.; Stepanov, A. *Can. J. Chem.* **1993**, *71*, 674-677.

79.) Brunner, E. *J. Chem. Eng. Data*. **1985**, *30*, 269.

80.) Whitten, K.; Davis, R.; Peck, M. General Chemistry. Saunders College Publishing, Orlando, FL (1996)

81.) Chou, M.; Creutz, C.; Mahajan, D.; Sutin, N.; Zipp, A. *Inorg. Chem*. **1982,** *21*, 3989-3997.

82.) Bakac, A. *Dalton Trans*. **2006**, 1589-1596.

83.) Cotton, F.; Wilkinson, G.; Murillo, C.; Bochmann, M. Advanced Inorganic Chemistry 6th ed. John Wiley & Sons, NY (1999).

84.) Mulazzani, Q.; Venturi, M.; Hoffman, M. J. Phys. Chem. **1982**, *86*, 242-247.

85.) Kitamura, N.; Kim, H.; Okano, S.; Tazuke, S. *J. Phys. Chem*. **1989**, *93*, 5750-5756.